NORTHWESTERN UNIVERSITY

Studies of Single Nanoparticle Systems by Localized Surface Plasmon Resonance Spectroscopy, Atomic Force Microscopy, Transmission Electron Microscopy, and Combinations Thereof

A DISSERTATION

SUBMITTED TO THE GRADUATE SCHOOL

IN PARTIAL FULFILLMENT OF THE REQUIREMENTS

for the degree

DOCTOR OF PHILOSOPHY

Field of Chemistry

By

Leif Jorstad Sherry

EVANSTON, ILLINOIS

June 2007

Abstract

Studies of Single Nanoparticle Systems by Localized Surface Plasmon Resonance Spectroscopy, Atomic Force Microscopy, Transmission Electron Microscopy, and Combinations Thereof

Leif J. Sherry

The work presented here describes investigations into the optical properties of single silver nanoparticles. The contents of this thesis are divided into two parts: (1) single nanoparticle localized surface plasmon resonance (LSPR) spectroscopy and sensing and (2) approaches to combining LSPR spectroscopy with atomic force and transmission electron microscopies. Part I addresses the LSPR properties of two specific nanoparticle geometries: triangular nanoprisms and nanocubes. It was shown that the LSPR spectra for ensembles of these structures are inhomogenously broadened, and that the LSPR spectra of single nanoparticles are highly sensitive to details of their geometries. These geometric details play an important role in determining the utility of a nanoparticle as an environmental sensor. It was demonstrated that nanoprisms have a 1 nm per alkyl unit greater sensitivity to the binding of molecular adsorbates than truncated tetrahedral arrays despite being five times thinner, suggesting they will be excellent candidates for sensing large biomolecules. It was further shown, for the case of the nanocubes, that the energy of LSPR modes are not simply sensitive to their environments, but that the environment can actually affect the number of modes observed in a nanoparticle's LSPR spectrum. For the nanocube it was shown that this leads to two peaks: a narrow high energy peak and a broader low energy peak. A figure of merit has been defined for single nanoparticle sensors and nanocubes' high energy peaks were shown to have the highest value FOM measured to date. Part II addresses the ambiguity that persists in standard single nanoparticle LSPR studies

due to the fact that no structural information is available to enlighten interpretations of nanoparticle spectra. This was done by correlating the LSPR spectra with atomic force microscopy (AFM) and transmission electron microscopy (TEM) measurements.

Prof. Richard P. Van Duyne
Prof. George C. Schatz
Research Advisors

Acknowledgements

I would like to thank my advisors Richard Van Duyne and George Schatz for the opportunity to work on such extremely challenging problems with a dynamic group of scientists. Their availability, support, and insights have been invaluable. I was extremely lucky to not only have great advisors, but great research groups in which to work. I would like to give a special thanks to the entire Van Duyne research group for a wonderful day-to-day work environment. I spent almost 100% of my time there since I promptly lost my desk in the theory group after my first year. I would like to echo the assertion made by my colleague Dr. Alyson Whitney in her thesis that the first row is the best row. Jon, Kathryn, Alyson…..I couldn't have done it without you. I would also like to thank the rest of the lab, but I will not individually since Rick has managed to quadruple his number of students since my arrival in 2002.

Of course, science today is not an individual effort and I would be remiss not to acknowledge those who directly contributed to the work presented here. I would first like to thank Dr. Adam McFarland for his guidance and training during my graduate school infancy. His breadth and depth of knowledge was a tremendous resource. I would like to thank Prof. Shengli Zou for his assistance with DDA calculations, and Prof. Shih-Hui Chang for performing the FDTD calculations in Chapter 3. Benjamin Wiley and Prof. Younan Xia from The University of Washington fabricated the nanocubes discussed in Chapter 3, Alyson Whitney and Kathryn Kosuda provided ALD coated samples, and Yingmin Wang performed TEM analysis for the work presented in Chapter 5. I would like to give a special thanks to Prof. Kallie Willets. She was instrumental in the construction, trouble-shooting, and development of the TIR-AFM instrument. I enjoyed all our time working together, and our many discussions.

Last, but no least, I would like to thank my family. They have constantly kept me grounded throughout my academic career, and cognizant of how science is viewed by the general public. To my parents, thank you for believing in me. To my grandparents, thank you for your interest and your many letters. To my sisters, thank you for not understanding half of what I say. And to my wife, thank you for your support (both emotionally and financially). It has to all be downhill from here, right!

Table of Contents

List of Illustrations

List of Tables

Chapter 1

Introduction to the Localized Surface Plasmon Resonance

1.1 Historical Perspective

In 1974 Professor Norio Taniguchi first defined nanotechnology as such: "'Nano-technology mainly consists of the processing of, separation, consolidation, and deformation of materials by one atom or one molecule."[1] However, when this definition, or one much like it, is recited to the laymen they fail to recognize how this new way of understanding and controlling matter will affect their lives. I empathize with these individuals since I, too, would fail to see a connection to something so grand and new as a "technological revolution" from such a statement without the specialized training I've received these last five years. In truth, this statement would simply seem like the prophecy of the ultimate engineering achievement. Not a trivial matter, mind you, but hardly something that should herald the beginning of a new age in technology.

Of course there is something new, or else the scientific community would not be so excited. What is that something else? It is size and shape dependent properties. At no other scale in nature do such phenomena exist. If, for instance, one were to cut a one ounce piece of gold in half, or shape it into a coin from an amorphous lump, all of its properties will remain as they were before the gold piece was altered. It will melt at the same temperature, look the same color, and have the same coefficient of thermal expansion in either (or any) geometric configuration. This is not the case at the nanoscale. And though the optical properties of metal nanoparticles have been of interest since the time of Faraday in the 1800's,[2] it was not until the later half of the twentieth century that scientists showed that the magnetic,[3-8] catalytic,[9-14] thermal,[15-19] electrochemical,[20-23] electronic,[24-29] and optical[30-33] properties of nanoscale materials display size and shape dependence.

In the Van Duyne and Schatz groups we focus on understanding the *optical* properties of nanoscale materials: specifically those constituting the noble metals (gold, silver, and copper). Why the noble metals? These metals have a special optical property associated with them known as surface plasmons. This phenomenon can take two forms: propagating surface plasmons (also known as surface plasmon polaritons), which are supported in thin noble metal films,[34] and localized surface plasmons, which are supported in noble metal nanoparticles.[35] Van Duyne and Schatz became interested in surface plasmons in 1977 when Van Duyne and coworkers proposed that the huge enhancement (10^4-10^7) of a very weak optical process known as Raman scattering was due to enhanced electromagnetic (EM) fields on a silver surface containing nanoscale features.[36] These enhanced electromagnetic fields were a result of localized surface plasmon resonances (LSPR) being excited in the nanoscale features by incident light.[37] The Raman scattering process came to be known as surface-enhanced Raman scattering (SERS). Raman scattering is a process by which molecules scatter light inelastically (the incoming and exiting photons have different energies). The probability of the process taking place for any one incoming photon is extremely low (1 out of 1,000 photons are Raman scattered) making the Raman signal extremely weak. SERS, however, made Raman spectroscopy competitive with other optical processes such as fluorescence and absorption spectroscopy. This, coupled with the fact that Raman spectroscopy is the most information rich optical spectroscopy, fueled not only a renewed interest in Raman spectroscopy, but a new research field of its own. Since the enhanced fields at a roughened metal surface due to the localized surface plasmons were hypothesized as one mechanism by which SERS was possible, a huge research effort was made to understand and control plasmonically active materials. Before

I present an overview of this field, however, I would like to outline the basic physics of localized surface plasmons. I would like to emphasize that this introduction is meant to give the reader a qualitative picture of the physical phenomena being studied, and that this treatment is based on a classical electrodynamics argument.

1.2 Introduction to Surface Plasmons

Surface plasmons are coherent oscillations of a metal's conduction band electrons. The mechanism behind electromagnetic excitation of localized surface plasmons is as follows. When electromagnetic radiation interacts with a charged species, that species will feel a force (the electromotive force). If the species is positively charged, it will move in the direction of the force. If the species is negatively charged, it will move in the opposite direction. Hence, when a noble metal is irradiated by an oscillating EM field its electrons will oscillate in response to this field as depicted in Figure 1.1. The magnitude of the material's electronic response depends on the electronic structure of the material. Noble metals' outer shell electrons are well shielded from their positive nuclei by filled lower lying electronic orbitals. This allows the outer shell electrons to delocalize over large areas in coordinated noble metal structures. This is the source of these materials' conductive properties, and hence these electrons are said to occupy the "conduction band". This is why noble metals support plasmons. One will notice that figure 1.1 depicts the oscillation of the electrons as a displacement of the outer electrons from the positive nanoparticle core. This can be done due to the delocalized nature of the metal's conduction band electrons. Since they are delocalized, they can be modeled as a free electron gas. When this

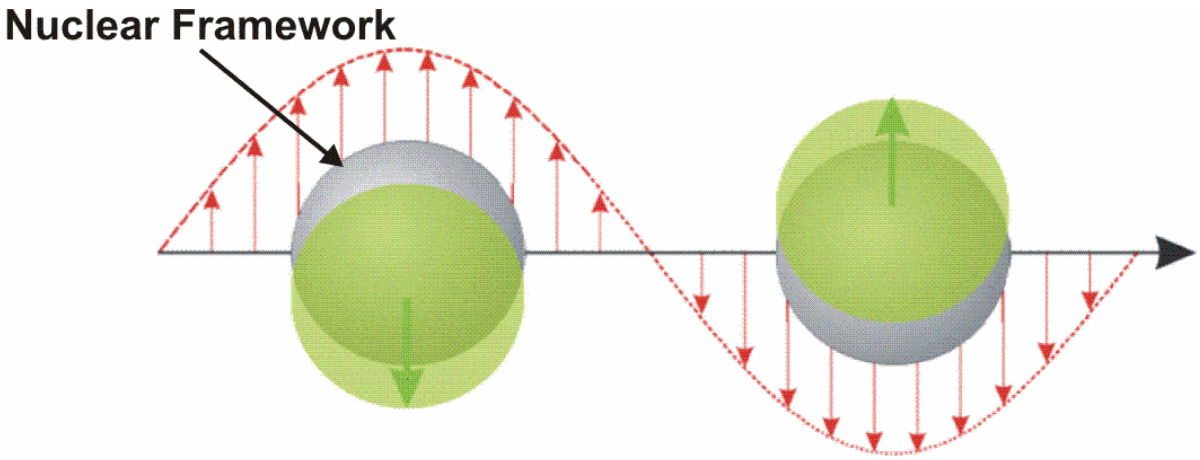

Figure 1.1 Depiction of the response of a nanoparticle's conduction band electrons under electromagnetic excitation.

"gas" is disturbed by incoming radiation the electrons respond to the electromotive force of the radiation; oscillating in response to the oscillating radiation field. Now that we understand how a metal's outer shell electrons oscillate we must move on to understanding how to analyze this motion. The following argument is based on the treatment put forth by Feynman *et al*.[38]

As has been discussed, electrons are physically moving during a plasmon excitation by oscillating about the nanoparticle's center of mass. This motion is harmonic, which implies that we must employ the equation describing harmonic motion. The equation of motion for an electron displaced by an electric field (excluding damping) is:

$$m_e \frac{d^2x}{dt^2} = -q_e E \tag{1.1}$$

where q_e is the charge of an electron, E is the electric field felt by the electron, and the product q_eE is the force felt by a charged species in the presence of the electric field. Since E is a function of x, the solution of this differential equation is evident from inspection. Using the exponential notation one can express it as:

$$x = e^{i\omega} \tag{1.2}$$

It is clear that we can solve for the plasma frequency (ω) if we can find an expression for the electric field. So the trick is to relate a property of the nanoparticle to the oscillating electric field. This will allow us to express the plasma frequency in terms of this property. Well, what is the basic property of the nanoparticle that is being affected by incoming electric field? Remember that the electrons are being physically moved by the electric field. At some point in

time, *t*, the electrons are displaced some distance *x*. Hence, the electrons that were positioned at the edge of the nanoparticle in the *x* direction are now the electrons farthest displaced from the nanoparticle core. This means that there is a greater restoring force acting on these electrons than the electrons that were displaced from the edge of the nanoparticle in the *–x* direction. Therefore, not only is a nanoparticle's electron cloud displaced by an electric field, but it is also compressed: i.e. a change in the density of a nanoparticle's conduction band electrons. We have now deduced that the charge density has been altered during a plasmon oscillation. It turns out that we can relate the charge density to the electric field through the first of Maxwell's equations:

$$\frac{\partial E_x}{\partial x} = \frac{\rho}{\varepsilon_0} \tag{1.3}$$

Here I have expressed Maxwell's first equation in one dimension since we will assume for simplicity that the electrons are displaced in one dimension (the electric field, *E*, only has a component in the x direction). The charge density (ρ) is simply the electron density multiplied by the electron charge. We have now related the plasma frequency to a fundamental property of a nanoparticle. So we see that that the plasma frequency is the natural frequency of density oscillations of the free electrons. This explains the behavior of a nanoparticle's outer shell electrons when it is irradiated with electromagnetic radiation. It does not, however, explain how one detects a plasmon resonance. To do this, we must understand the nature of moving charges.

All accelerating electric charges radiate energy. Since the electrons of the metal continually accelerate (defined as a change in velocity *or* direction) as they oscillate back and forth across the particle's center of mass they radiate energy of a frequency defined by the frequency of their oscillation. This is what we detect as the surface plasmon scattering, and what

yields the beautiful images of single nanoparticles when viewed in a microscope under high magnification (Figure 1.2). Nanoparticles scatter light elastically, which is known as Rayleigh scattering. Note that not every frequency of radiation will induce a *collective* oscillation resulting in a resonance response in nanoparticle systems. The frequency of these resonant oscillations is defined by the physical boundaries of the nanoparticle surface, the dielectric properties of the nanoparticle material, and the dielectric properties of the surrounding media.[33, 39] It is these secondary electromagnetic fields created by the oscillating electrons that create the enhanced fields responsible for SERS. But what is the nature of these resonances, and to what type of fields do they lead? Are these fields related to the simple dipolar fields from electrostatics where two point charges are separated in space, or are they something more complex? In order to answer these questions we must analyze the potentials associated with a nanoparticle system since it is then straightforward to obtain the fields by calculating the derivative of the potential.

Representing a nanoparticle as shown in Figure 1.3 we can use coulombs law to write the potential of this system as:

$$\phi = \frac{1}{4\pi\varepsilon_0}\sum_i \frac{q_i}{r_i} \tag{2.1}$$

where q_i is the charge of the ith charged species (protons and electrons), d_i is the distance from the center of the nanoparticle, P is the location at which we are measuring the potential, and r_i is the distance from the i^{th} electron to point P. If we assume that P is much greater than the size of the nanoparticle (which it is for these experiments) we can approximate r_i with R. This gives:

$$\phi = \frac{1}{4\pi\varepsilon_0 R}Q \tag{2.2}$$

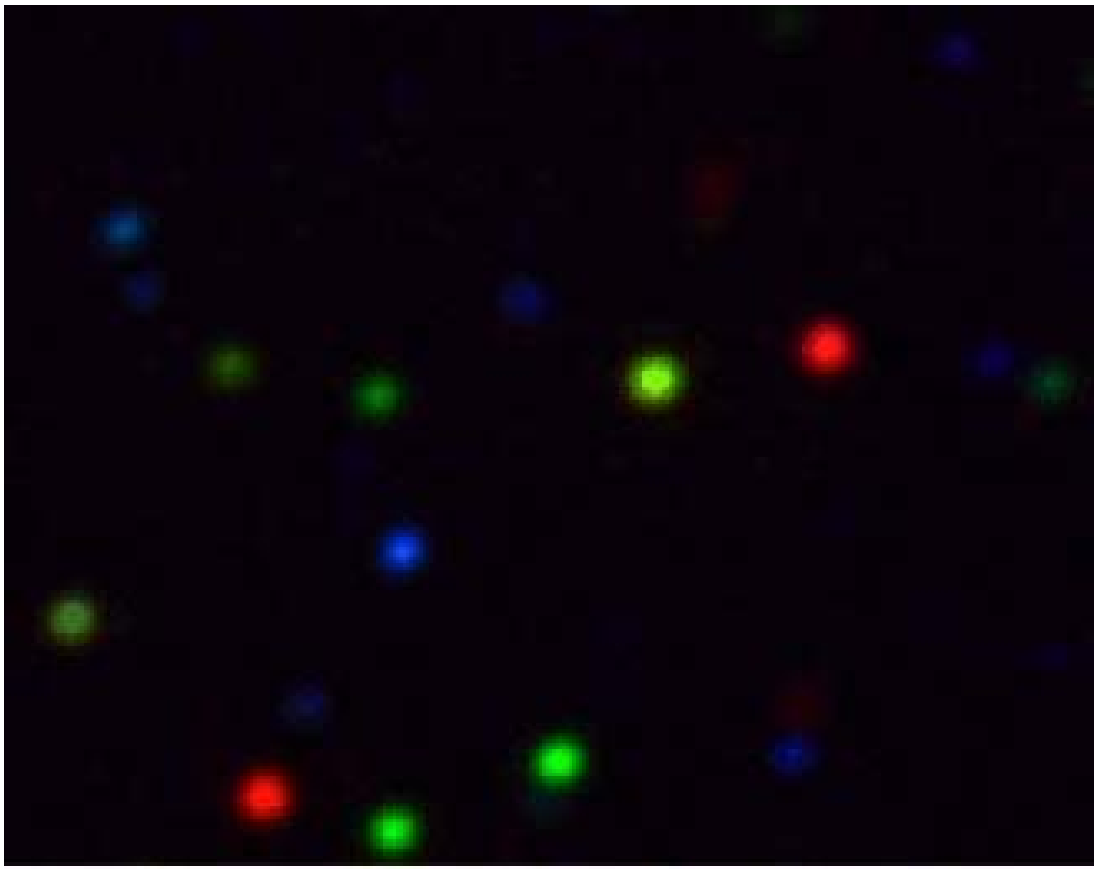

Figure 1.2 Wide field resonant Rayleigh dark-field LSPR image of colloidal silver nanoparticles on a glass slide at 100x magnification.

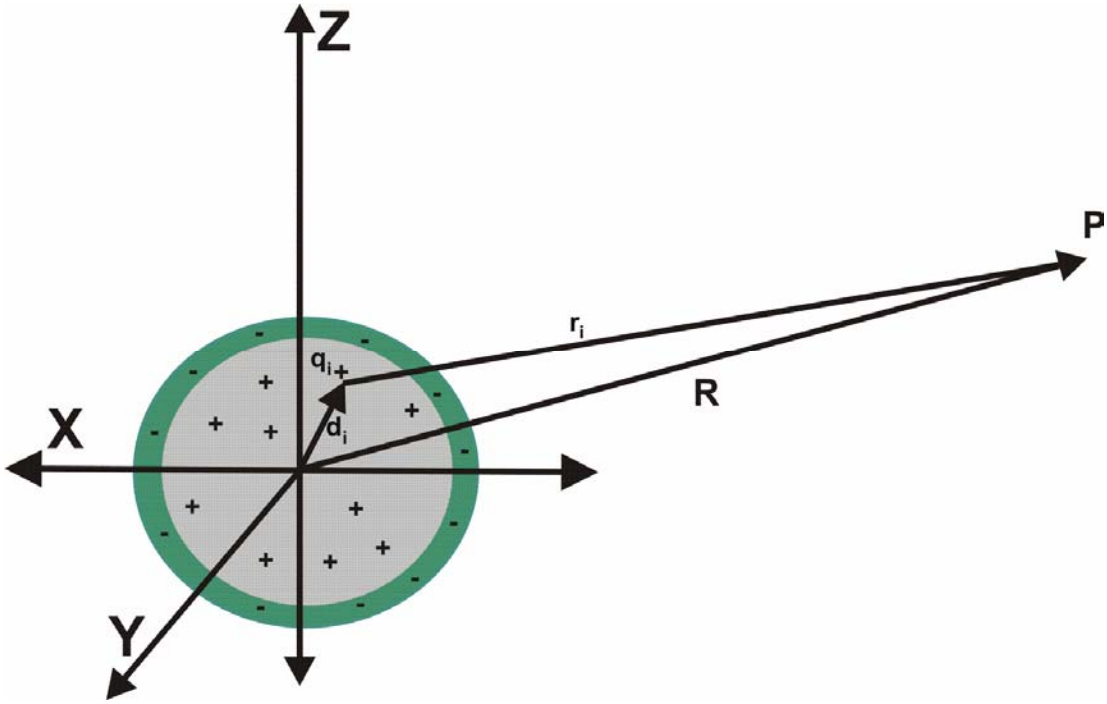

Figure 1.3 Schematic representation of the geometry for viewing a nanoparticle from an infinitely distant point (P).

where Q is the total charge on the nanoparticle. However, now we see that the potential at our observation point P is zero if the total charge is zero. However, if we are more careful we see that we did not correctly model our system. Figure 1.3 represents the relative positions of the positive and negative charges in a nanoparticle. While it may appear overall neutral when counting total number of charges present in the structure, when we look close enough we should be able to see some effect of the charges because they are not at the exact same points. This means we need a better approximation for r_i.

If we imagine that P is so far away from our nanoparticle that r_i is virtually parallel with R we see that our next best approximation for r_i is:

$$r_i \approx R - d_i \cdot e_r \tag{2.3}$$

where e_r is the unit vector along R, making the dot product of d_i and e_r the projection of d_i along R. What we really want, however, is $1/r_i$ (as seen from equation 2.1). Since d_i << R we can expand $1/r_i$ in a Taylor series yielding:

$$\frac{1}{r_i} = \frac{1}{R}\left(1 + \frac{d_i \bullet e_r}{R} + ...\right) \tag{2.4}$$

Substituting this into equation 2.1 gives:

$$\phi = \frac{1}{4\pi\varepsilon_0}\left(\frac{Q}{R} + \sum_i q_i \frac{d_i \bullet e_r}{R^2} + ...\right) \tag{2.5}$$

If the nanoparticle is neutral Q is zero and the first term is zero as it was for equation 2.2. Now, however, we have higher order terms from our Taylor expansion. The first term depends on the quantity $\sum_i q_i d_i$ and scales as $1/R^2$. If we compare this expression with that of the dipole potential for two oppositely charged particles separated by a small distance:

$$\phi = \frac{1}{4\pi\varepsilon_0}\frac{p \bullet e_r}{r^2} \tag{2.6}$$

where p is the dipole moment of the two charges and r is the distance between the charges, we see that the two expressions are exactly equal if $p = \sum_i q_i d_i$. This relationship is defined as the dipole moment of a charge distribution. Hence, dipolar fields, not a more complex field, will be dominant in metal nanoparticle systems. In fact, dipolar fields are dominant for any collection of charges that are, on the whole, neutral. This is why they are so important in physics and chemistry. The reader should note that the expression for the dipole potential was found by taking the *first* term of a Taylor expansion. Each higher order term in the Taylor expansion represents a type of mode for charge distributions. The second term, for example, represents the potential for a quadrupole mode. These modes will be discussed in more detail as necessitated by experimental results later in this thesis. A full derivation of the expression of the electromagnetic fields associated with plasmon excitations is beyond the scope of this thesis. The final result will simply be presented here for completeness and I refer the reader to an excellent review on the subject.[40]

In the limit of the nanoparticle radius (a) being much smaller than the wavelength of light ($a/\lambda < 0.2$) the electric fields around a nanoparticle appear static. This allows Maxwell's equations to be solved for a *sphere* in the quasi-static limit to yield:[33, 40]

$$E_{out}(x,y,z) = E_0\vec{z} - \left[\frac{\varepsilon_{in} - \varepsilon_{out}}{\varepsilon_{in} + 2\varepsilon_{out}}\right] a^3 E_0 \left[\frac{\vec{z}}{r^3} - \frac{3z}{r^5}\left(x\vec{x} + y\vec{y} + z\vec{z}\right)\right] \tag{2.7}$$

where ε_{in} is the dielectric function of the metal, shown in Figure 1.4**,** and ε_{out} is the dielectric function of the embedding medium. Since ε_{in} is the only wavelength dependent term in this

expression (ε_{out} is constant at optical wavelengths), the maximum field at the nanoparticle surface is reached when $\varepsilon_{in} = -2\varepsilon_{out}$.

1.3 Overview of Plasmonic Systems

The original plasmonic system used to observe SERS was the roughened silver electrode.[36] While this system served to prove the necessity of nanoscale features in the SERS phenomenon, details of the surface itself were unknown for two reasons. First, the process by which the surface was prepared was inherently random. Second, the tools required to characterize such small systems were yet to be invented. These made a quantitative theoretical understanding of SERS practically impossible at the time since a correct model of the enhanced electromagnetic fields at the metal surface required a detailed knowledge of the surface geometry. This need, along with other plasmonic applications to be discussed in the next chapter and the advent of new characterization and fabrication tools in the 1980s and 1990s, led to massive research efforts to understand and tailor the plasmonic properties of the noble metal nanopatterned surfaces.

Original approaches to fabricate such systems sought to develop techniques that could produce large areas of nanoparticles on a substrate while maintaining the ability to tune particle size, shape, material, and spacing. Today's standard approaches to this type of pattering are

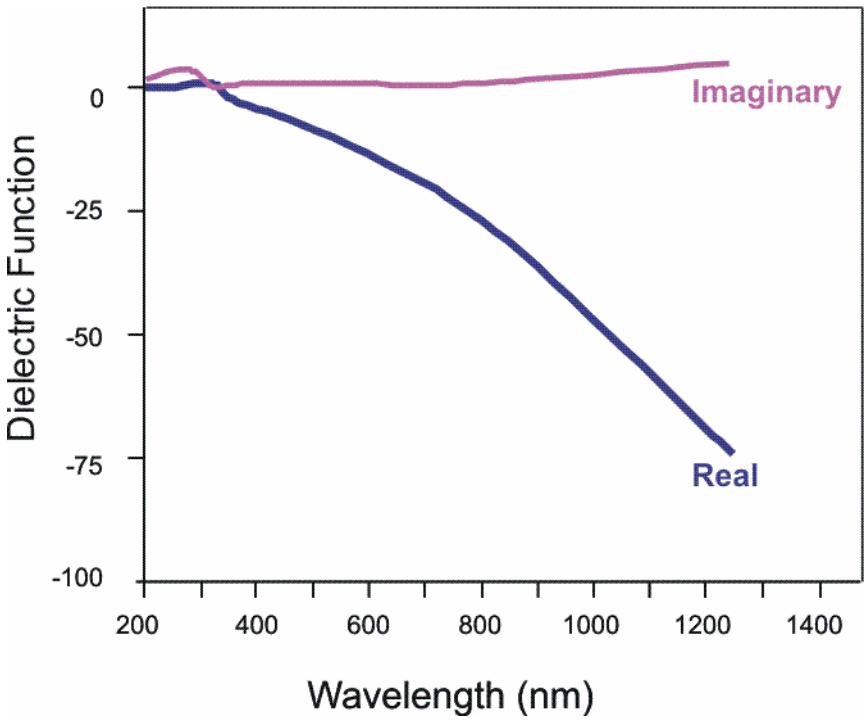

Figure 1.4 Plot of the real and imaginary components of the silver dielectric function.

photolithography,[41] electron beam lithography (EBL),[42] and focused ion beam lithography (FIB).[43] Photolithography is a massively parallel approach to designing nanostructured surfaces, and is the current industrial standard due to its speed and relative low cost as compared to the other two methods. Photolithography uses prefabricated pattern masks and light to create a pattern in a photosensitive polymer resist. Therefore, one is limited in tunability by the number of pattern masks one has, and in resolution by the diffraction limit of the light used in exposing the photoresist. EBL and FIB allow for arbitrary shapes and patterns to be written on a substrate surface. In addition, the use of an electron beam instead of light waves allows for far greater resolution to be achieved in EBL and FIB than with photolithography. However, the high cost associated with these processes encouraged the development of alternative parallel lithographic techniques.

Two approaches developed in the Van Duyne lab are film over nanospheres (FON)[44] and nanosphere lithography (NSL).[45] In these approaches aqueous suspensions of polystyrene or silica spheres (100-20000 nm radius) are drop coated onto a hydrophilic substrate surface. These substrates are generally glass,[46] but have included mica,[47] silica,[48] copper,[49] and indium tin oxide.[50] The spheres are forced to self assemble into a hexagonal close packed arrangement at the evaporation front of the water layer due to capillary forces. Various metals (silver, gold, copper, etc) are then deposited onto the so-called “sphere masks” via thermal or electron beam evaporation to create the metallic substrates.

For a FON the metal layer is made thick enough (of order 200 nm) such that none of the spheres in the sphere mask are exposed to the environment after metal deposition. This process yields substrates with random nanoscale roughness features that lead to extremely reproducible

large enhancement factors for SERS experiments.[44] While these substrates have proven extremely useful for developing biological and chemical sensors based on SERS,[51, 52] their extremely broad plasmons make detailed studies of the relationship between the LSPR and SERS unrealistic.

NSL, however, leads to well ordered nanoscale structures with well defined, Lorentzian plasmon resonances. In NSL, as opposed to FONs, metal is deposited such that discrete particles are formed in the gaps which form at the intersections of a sphere mask's hexagonal array. This means that NSL nanoparticles can have heights of ~15-75 nm. The shape defined by these gaps are truncated tetrahedra.[45] It has been shown that the plasmons of these nanoparticles are broadly tunable by fabricating particles with various combinations of height, controlled by the thickness of metal deposited, and size, controlled by the size of sphere used to make the sphere mask.[53] These nanoparticle substrates have allowed beautiful experiments correlating plasmon spectral position with SERS enhancements for various laser excitation energies.[54, 55] SERS, however, was not the only system in which NSL nanoparticles proved useful.

As stated previously, the energy of a nanoparticle's plasmon resonance is dependent on its external dielectric environment. This means that, in principal, nanoparticle plasmons could be a transduction mechanism to sensing a change in a nanoparticle's environment. More specifically, if the nanoparticle surface is engineered properly to bind a specific target analyte, nanoparticles could serve as chemical/biological sensors. In 2001 Van Duyne and coworkers demonstrated that an array of NSL derived nanoparticles could be used as biological and chemical optical nanosensors by monitoring the shift in the nanoparticles' plasmon resonance extinction (absorption + scattering) peak when small molecular adsorbates bound to the

nanoparticles' surface.[56] In 2002 Haes and Van Duyne extended this work to show that NSL nanoparticle sensors could be used to extract binding constants and showed their limit of detection (LOD) to be in the low-picomolar to high-femtomolar range for the model biotin-streptavidin system.[57] While this was a landmark result, the question of the ultimate LOD for LSPR based sensors was posed.

One obstacle to improving the LOD in the NSL paradigm is signal. In a standard sensing experiment with NSL nanoparticles the plasmon resonance is detected via conventional UV-Vis spectroscopy. This is a bright-field technique where the optical signature of the nanoparticles is detected as a loss in the illumination from the spectrometer's source. Hence, a critical number of nanoparticles must be in the illumination spot in order for the plasmon signal to be greater than that of the system noise. This implies that the LOD in such an experiment is not necessarily a fundamental limit, but a function of the system. Obviously, if one could use a single nanoparticle as the entire sensing modality this obscurity would be removed.

In 2003 McFarland and Van Duyne explored the use of colloidal single nanoparticles as chemical sensors.[58] The transition to single nanoparticles brought improvements beyond simply removing the experimental system as a limiting factor in the LOD. NSL particles, along with all other lithographically derived nanoparticle systems, have broader plasmon linewidths due to the noncrystalline nature of their internal structure. This is a result of forming the nanoparticles by depositing metal onto a surface as opposed to synthesizing the nanoparticles chemically as is done with the single nanoparticles used by McFarland and Van Duyne. These chemically synthesized nanoparticles are single crystalline, yielding a linewidth that is intrinsically narrower than lithographically derived particles. This is an advantage since narrow resonances improves a

system's resolution (ability to detect small changes in a measured signal). Single nanoparticle systems have another advantage over many lithographic techniques in that they do not suffer from array defects broadening their plasmon resonance. Figure 1.5 illustrates these types of defects in an NSL array. The final advantage of single nanoparticles is their cost and general ease of production (certain particle types notwithstanding). One can synthesize the simplest nanoparticle colloidal suspension in three hours and produce millions of nanoparticles that can retain their optical properties for years.

Recently, wet chemical synthetic approaches have been developed for new nanoparticle shapes. These shapes include triangular prisms,[59] rods,[60] cubes,[61] right bipyramids,[62] and stars,[63] just to name a few. These developments are important since it has been shown that the plasmon resonance, and it's sensitivity to its environment, to be highly dependant on shape.[33, 58] Therefore, much work has been done to understand the modes of these new nanoparticle systems, and their utility as chemical/biological sensors.[64] With the most rudimentary nanoparticle shape (sphere) yielding sensitivities in the zeptomole range,[58] the future of single nanoparticle applications seemed bright.

1.4 Goals and Organization

I hope this introduction has given the reader a context in which to place the work to be presented in this thesis. This work seeks to expand the work on colloidal single nanoparticle systems to encompass a class of more exotic nanoparticles, and verify that current theoretical

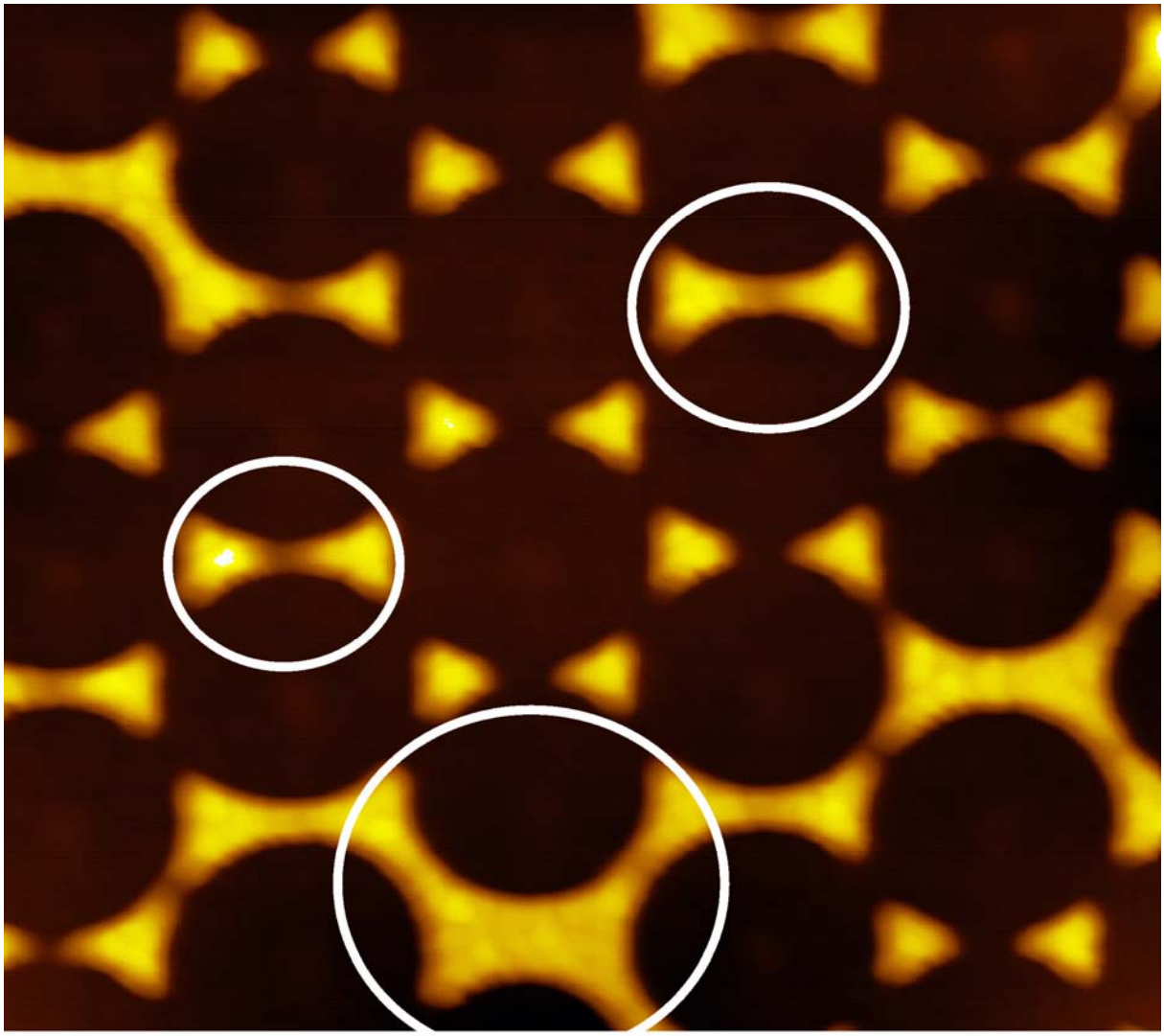

Figure 1.5 AFM image of an NSL nanoparticle array (fabricated using a 500 nm sphere mask) illustrating typical defect structures.

methods accurately model single nanoparticle optical resonances. This thesis will be divided into two parts, with each part containing two chapters. Part I will address single nanoparticle spectroscopy and sensing experiments. Chapter two will discuss single nanoparticle experiments performed on single silver triangular nanoprisms. Chapter three will discuss single nanoparticle experiments performed on single silver nanocubes.

Part II is motivated by Part I and will address experiments correlating LSPR spectra of single nanoparticles with measurements of their geometry. Chapter four will discuss an approach to correlating single nanoparticle scattering measurements with scanning probe microscopy measurements, and chapter five will discuss results from correlating single nanoparticle scattering measurements with high resolution transmission electron microscopy measurements.

Part I

Single Nanoparticle LSPR Spectroscopy and Sensing

I.1 Introduction

Significant attention has been given to the study of the plasmonic properties of noble metal nanoparticles as a result of their potential uses as components in a diverse range of technologies such as waveguides,[65-67] photonic circuits,[68, 69] molecular rulers,[70] and chemical/biological sensors.[47, 58, 71, 72] All of these applications are based on the localized surface plasmon resonance (LSPR) of the nanoparticle. LSPRs are excited when electromagnetic radiation interacts with a nanoparticle to create coherent oscillations (excitations) of the conduction electrons. This phenomenon has two key consequences: (1) selective photon absorption and scattering allows the optical properties of the nanoparticles to be monitored by conventional UV-Vis spectroscopy and far-field scattering techniques and (2) enhancement of the electromagnetic fields surrounding the nanoparticles lead to surface-enhanced spectroscopic techniques including surface-enhanced Raman spectroscopy. Previous studies show that the plasmon frequency is extremely sensitive to nanoparticle composition,[73] size,[39] shape,[32, 33, 74] dielectric environment,[56, 75-77] and proximity to other nanoparticles.[42, 78-80]

The last factor affecting the plasmon frequency is of no concern since in this work all particles were optically isolated. The other four conditions for the plasmon frequency can be accounted for theoretically from a relationship derived by Mie in 1908:[81]

$$E(\lambda) = \frac{24\pi^2 a^3 \varepsilon_m^{3/2}}{\lambda \ln(10)} \left[\frac{\varepsilon_i(\lambda)}{(\varepsilon_r(\lambda) + \chi\varepsilon_m)^2 + \varepsilon_i(\lambda)^2} \right] \quad \text{(I.1)}$$

where $E(\lambda)$ is the extinction magnitude, a is the radius of the metallic nanoparticle, ε_m is the dielectric constant of the medium surrounding the metallic nanoparticle (ε_m is assumed to be a

positive, wavelength-independent, real number), λ is the wavelength of the incident radiation $\varepsilon_i(\lambda)$ is the imaginary portion of the metallic nanoparticle's wavelength dependent dielectric function, and $\varepsilon_r(\lambda)$ is the real portion of the metallic nanoparticle's wavelength dependent dielectric function. The χ term in the denominator of equation 2.8 is a numerical approximation (Gan's theory) to Mie's exact solution for a sphere where the value of χ is 2.[33] This term increases in value for nanoparticles of increasing aspect ratio. The need for such an approximation was prompted by the development of lithographic and wet chemical synthetic approaches that yielded new nanoparticle geometries. EBL, photolithography, and NSL have been used to create arrays of cylindrical disks,[82] pyramids,[83] and truncated tetrahedra.[45] Wet chemical synthetic techniques based on the reduction of a metal salt have been developed to yield geometries such as rods,[84] triangular prisms,[85] cubes,[85] right bipyramids,[62] and stars.[63] Another feature of interest is the observation of multiple plasmon peaks in the far-field Rayleigh LSPR spectra of nanorods,[86, 87] triangular nanoprisms,[59] and nanocubes.[75] These are caused by either multipolar excitation, or by interaction with the surroundings, such as with an asymmetric dielectric environment. The shape factor approximation to Mie's extinction expression, however, is not sufficient to accurately model these more complex nanoparticle systems.

A number of approaches have been employed to model the optical properties of nanoparticle systems with complex geometries including the coupled dipole method,[79] multipole multipole method,[88] the modified long wavelength approximation,[89] T-matrix methods,[90] finite difference time domain method (FDTD),[75, 91-93] and the discrete dipole approximation (DDA).[94, 95] Each approach has strengths and weaknesses, and I refer the reader to discussions comparing these approaches.[33, 96] The theoretical component of this thesis is mainly concerned with the

performance of the DDA method when modeling the LSPR spectra of single silver nanoparticles. However, results from the FDTD method will also be discussed for certain circumstances where they offer useful insight into the nature of the LSPR modes.

The DDA method represents a nanoparticle as a collection of *n* cubic polarizable dipoles arranged on a cubic grid. These dipoles can be restricted in size by one's choice of grid spacing. There is a trade-off to consider when choosing this grid spacing; a smaller grid spacing yields a more structurally accurate representations of a nanoparticle at a computational cost. The advantage to this approach, however, is in its relative conceptual simplicity, ease of use, and availability of public domain software.

A major limitation to DDA is its representation of a nanoparticle's edge features. Since the dipole sources are arranged on a regular grid, there is a "staircase" representation for sharp features or angles on the structure's surface. However, there is no a priori requirement as to which sites are occupied on the cubic grid. This makes the representation of arbitrary shapes quite straightforward when using DDA.

With such a wide range of tunable parameters, spectral signatures, and sensitivity to their "nanoenvironments", nanoparticles have become good platforms for pursuing high throughput, small volume, low cost, ultrasensitive, multiplexed chemical/biological sensors.[97] However, most of these applications are based on ensemble-averaged spectral properties.[71, 97, 98] To date five different ensemble averaged nanoparticle sensing mechanisms have been demonstrated. These are (1) surface-enhanced Raman scattering,[52, 99, 100] (2) local refractive index changes,[47, 56, 58, 101, 102] (3) charge transfer interactions at nanoparticle surfaces,[103, 104] (4) resonant Rayleigh scattering from nanoparticles used as labels,[105-107] and (5) nanoparticle aggregation.[71, 108-110]

In order to better understand the design rules for practical plasmonic sensing devices, the properties of single nanoparticles, including the relationship between particle morphology, plasmon spectral position (λ_{max}), dielectric sensitivity, and sensing volume, need to be understood in greater detail. Recent theoretical work by Lazarides and coworkers has suggested that nanoparticle dielectric sensitivity is independent of nanoparticle morphology.[111] Instead they suggest that it is only the spectral position of the plasmon that determines the dielectric sensitivity of a nanoparticle. A caveat to this assertion is that this will be true only when the particle is in a homogenous dielectric environment. This is critical since many measurements on nanoparticles are performed in an inhomogeneous dielectric environment (e.g. particles on surfaces or particles that are chemically functionalized in an asymmetric manner).

Part I: Chapter 2

Single Nanoparticle Localized Surface Plasmon Resonance Spectroscopy of Single Silver Triangular Prisms

2.1 Introduction

The development of a technique to synthesize atomically flat triangular nanoprisms elicited great excitement in the field of nanoparticle optics since their growth is induced by shining light on a suspension of small gold or silver colloids.[59] This was an unprecedented result, and presented a new approach to nanostructure synthesis. Jin *et al* was able to tune the average size of the prisms produced by varying the wavelength of the light used to irradiate the seed solution.[74] The mechanism behind this optically driven growth process is still under debate although a mechanism has been suggested in the literature by Brus and coworkers.[112] The only fact for certain on the subject is that the localized surface plasmons (LSPR) of the prisms are integral in the process.

The excitement about this development was not limited simply to the synthetic novelty of the process. The structure itself was of great interest to the plasmonics community. This interest was based on previous work done by Van Duyne and coworkers with arrays of truncated tetrahedral nanoparticles due to the geometric similarity between the two structures. These studies revealed a number of interesting properties of triangular nanoparticles. First, the enhanced local electromagnetic (EM) fields associated with the LSPRs of the nanoparticles extend farther from the nanoparticles' surface for thinner nanoparticles.[113, 114] Second, these EM fields were most intense at the triangles' tips.[113, 115] Third, these particles were excellent SERS substrates.[54]

As stated above, changing the wavelength of the light source allows one to tune the size of the final nanoprisms. But how well controlled are these sizes? This is always an issue when dealing with the synthesis of nanoparticle suspensions. They are inherently heterogeneous

systems in which the subtleties of each individual particle's properties are obscured. These issues are addressed here by studying the LSPR spectroscopy and dielectric sensitivities of single silver triangular nanoprisms. Although there have been previous studies on triangular nanoprisms[59, 74] the present studies are the first for single nanoparticles. It will be important to see how the results compare, as much of the interpretation of the nanoparticle spectra have involved comparing ensemble averaged results with theory done for single nanoparticles. These earlier comparisons have provided significant information about the nanoparticle properties, including the assignment of the modes of plasmon excitation which are responsible for each of the three experimentally observed plasmon peaks.[59] They also have demonstrated the exceptional degree of tunability which this structure allows through changes in height, width, and tip sharpness.[74] By judiciously selecting nanoprisms with one or more plasmon modes that have the same λ_{max} three of the four nanoparticle observables mentioned previously (λ_{max}, dielectric sensitivity, and sensing volume) are able to be investigated at the single particle level.

The goal of this chapter is to explore the optical properties of single silver triangular nanoprisms, and assess heir utility as chemical sensing platforms.

2.2 Materials and Methods

2.2.1 Materials

Substrates for all experiments were 18 mm diameter No. 1 glass coverslips from Fischer Scientific (Pittsburg, PA). Glassware preparations utilized H_2O_2, H_2SO_4, HCl, HNO_3, and NH_4OH from Fischer Scientific, and ultrapure H_2O (18.2 MΩ cm^{-1}) from a Millipore academic system (Marlborough, MA). Sodium borohydride (99%), trisodium citrate dihydrate, silver

nitrate (99.9999%), poly-L-lysine (98%), pentanethiol, heptanethiol, decanethiol, and hexadecanethiol were purchased from Aldrich (Milwaukee, WI). Bis(p-sulfanatophenyl) phenylphosphine dihydrate dipotassium salt (BSPP) was purchased from Strem Chemicals (Newburyport, MA).

2.2.2 Substrate Preparation

No. 1 glass coverslip substrates were prepared by a standard procedure where the coverslips were initially treated with a "piranha etch" (3:1 H_2SO_4:H_2O_2) for 30 minutes to clean the glass surface of impurities. The substrates were then rinsed with copious amounts of ultrapure H_2O until the pH of the substrates' bath stabilized at a value of 7. This was followed by sonicating the substrates for 60 minutes in a 5:1:1 H_2O:H_2O_2:NH_4OH bath in order to render the surface hydrophilic via OH^- termination. The substrates were again rinsed with copious amounts of milliQ purified H_2O, and stored in a pH neutral H_2O environment until use.

2.2.3 Sample Preparation

When ready to use, a substrate was removed from the water storage and an 2 μL aliquot of nanoprism solution was drop-coated onto the surface of a still wet glass coverslip. The substrate was then rotated by hand until the nanoparticle solution is well dispersed into the initial water layer. Substrates were then allowed to dry in either air or N_2 environments. The prepared samples were then loaded into a custom flow cell so that the nanoparticles could be studied in a controlled environment.

Suspensions of triangular nanoprisms were synthesized by an established technique pioneered by Jin *et al*.[59] This is a two step synthesis where a seed solution of silver colloids (~8 nm) serves as the starting material for triangular nanoprism formation. First, nanopure water (95

mL), aqueous trisodium citrate (1 mL of 30 mM, freshly prepared), and aqueous silver nitrate (2mL of 5 mM, freshly prepared) were mixed in a 250 mL 3 necked flask that had been cleaned with aqua regia for at least 3 hours. This solution was immersed in an ice bath and stirred for 30 minutes. During this time inert gas (Ar or N_2) was bubbled through the solution. After 30 minutes the inert gas flow was terminated, and each neck of the flask was corked with a rubber stopper. Aqueous sodium borohydride (50 mM) was then made using ice-cold ultrapure water. 1 mL of this solution was quickly injected into the ice-cold solution by a syringe through the center rubber stopper. The clear solution turned pale yellow immediately (note: if a blue color that fades to light yellow appears initially, the seed solution is unusable). The reaction was allowed to proceed for an additional 15 minutes. 1 mL of BSPP and 0.5 mL of sodium borohydride solutions (50 mM, freshly made with ice-cold water) were then added dropwise over a five minute period. The resulting suspension of small silver colloids were immediately divided into 10 mL vials and irradiated with a fluorescent lab lamp overnight. After the irradiation period the suspension changed from yellow to deep green or blue, indicating the formation of triangular nanoprisms.

A slight variation on this approach was also used in this chapter's experiments. In this synthesis the addition of BSPP was neglected in order to create nanoprisms that were capped with citrate instead of BSPP. This led to a larger heterogeneity in the structures of the nanoprisms.

2.2.4 Structural Characterization

Scanning electron microscope (SEM) images were acquired using a Hitachi 4500 field emission electron microscope (Hitachi, Japan) operating at an accelerating voltage of 5 kV.

Tapping-mode atomic force microscope (AFM) images were acquired using a Pico-Plus Molecular Imaging scanning probe microscope (Agilent Technologies, Santa Clara, CA). Pyramidal doped single crystal silicon cantilevers (Applied Nanostructures, Santa Clara, CA; radius of curvature < 10 nm, resonant frequency = 200-400 kHz, force constant = 25-75 N/m) were used to obtain all AFM images.

2.2.5 Optical Characterization

All ensemble nanoparticle extinction spectra were obtained by standard UV-visible spectroscopy. In this approach a fiber optically coupled Ocean Optics SD2000 (Ocean Optics, Dunedin, FL) spectrometer was used in standard transmission geometry with unpolarized light.

All single nanoparticle scattering spectra were obtained with either a Nikon *Eclipse* TE300 or Nikon *Eclipse* TE2000-U inverted optical microscope (Nikon, Japan) coupled to a SpectroPro 300i imaging spectrometer and a liquid nitrogen cooled Spec-10:400B CCD detector. These microscopes use tungsten filaments for illumination. This illumination was focused on the sample surface by a Nikon 0.8-0.95 numerical aperture (NA) dark-field condenser. Single nanoparticles scattered this light into the collection optics. For this approach it was critical that the NA of the objective (collection optic) was smaller than the NA of the condenser so that none of the illumination light would be collected. A Nikon variable aperture (NA=0.5-1.3) 100X oil immersion objective was chosen for this purpose. Figure 2.1 shows a schematic of this apparatus.

The following approach was used in order to acquire a single nanoparticle spectrum. First, the nanoparticle of interest was imaged at the center of the spectrometer slit, and the slit was narrowed to the diffraction limited spot size of the image of the nanoparticle. The grating was then rotated out of zero order into first order, and the dispersed light was imaged. WinSpec

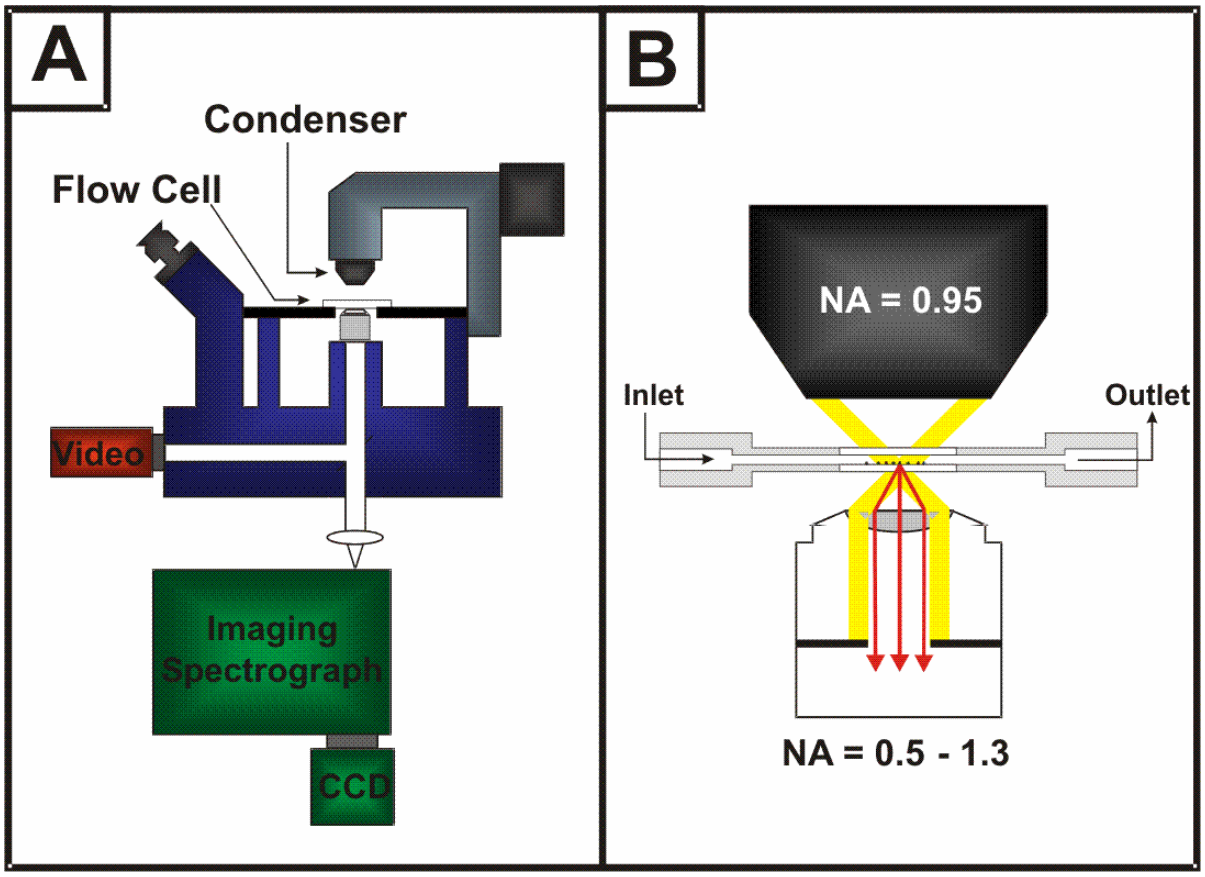

Figure 2.1 A) Apparatus for measuring dark-field scattering. B) Close-up view of the illumination and collection optics' geometry.

software (Princeton Instruments, Trenton, NJ) was used to digitally select the region of the detector chip over which the nanoparticle's scattered light was located. A region of the same size was chosen where no nanoparticle scattering existed for background subtraction. Spectra were then acquired. These two spectra alone, however, were not sufficient to obtain the true scattering spectrum of a single nanoparticle. To do this the spectrum of the illumination lamp was necessary since a tungsten filament does not radiate at a constant irradiance over all wavelengths (Figure 2.2). Hence, to obtain a true single nanoparticle scattering spectrum the background subtracted spectrum was divided by the lamp spectrum.

2.2.6 Theoretical Calculations

The DDA method was utilized to model the LSPR spectra of the single silver nanoprisms studied in this chapter. The number of dipoles used to define each nanoprism structure was determined by the number needed in order for the grid length to equal 1 nm.

2.3 Results and Discussion

Figure 2.3 shows two series of DDA calculations in which two different geometric parameters were varied. I begin with this theoretical data set since it illustrates how the different geometric changes affect the LSPR spectra of nanoprisms. The first thing to note about the spectra is that triangular nanoprisms show two LSPR resonance peaks. The more intense, lower energy, peak is assigned as a dipole mode, and the smaller, higher energy, peak is assigned as a quadrupole mode.[59] In fact, nanoprisms have other optical LSPR modes that are not revealed in this set of DDA calculations or the single nanoparticle experiments to be shown later in this chapter. This is due to the geometry by which the light impinges on the nanoprisms. It can be

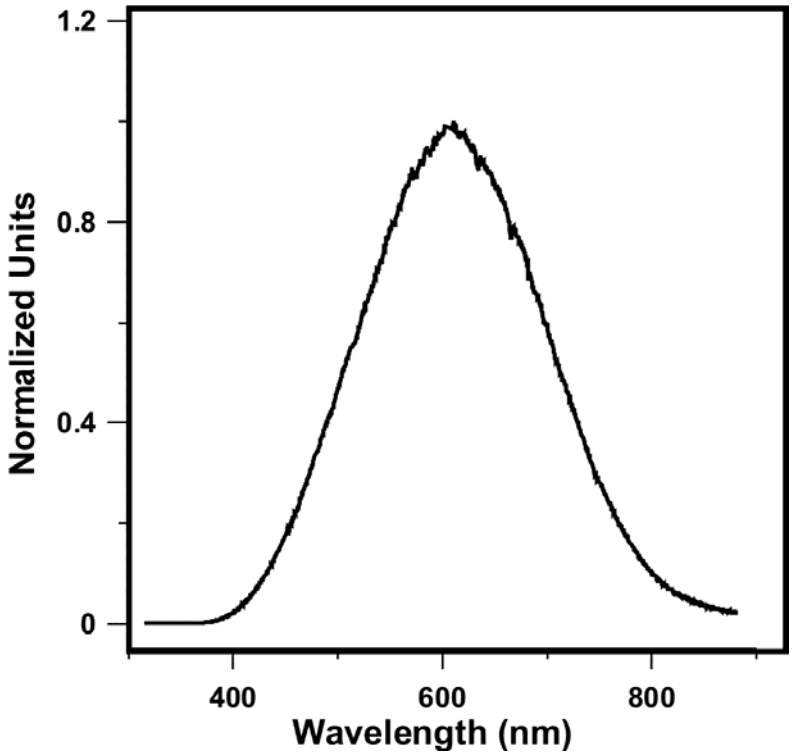

Figure 2.2 Irradiance profile of the lamp used for all transmission dark-field measurements.

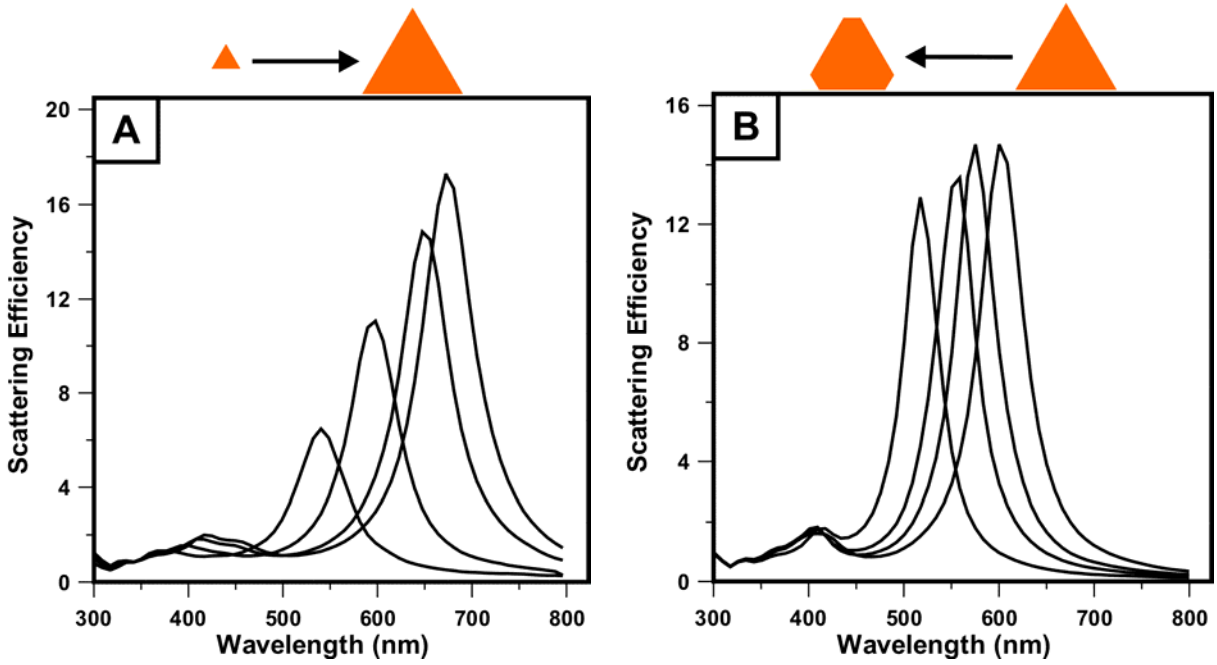

Figure 2.3 DDA calculations demonstrating the effect on the LSPR spectra of single silver triangular nanoprisms for A) changing the size of a nanoprism with perfectly formed tips and B) progressively snipping the nanoprisms' tips.

seen from Figure 2.1, that the light's axis of propagation is orthogonal to the substrate surface. Since the electromagnetic field is orthogonal to the light's propagation direction, and the nanoprisms are laying flat on the substrate surface, the dipole and quadrupole modes seen in the DDA results and experiments are associated with the "in-plane" axis of the nanoparticles. There are, of course, out-of-plane modes, but these modes are not accessible by these experiments and will not be discussed further. It is also important to note that changes in a nanoprism's thickness also affect the dipole and quadrupole resonances (both modes blue-shift with increasing thickness). However, the vast majority of nanoprisms synthesized for these studies have a thickness of 10 nm $\pm$ 2 nm. Hence, all nanoprisms in this study are considered to be 10 nm thick.

Part A of Figure 2.3 shows that both the dipole and quadrupole LSPRs for a perfectly formed nanoprism red-shift as the nanoprism increases its in-plane size. Part B of Figure 2.3 shows that only the dipole LSPR mode is affected for a change in a nanoprism's tip structure (up to ~25% change in the original nanoprism's total size at which point the qaudrupole also begins to shift). This change in a nanoprism's tip structure will hereafter be referred to as "tip snipping". For increasing tip snipping the dipole resonance blue-shifts while the quadrupole mode remains unchanged. This implies that dipoles are excited at a nanoprism's tips while the quadrupole is excited at a nanoprism's center as shown in Figure 2.4. Now that we have a basic understanding of how geometry affects a nanoprism's LSPR spectrum let's turn to a discussion of experimental results.

Figure 2.5 compares triangular nanoprism LSPR spectra from three different sources: transmission UV-Vis spectroscopy (ensemble of nanoprisms in solution), resonant Rayleigh

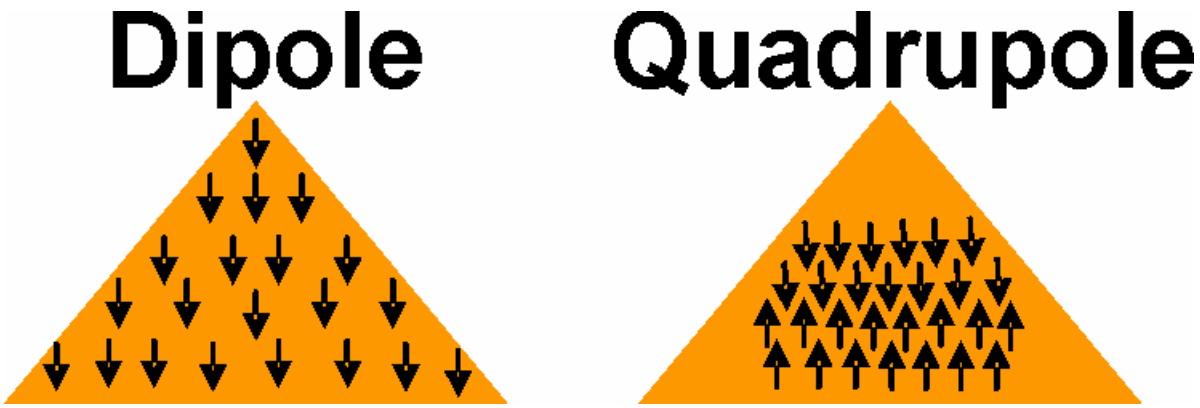

Figure 2.4 Representation of the regions where the dipole and quadrupole LSPRs are excited in triangular nanoprisms.

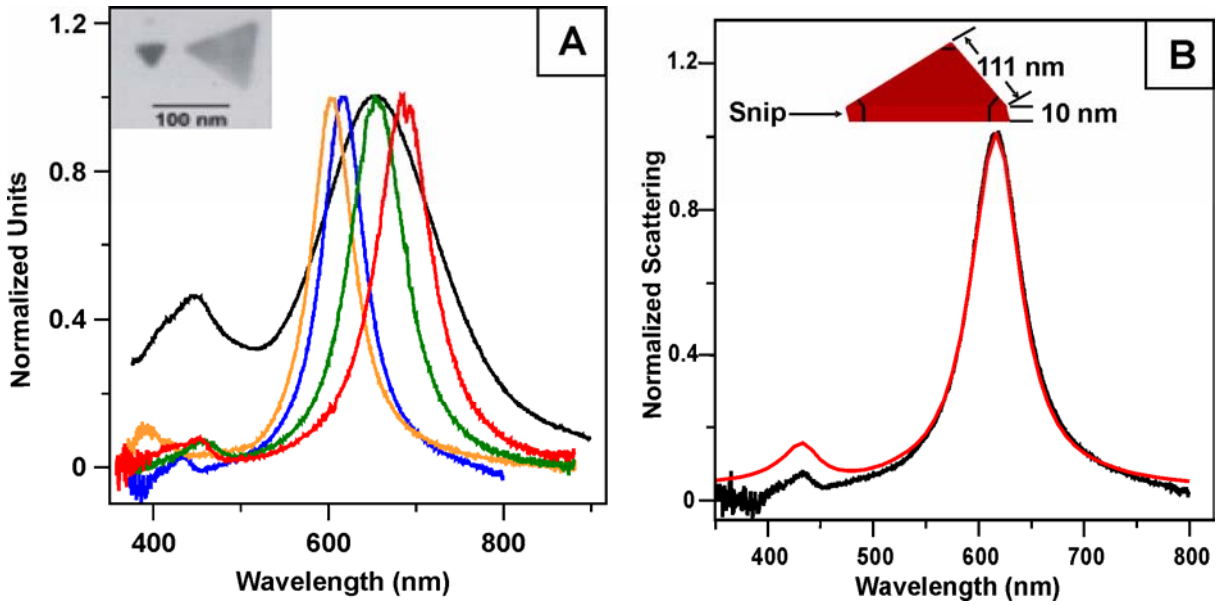

Figure 2.5 LSPR spectra of silver triangular nanoprisms: A) Ensemble extinction spectrum (black curve) vs. single nanoparticle dark-field scattering spectra (colored curves) of triangular nanoprisms (representative nanoprisms shown in TEM inset). B) Theoretical modeling (red curve) of a single triangular nanoprism using the DDA method. The theoretical spectrum was calculated for a nanoprism with edge length = 111 nm, snip = 15 nm, and height = 10 nm.

scattering spectroscopy (single nanoprism), and DDA calculations (single nanoprism). The prisms in these samples were made using BSPP. Figure 2.5A compares the ensemble extinction spectrum (scattering + absorption) of an aqueous solution (refractive index = 1.33) of nanoprisms to the spectra of four different single nanoprisms that are also immersed in an aqueous environment. These single nanoprism scattering spectra illustrate the degree of geometric diversity contained in a given aliquot of a nanoprism solution. The inset is a TEM image of nanoprisms taken from the aqueous solution, but these prisms are not the specific nanoprisms responsible for any of the depicted spectra. Figure 2.5B compares the spectrum of a single nanoprism acquired in an inert nitrogen environment (refractive index = 1.000297) with a nanoprism spectrum calculated with the DDA method.[94, 95] This spectrum shows typical behavior for a prism[59] in which there is a strong dipole resonance at 620 nm, and then a weaker in-plane quadrupole resonance at 433 nm. A third plasmon resonance, due to out-of-plane quadrupole excitation, which has previously been noted at 325 nm, is not accessible in our measurements as discussed earlier. The particle structure parameters used to calculate this spectrum were not exactly from physical measurements of the nanoprism yielding the experimental spectrum. Instead, the geometric parameters used in the calculation in Figure 2.5B were allowed to vary until the experimental result was sufficiently reproduced. AFM measurements on several different nanoprisms, shown in Figure 2.6, reveal that the geometric parameters used to model the experiment fall well within the range of measured values. These images explicitly show the lack of geometric homogeneity in the nanoprism samples; in particular the variation in edge length and tip sharpness.

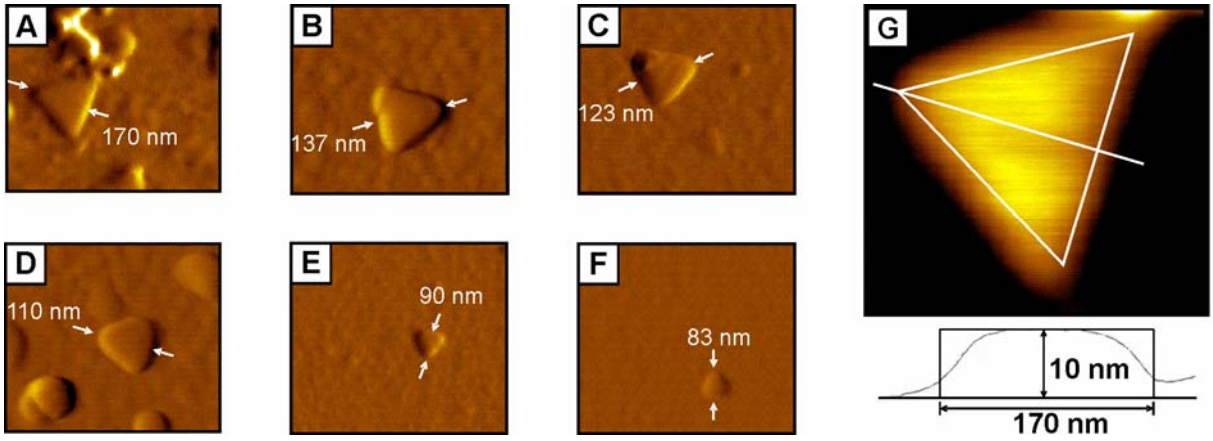

Figure 2.6 A-F) AFM measurements showing the diversity found in a typical 2 μL aliquot of a suspension of triangular nanoprisms. G) Height cross-section for the nanoprism shown in (A).

Figure 2.7 shows LSPR spectra of nanoprisms synthesized without the use of the BSPP surfactant. This was done since it was discovered that straight-chain alkanethiols do not displace the surfactant, making it difficult to functionalize the BSPP-coated particles for sensing applications. Figure 2.7A compares the ensemble extinction LSPR spectrum to three single LSPR scattering spectra. As one can see, the ensemble averaged spectra show considerably less homogeneity in the lineshape of the in-plane quadrupole peak at ~ 465 nm, reflecting the contribution of particles in the sample that are not nanoprisms. The single nanoprism spectra displayed in Figure 2.7A have been deliberately chosen to have overlapping in-plane dipole LSPR peak positions so as to address the relative importance of geometry vs. plasmon resonance position in nanoparticle refractive index sensitivity.

Figure 2.7B shows a single nanoprism from Figure 2.7A (blue curve) in a variety of different bulk dielectric environments. It should be noted that prior to all our experimental measurements the nanoparticles were solvent annealed by incubating the nanoprisms in ethanol for at least twelve hours. This is necessary since nanoparticles can undergo geometrical changes when initially exposed to a solvent environment.[56] After the annealing process, LSPR spectra of the nanoprisms were acquired in nitrogen after brief incubations (~10 minutes) in methanol, ethanol, and 1-propanol; this assured us that the LSPR spectrum would not suffer any additional shifts due to further solvent annealing. Once the geometric integrity of the nanoprisms was established, their refractive index sensitivity was measured (Figures 2.7B and 2.7C). These data show that the nanoprisms' dipole and quadrupole plasmon resonances respond linearly to changes in the refractive index of their environment, and that the dipole's response is stronger than the quadrupole's.

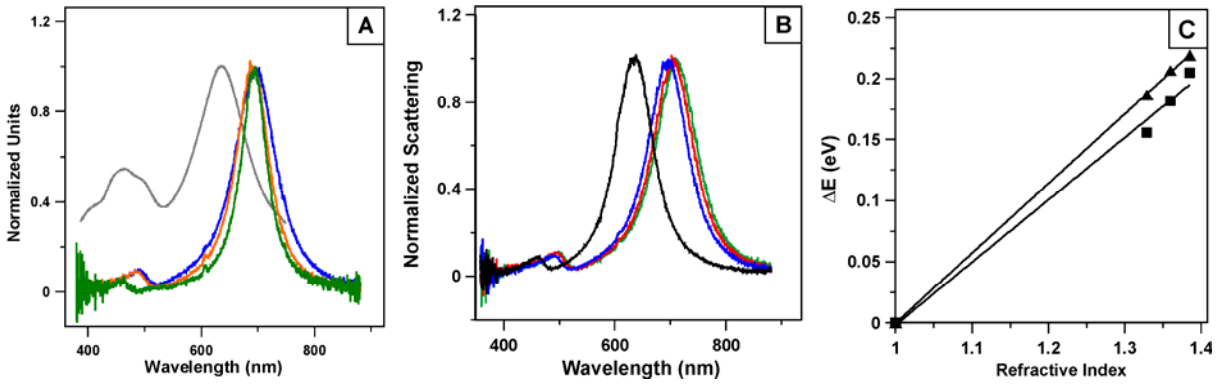

Figure 2.7 A) Ensemble extinction spectrum (grey curve) vs. single nanoparticle LSPR scattering spectra of silver triangular nanoprisms synthesized without surfactant. B) Single nanoprism dark-field scattering spectra in four different dielectric environments (refractive indexes = 1.000297, 1.329, 1.359, 1.383) demonstrating the nanoprism's sensitivity to its environment. C) Linear regression fit to the experimental data. Triangles represent dipole data (m = 0.571 eV RIU^{-1}, R^2 = 0.999,) and squares represent = quadrupole data (m = 0.512 eV RIU^{-1}, R^2 = 0.992).

Tables 1 and 2 list the peak position, refractive index sensitivity, plasmon linewidth, FWHM, and figure of merit (FOM) for each of the three single nanoprisms shown in Figure 2.7A. The FOM,[75] which is defined using:

$$\text{FOM} = \frac{m \text{ (eV RIU}^{-1})}{FWHM \text{ (eV)}} \tag{2.1}$$

functions as a standard measure for assessing a nanoparticle's sensing potential. The results show that the bulk refractive index sensitivities of nanoprisms vary significantly (~ 11 %) despite overlapping dipole λ_{max}'s (at most a 0.6 % change in dipole LSPR peak position). This demonstrates that the Lazarides argument is not valid (as expected) when a nanoparticle is in an inhomogenous dielectric environment (nanoparticles on a glass substrate).

The results in tables 2 and 3 provide an important opportunity to study the influence of plasmon linewidth on particle structure. Previous experimental and theoretical studies have demonstrated the sensitivity of λ_{max} to changes in particle geometry (i.e. edge length, thickness, and tip sharpness),[33, 59] and the present results are consistent with past expectations. However the variation of the plasmon linewidth with changes in nanoprism structure, holding λ_{max} constant, has not been studied even though this is an important component of the FOM. The data in tables 2 and 3 demonstrate substantial variation in the plasmon linewidth, and this plays an important role in determining the FOM. The absence of information about particle structure in these measurements limits our ability to explain what factors are important in determining this behavior; however the DDA calculations can be used to provide qualitative insight.

Previous studies have shown that there are two distinct regimes (intrinsic and extrinsic) of the plasmon bandwidth for high symmetry (spheres, rods, etc.) noble metal nanoparticles.[35, 116] The intrinsic regime applies to nanoparticles with radii smaller than their mean free electron

	Dipole λ_{max} (nm)	Dipole Sensitivity (nm/RI units)	Dipole Sensitivity (meV/RI units)	FWHM (meV)	FOM
Nanoprism 1	630.6	204.9	571.1	246.3	2.319
Nanoprism 2	634.6	182.9	511.4	195.3	2.619
Nanoprism 3	631.4	196.4	549.1	165.8	3.294

Table 2.1 Peak positions and pertinent experimental environmental sensitivity parameters for the dipole resonance of three different nanoprisms with approximately equal dipole λ_{max}'s.

	Quad λ_{max} (nm)	Quad Sensitivity (nm/RI units)	Quad Sensitivity (meV/RI units)	FWHM (meV)	FOM
Nanoprism 1	459.3	93.99	511.6	284.1	1.801
Nanoprism 2	460.8	80.64	440.8	267.5	1.648
Nanoprism 3	439.6	78.62	481.8	166.7	2.890

Table 2.2 Peak positions and pertinent experimental environmental sensitivity parameters for the quadrupole resonance of three different nanoprisms with approximately equal dipole λ_{max}'s.

	FWHM (meV)	Dipole Shift (nm)	Dipole Shift (meV)	Reference Shift (meV)	% Reference Shift (meV)	Quad Shift (nm)	Quad Shift (meV)
Nanoprism 1	246.3	19.84	59.96	71.15	84.27	16.81	96.10
Nanoprism 2	195.3	11.56	34.97	71.15	49.15	4.44	25.46
Nanoprism 3	165.8	14.69	46.80	71.15	65.78	6.14	38.83

Table 2.3 LSPR λ_{max} shift data acquired after surface modification with decanethiol for three different nanoprisms with approximately equal dipole λ_{max}'s.

path. In this regime, the surface of the nanoparticle becomes the dominant scattering source for the conduction electrons, and thereby determines the lifetime of the excited electrons. Smaller radii lead to shorter lifetimes, and, hence, larger bandwidths. The DDA calculations have not included the intrinsic effect; however we note that the good agreement between theory and experiment in Fig. 1B suggests that this must not be very important for the particle sizes studied here.

The extrinsic regime applies to nanoparticles with radii larger than their mean free electron path. In this regime, electron-electron, electron-phonon, and electron defect scattering dominate, which are contributions that should be size independent. However, broadening of the plasmon bandwidth with increasing particle size does occur as a result of radiative damping. This arises when the induced dipole in the particle emits light at a rate that competes with the rate of excitation of the particle. For spherical particles this effect scales with the square of the volume of the particle, and it becomes important for particles with diameters larger than 100 nm. In the case of the nanoprisms, our DDA calculations (Figure 2.8) show that the bandwidth does not increase with increasing edge length (considering edges in the 80-200 nm range) or with particle height (for 8-15 nm heights). This is consistent with the idea that the particle volume is too small for radiative damping to be important.

However, our DDA calculations show that there is one structure that is important in determining the LSPR linewidth, the sharpness of the tips of the particles: i.e. the sharper the tips the broader the linewidth. Figure 2.8 shows that only the prisms with perfectly sharp tips have

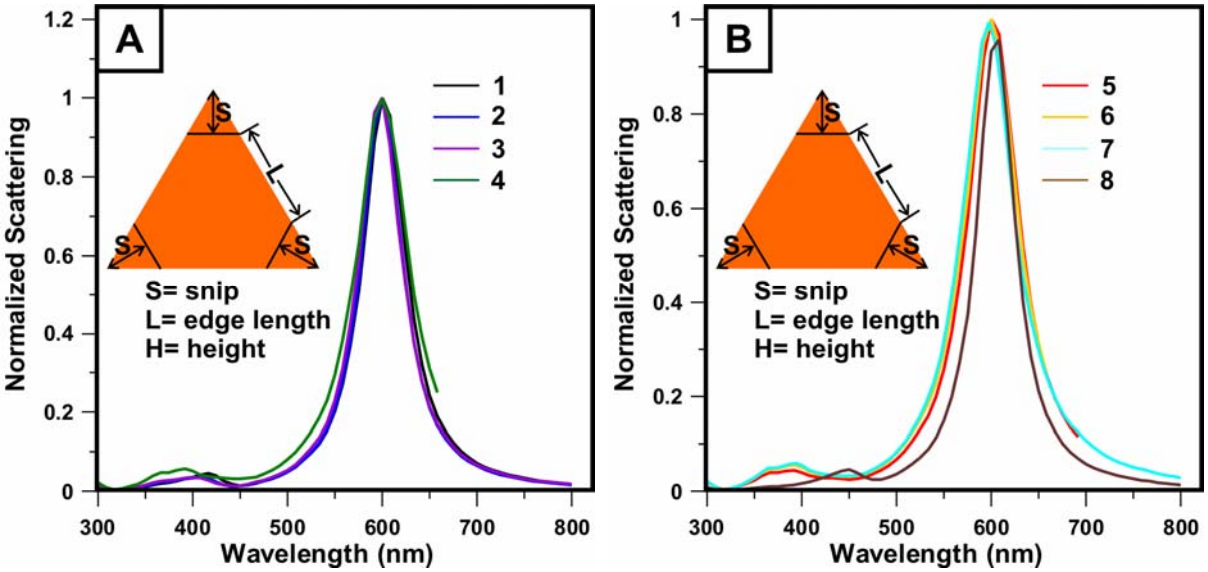

Figure 2.8 DDA calculations for a series of nanoprism dimensions to compare linewidth as a function of geometry at a fixed LSPR wavelength. A) Compares constant height vs. changing size and snip. B) Compares constant snip vs changes in height and size where particle 8 is included to show that linewidth only changes appreciably when snipping is included. Dimensions (nm) are particle 1: L=100, H=10, and S=11.5; particle 2: L=90, H=10, S=7.5; particle 3: L=80, H=10, S=3.5; particle 4: L=70, H=10, S=0; particle 5: L=95, H=15, S=0; particle 6: L=70, H=10, S=0; particle 7: L=58.5, H=8.25, S=0; particle 8: L=70, H=5, S=12.25.

an appreciably broader LSPR. Since we are comparing results for fixed λ_{max}, the particle tip sharpness is controlled by "snipping" the tips (and readjusting particle size), and the broadest resonances are obtained by unsnipped (perfectly sharp) tips. Physically the coupling of tip sharpness to plasmon width is a manifestation of the well-known lightning rod effect, and it also can be understood in terms of roughness-induced momentum matching of surface-plasmons to the radiation field.

Although the DDA results provide a straightforward mechanism for understanding the width data in tables 1 and 2, we are not able to perform a quantitative assessment of this interpretation due to the lack of measured structural information about the specific particles being considered. We do note, however, that theory and experiment yield good qualitative agreement for the variation in the observed plasmon linewidths. Our calculations show that a variation of ~41% in linewidth is expected for particles with between 0 and 18% of their tips snipped. The experimental data shows ~33% variation. It is expected for theory to show a larger variation in linewidth since it can represent nanoprisms with perfectly sharp tips, while the tips of the chemically synthesized nanoprisms are never perfectly sharp. Also, we cannot rule out the variation of particle dielectric constant with internal structure of the particles (twinned crystal planes, crystal defects, etc) might provide an alternative mechanism for the observed linewidths.

We now turn to the refractive index sensing properties of single silver nanoprisms. Figure 2.9A and B show the LSPR spectra of two different nanoprisms before and after one hour incubations in alkanethiol (Sigma Aldrich) solution. The nanoprism in Figure 2.9A was synthesized with the surfactant BSPP as the capping agent and was incubated in 1-hexadecanethiol. The nanoprism in Figure 2.9B was synthesized with citrate as the capping

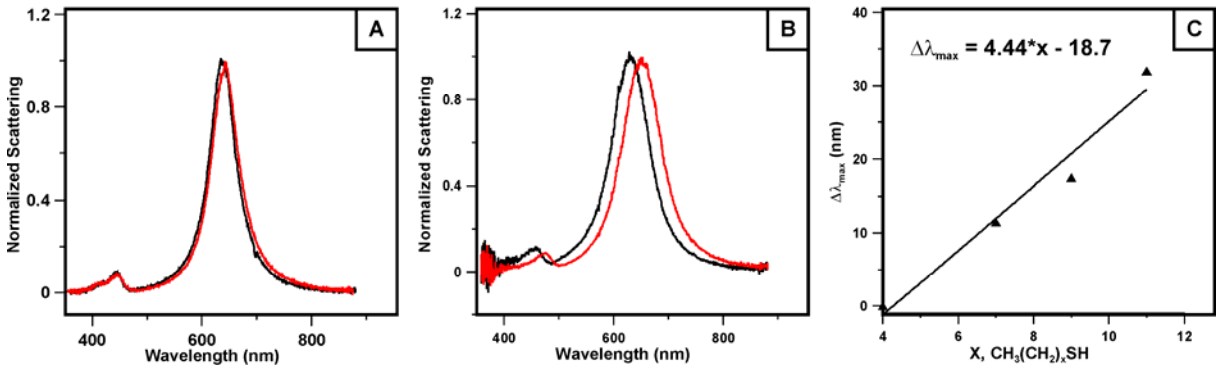

Figure 2.9 LSPR dark-field scattering spectra of single silver nanoprisms before (black) and after (red) surface modification with A) 1-Hexadecanethiol (5 nm dipole shift; BSPP capped) and B) 1-Decanethiol (19.84 nm shift; citrate capped). C) Plot depicting the linear relationship between the LSPR response and the SAM alkyl chain length.

agent and was incubated in 1-decanethiol. These data show that BSPP is not and citrate is displaced by the binding of thiol molecules to the nanoprism surface. This fact is important since the use of BSPP allows for improved control of nanoprism synthesis (higher yield, better size homogeneity, and sharper tips),[59] which is critical for optimizing the sensing properties of single nanoparticles. This can be seen in Figure 2.9C, which shows the relationship between alkanethiol chain length and the maximum observed LSPR shift. By controlling the shape of the nanoparticles, the increment in wavelength per CH_2 group is 1 nm larger in the present measurements (4.44 nm per CH_2 group vs. 3.5 nm per CH_2 group) than with previously studied citrate reduced single nanoparticles (involving randomly selected particles) for the dipole plasmon resonance.[9]

Table 3 lists the LSPR shift data due to adsorption of 1-decanethiol to the surface of the three single nanoprisms shown in Figure 2.7A for both their dipole and quadrupole resonances. The reference shift in table 3 is based on previous experimental work by Van Duyne and coworkers on triangular truncated tetrahedra (120 nm perpendicular bisector and 50 nm height) modified with 1-decanethiol.[56] Note that the nanoprism with the greatest linewidth experiences the largest shift upon chemical modification. If we assume that linewidth correlates with tip sharpness as described above, then we can also understand why this also leads to the largest shift upon chemical modification. This is because earlier theory from Schatz and coworkers has demonstrated that the dielectric shift is largest where the near-field is largest,[115] and the near-field is largest for the sharpest tips. The other two nanoprisms do not obviously follow this argument since nanoprism 3 (narrower linewidth) experiences a greater shift than nanoprism 2.

However other factors can make the shift associated with molecules that coat the entire surface of the particle scale differently than that associated with just the tip regions.[113, 115, 117]

Note that there are no reference shift data for the quadrupole peak since this is, to our knowledge, the first time a quadrupole plasmon resonance has been shown to respond to local refractive index changes. The quadrupole excitation of a nanoprism yields broader plasmon resonances, less sensitivity to bulk and local refractive index changes, and lower FOM values relative to the dipole excitation. The only deviation from these trends was observed for the shift induced by 1-decanethiol bound to the surface of nanoprism one. In this case the quadrupole shift was greater (in energy units) than the dipole shift.

2.4 Conclusions

The plasmonic properties of *single* silver nanoprisms have been studied for the first time, and shown to be superior to comparable ensemble averaged nanoparticle plasmonic sensors. It is evident that geometric parameters, along with plasmon position, play a key role in the sensitivity of the nanoprisms to both bulk (solvent) and local (surface chemical modification) refractive index changes. This agrees with previous statements on the subject, and an approach to more carefully explore this issue is needed. Also, measurement of a nanoparticle's quadrupole plasmon response to changes in the local refractive index has been demonstrated for the first time. This information provides an experimental probe of the LSPR quadrupolar fields surrounding a nanoparticle, and in some cases it provides greater sensitivity to adsorbates than do dipole resonances.

Single nanoprisms show great promise as chemical and biological sensors for three reasons: (1) The single nanoprisms studied are approximately five times thinner than the nanoparticles used in the comparison data set. This implies that the electromagnetic fields of the nanoprisms extend significantly farther from their surface than those of the reference particles since it was shown by Van Duyne and coworkers that thinner particles have larger sensing volumes.[114, 117, 118] Hence, the shifts recorded for the nanoprisms are due to a much lower percentage of the total sensing volume than was the case for the reference particles. Therefore, the nanoprisms should be even better for sensing of large biomolecules since these will fill a greater percentage of a nanoprism's sensing volume (2) Virtually all the nanoprisms in a given sample have some amount of tip snipping (average ~ 10-15 % of the unsnipped edge length). If we restrict our measurements to particles with sharper tips, then larger refractive index sensitivity can be achieved since the most of the triangular nanoparticle's near-field electromagnetic enhancement is localized to the particle's sharp tips.[115] (3) All triangular prism spectra blue shift when first exposed to solvent. This is generally interpreted as further annealing of a prism's sharp tips. If the tips can be protected, nanoprism sensing performance will be improved.

Part I: Chapter 3

Single Nanoparticle Localized Surface Plasmon Resonance Spectroscopy of Single Silver Nanocubes

3.1 Introduction

Much of recent attention concerning metal nanoparticles has been concerned with their use as small volume, ultrasensitive sensors.[9-14] These studies exploit the environmental sensitivity of a nanoparticle's LSPR spectrum by exposing a nanoparticle to solvents of varying refractive index and by modifying a nanoparticle's surface with a self assembled monolayer (SAM) of small-molecule adsorbates. Intrinsic to this type of study is the need to immobilize the nanoparticles on a substrate, particularly if one is interested in working with single nanoparticles. Van Duyne, Schatz and coworkers have investigated the effect of dielectric substrates on the LSPR extinction of metallic nanoparticle arrays.[25] Kreibig and coworkers have compared the effects of dielectric, semiconductor, and metallic substrates on nanoparticle optical properties with a nanoparticle positioned at different heights relative to the substrate surface.[26] A conclusion from both of these investigations is that plasmon resonances are red-shifted (relative to the particles in vacuum) due to interactions with the substrate, with the amount of the red-shift being determined by the dielectric constant of the substrate and by the distance between the particle and substrate. If the particle is in contact with the substrate, then the size of the red-shift depends on the fractional area of the particle which is in contact with the substrate. While these studies are of high quality and correctly predict the influence of the substrate on the resonance spectral location, they are performed on nanoparticles of limited geometrical diversity (i.e. truncated tetrahedrons having a maximum height of 50 nm and small (<10 nm) spheres, respectively).

In this chapter I discuss the influence of a dielectric substrate on the LSPR spectrum of a non-spherical silver nanoparticle, specifically a nanocube, and show how the nanocube's LSPR

spectrum is uniquely altered due to the presence of such a substrate. In contrast to the earlier work, this study involves measurements on single particles (using-dark field microscopy), rather than an ensemble, thereby removing the effect of averaging, and enabling us to observe previously unsuspected details of the effects of substrate interactions. In particular, there are *two* plasmon resonance peaks when a silver cube interacts with a glass substrate, one of which is red-shifted relative to the bulk spectrum (where only a single peak is observed), and the other being blue-shifted and considerably narrower. The blue-shifted resonance was not anticipated based on earlier work, but finite difference time domain (FDTD) electrodynamics calculations confirmed that this is the expected result for this nanoparticle geometry. In addition, the blue-shifted resonance shows promise for applications in plasmonic sensing due to its narrow width.

While most plasmonic sensing studies to date have focused on creating systems that maximize the absolute shift of the plasmon peak due to molecular absorption to nanoparticles,[10-14] recent interest in the creation and utilization of narrow plasmons for sensing applications has increased,[27-29] as optimum sensitivity sometimes occurs because of plasmon narrowing rather than index shifting. To study this issue, we define and evaluate a Figure of Merit (FOM) for sensing, and compare values for a variety of nanoparticle structures.

3.2 Materials and Methods

3.2.1 Materials

Substrates for all experiments were 18 mm diameter No. 1 glass coverslips from Fischer Scientific (Pittsburg, PA). Glassware preparations utilized H_2O_2, H_2SO_4, HCl, HNO_3, and

NH_4OH from Fischer Scientific, and ultrapure H_2O (18.2 MΩ cm^{-1}) from a Millipore academic system (Marlborough, MA). Benzoic acid was purchased from Aldrich (Milwaukee, WI).

3.2.2 Substrate Preparation

No. 1 glass coverslip substrates were prepared by a standard procedure where the coverslips were initially treated with a "piranha etch" (3:1 H_2SO_4:H_2O_2) for 30 minutes to clean the glass surface of impurities. The substrates were then rinsed with copious amounts of ultrapure H_2O until the pH of the substrates' bath stabilized at a value of 7. This was followed by sonicating the substrates for 60 minutes in a 5:1:1 H_2O:H_2O_2:NH_4OH bath in order to render the surface hydrophilic via OH^- termination. The substrates were again rinsed with copious amounts of milliQ purified H_2O, and stored in a pH neutral H_2O environment until use.

3.2.3 Sample Preparation

When ready to use, a substrate was removed from the water storage and a 0.5 μL aliquot of nanoparticle solution was drop-coated onto the surface of a still wet glass coverslip. The substrate was then rotated by hand until the nanoparticle solution is well dispersed into the initial water layer. Substrates were then allowed to dry in either air or N_2 environments.

The prepared samples were then loaded into a custom flow cell so that the nanoparticles could be studied in a controlled environment. Prior to acquiring data the nanocubes were rinsed multiple times with methanol in order to ensure surface equilibrium and geometrical stability.

Suspensions of silver nanocubes were prepared by Xia and coworkers at the University of Washington by the polyol synthetic technique.[61] Only a small change in the reaction conditions dictates whether the final product yields cubes or right bipyramids. In this approach the reaction

mixture is fluxed through a high temperature poly glycol solvent. A critical component of this reaction mixture is the use of the surfactant PVP. This molecule binds preferentially to certain crystal faces of the small silver colloidal precursors. This allows inhomogeneous growth dynamics in orthogonal crystal planes.

3.2.4 Structural Characterization

Scanning electron microscope (SEM) images were acquired using a Hitachi 4500 field emission electron microscope (Hitachi, Japan) operating at an accelerating voltage of 5 kV.

3.2.5 Optical Characterization

All ensemble nanoparticle extinction spectra were obtained by standard UV-visible spectroscopy. In this approach a fiber optically coupled Ocean Optics SD2000 (Ocean Optics, Dunedin, FL) spectrometer was used in standard transmission geometry with unpolarized light.

All single nanoparticle scattering spectra were obtained with either a Nikon *Eclipse* TE300 or Nikon *Eclipse* TE2000-U inverted optical microscope (Nikon, Japan) coupled to a SpectroPro 300i imaging spectrometer and a liquid nitrogen cooled Spec-10:400B CCD detector. These microscopes use tungsten filaments for illumination. This illumination was focused on the sample surface by a Nikon 0.8-0.95 numerical aperture (NA) dark-field condenser. Single nanoparticles scattered this light into the collection optics. For this approach it was critical that the NA of the objective (collection optic) was smaller than the NA of the condenser so that none of the illumination light would be collected. A Nikon variable aperture (NA=0.5-1.3) 100X oil immersion objective was chosen for this purpose. Figure 2.1 shows a schematic of this apparatus, and the approach used to acquire single nanoparticle spectra is the same as described in Chapter 2.

3.2.6 Theoretical Calculations

FDTD results were generated using a previously described method.[119] These results describe the behavior of particles in solution and particles on glass, with structural parameters taken to match the experiments as closely as possible. The silver dielectric function was represented using a Drude model, with parameters chosen to match experiments for wavelengths in the 350-600 nm range.[120] The index of refraction of the glass is taken to be 1.5. The incident wave is launched in a box around the nanoparticle to simulate a plane wave propagating into an infinite half space filled with glass in the total-field scattered-field formulation.[93]

The DDA method was used to compare against the FDTD results.. The number of dipoles used to define each nanocube structure was determined by the number needed in order for the grid length to equal 1 nm.

3.3 Results and Discussion

Figure 3.1 compares Rayleigh scattering results for nanocubes. Figure 3.1A compares a single nanocube in water with extinction results for an ensemble of particles in water, and Figure 3.1B compares a single nanocube experiment in dry nitrogen with a FDTD scattering calculation for a 36 nm edge length nanocube in dry nitrogen. Fig 3.1A shows that the solution spectra of the cubes has a strong dipole plasmon resonance at 444 nm, while the single nanoparticle spectrum has two peaks, one blue-shifted (peak 1) and one red-shifted (peak 2) from the solution spectrum. The red-shifted peak is consistent with what was found in past studies of other nanoparticle structures,[46] but the blue-shifted peak has not been seen previously,[32, 46, 58, 72, 77, 121, 122] and we note that this peak is quite a bit narrower than the red-shifted peak. The solution

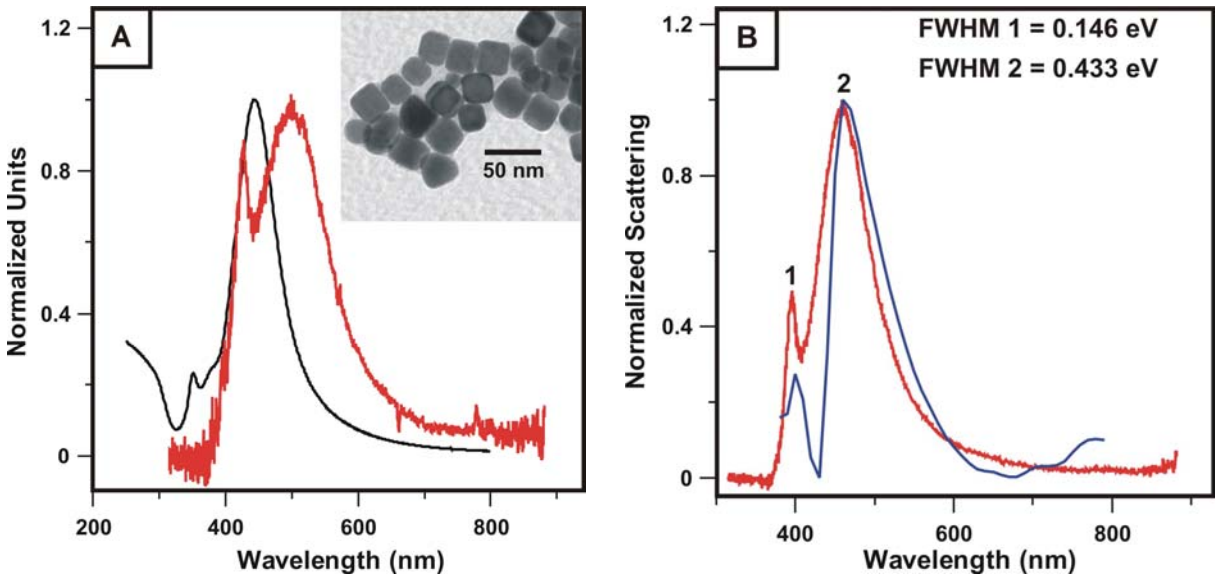

Figure 3.1 Comparison of the LSPR spectra of A) nanocube ensemble extinction (black) and single nanocube dark-field scattering (red) in H_2O environment and B) single nanocube dark-field scattering (red) and FDTD theory (blue) in a nitrogen environment. The calculation in part B was performed on a 36 nm nanocube on a glass substrate.

spectrum also shows a weak second peak at 351 nm. Our theoretical analysis shows, however, that this peak is not derived from the nanocubes. Hence, we assume that it arises from other particles present in small abundance.

Figure 3.1B shows that the calculated and measured scattering spectrum for a single particle on a surface match quite well, thereby confirming that the presence of two plasmon resonances when the particle is on the surface is consistent with electrodynamics for the assumed particle structure. To understand the physical origin of these peaks, we show in Figure 3.2 the near-field behavior associated with the FDTD result for peaks 1 and 2, this time for a larger cube (90 nm), as well as series of scattering spectra that were generated by moving the cube toward the surface. These spectra show that the dipole mode associated with the solution spectrum shifts into a broad peak at 550nm when the particle gets within a few nm of the surface. In addition a blue peak appears at 430nm that becomes more distinct as the particle approaches the surface. Figure 3.2B and 2C show that peak 1 is associated with large fields away from the surface, while peak 2 is associated with large fields toward the surface. This phenomenon shows up clearly with the 90 nm nanocube, and it also occurs for a 30 nm cube but not until it is almost in contact with the glass substrate. DDA calculations for cubes of various sizes do not show the behavior observed in experiments (Figure 3.3A). In water (Figure 3.3B), however, DDA results show plasmon lineshapes with two peaks, as a homogenous dielectric environment also results in multimodal resonances. Plotting the relative shifts of these two peaks for calculations of a nanocube in various solvent environments (Figure 3.3B) shows that peak 1 has a smaller slope than peak 2, indicating that DDA interprets this resonance as a quadrupole. The spatial separation in near-field response seen in Figure 3.2 only occurs for nanoparticles on a substrate.

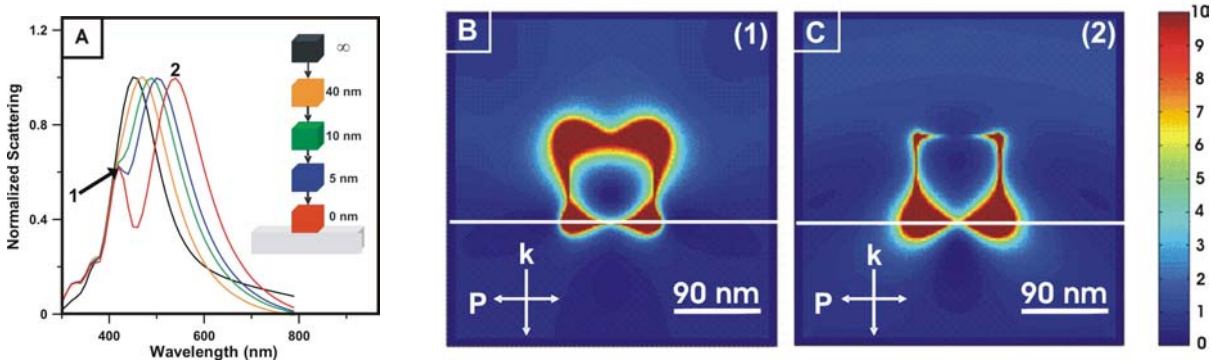

Figure 3.2 FDTD theory showing A) the emergence of a second peak as a single nanocube (90 nm diameter) approaches a dielectric substrate, and B, C) the field intensities for peaks 1 and 2 of the nanocube in contact with the substrate (the white line in the field pattern images represents the substrate).

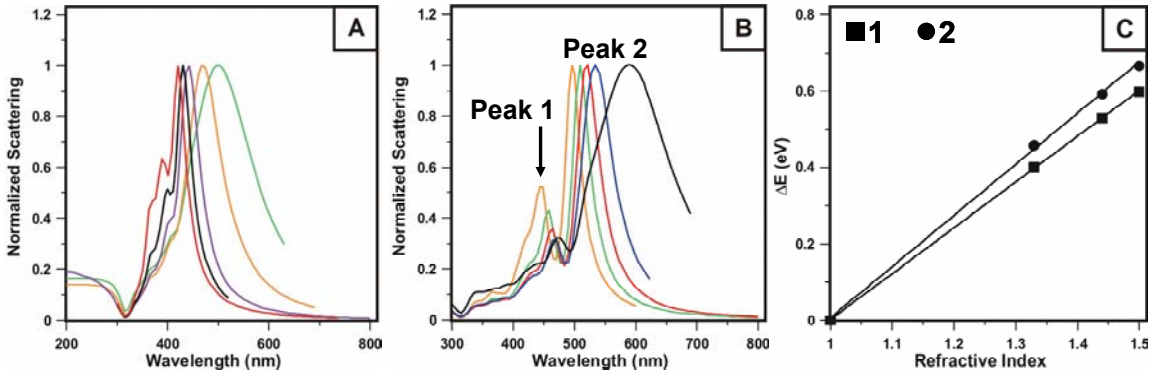

Figure 3.3 DDA calculations for A) 10-90 nm cubes in 20 nm increments in vacuum, B) the same nanocubes as in (A) but in a water environment, and C) the refractive index sensitivity of peaks 1 and 2 for a 40 nm cube.

To further understand these results, we have examined the dependence of the peak wavelengths on the refractive index of solvent above the nanoparticles via dark-field scattering and FDTD theory. Figure 3.4 presents both experimental (Figure 3.4A and B) and theoretical (Figure 3.4B) results, and we see a linear dependence of wavelength on refractive index that is similar to what has been seen earlier in studies of other nanoparticle structures.[32, 58, 72, 115] Linear regression yields experimental slopes of 0.792eV RIU^{-1} (peak 1) and 0.695 eV RIU^{-1} (peak 2; RIU = Refractive Index Unit), which are smaller values than have been seen in studies of triangular nanoparticles.[58] One thing to remember from the triangular nanoparticles is that dipole modes *always* showed a greater RI sensitivity than quadrupole modes. This is an important point to consider since it was possible that a quadrupole mode could have been responsible for peak 1 as indicated by DDA calculations in homogenous dielectric environments.

Intuition tells us that the redder resonance (peak 2) should be less dependent on changes in the bulk dielectric environment than peak 1 since this resonance mostly involves polarization excited at the surface. Indeed, one can see in both theory and experiment that as the refractive index of the dielectric medium increases, peak 1 shifts more readily to higher energy than peak 2. Although both theory and experiment show the same trend (Figure 3.4B) the experimental slope for peak 1 is well below the theoretical value, while theory and experiment have almost exactly the same slopes for peak 2. To explain this we hypothesize that upon exposure to the initial methanol rinsing the nanocubes suffer nonsymmetrical annealing in which the nanocube corners not in contact with the glass substrate are rounded while the corners in contact with the substrate are left virtually unchanged. This causes the nanocube corners not in contact with the glass

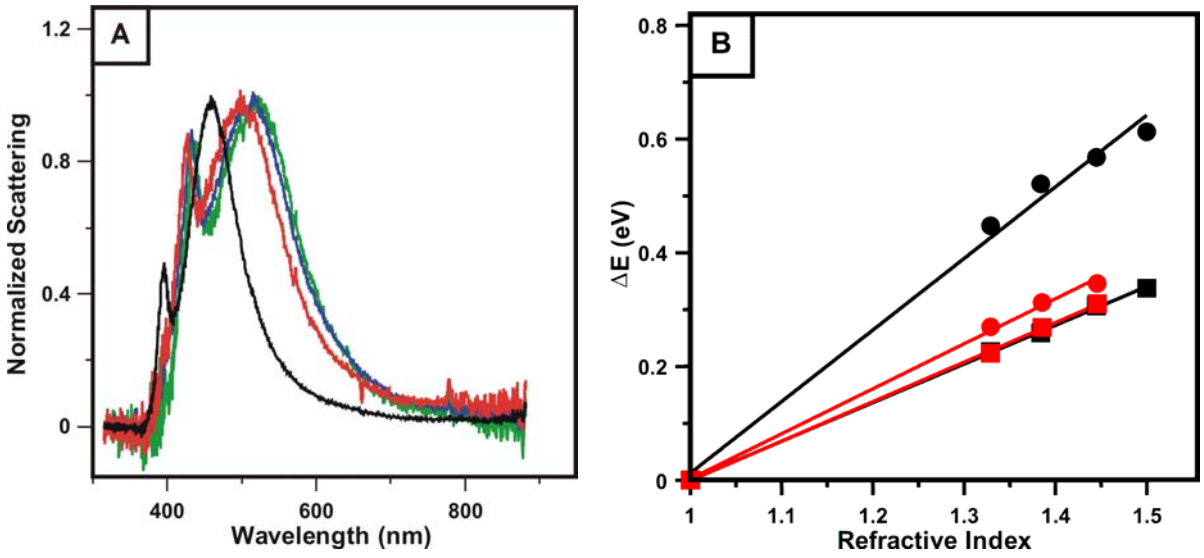

Figure 3.4 Refractive index sensitivities of single silver nanocubes: A) Single nanocube dark-field scattering spectra in four different dielectric environments (refractive indexes = 1.000297, 1.329, 1.3854, 1.4458). B) Theoretical (black) and experimental (red) linear regression fits of the relative energy shift for each nanocube peak (circles = peak one, squares = peak two) in the various dielectric environments.

substrate to have a larger radius of curvature, and based on our earlier work, this means a lessened sensitivity to changes in dielectric environment.[33, 58]

To test this hypothesis we acquired two dark-field LSPR scattering spectra in dry nitrogen: one before methanol rinsing and one after. If the methanol rinsing causes inhomogeneous solvent annealing of the nanocubes, the scattering spectra should reflect this with inhomogeneous blue shifts in the resonance peaks due to overall reduction in the nanocube's size.[33] Indeed Figure 3.5 shows precisely this type of behavior. Peak 1 experiences a 4.17 nm blue shift while peak 2 remains unchanged. To substantiate this result we performed a theoretical study of nanocubes with rounded corners using the FDTD method. The theory shows that if the nanocube's top corners are annealed, peak 1 blue shifts while peak 2 remains unchanged, and if the bottom corners are annealed peak 2 blue shifts. The experimental results, when compared to theory, are consistent with a ~2 nm annealing of the top corners leading to peak 1's observed 4.17 nm blue shift. This theory result also helps confirm that peak 1 is the resonant mode associated with the top corners of the nanocube and peak 2 is the resonant mode associated with the bottom corners.

Our mechanism was also tested experimentally. In order to accomplish this, LSPR spectra were acquired for two nanocubes in nitrogen environments. Index-matching oil was then placed on the sample and a second glass coverslip was placed on top of the oil drop. This created an effectively homogeneous dielectric environment for the nanocubes. Figure 3.6 shows a comparison of the nanocubes' spectra in heterogeneous and homogeneous dielectric environments. While each spectrum still shows a small side peak for each of the nanocubes, it has been damped severely. The persistence of its presence could be due to a weak quadrupole

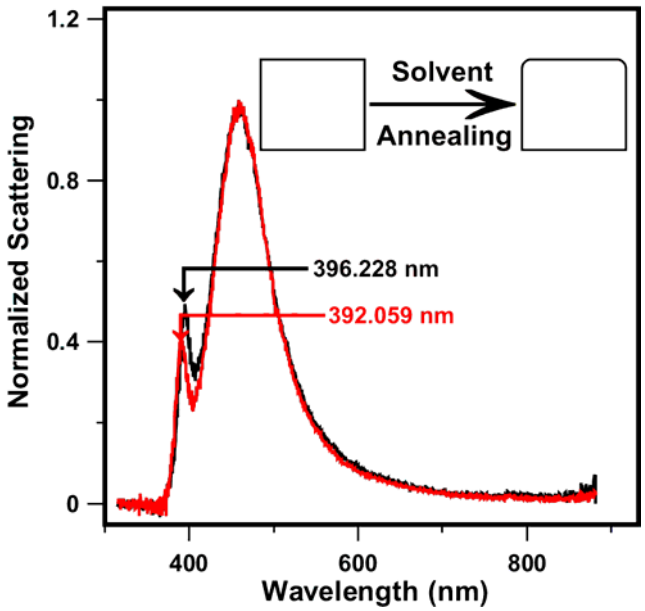

Figure 3.5 Dark-field LSPR scattering spectra for a single nanocube before (black) and after (red) solvent annealing with methanol.

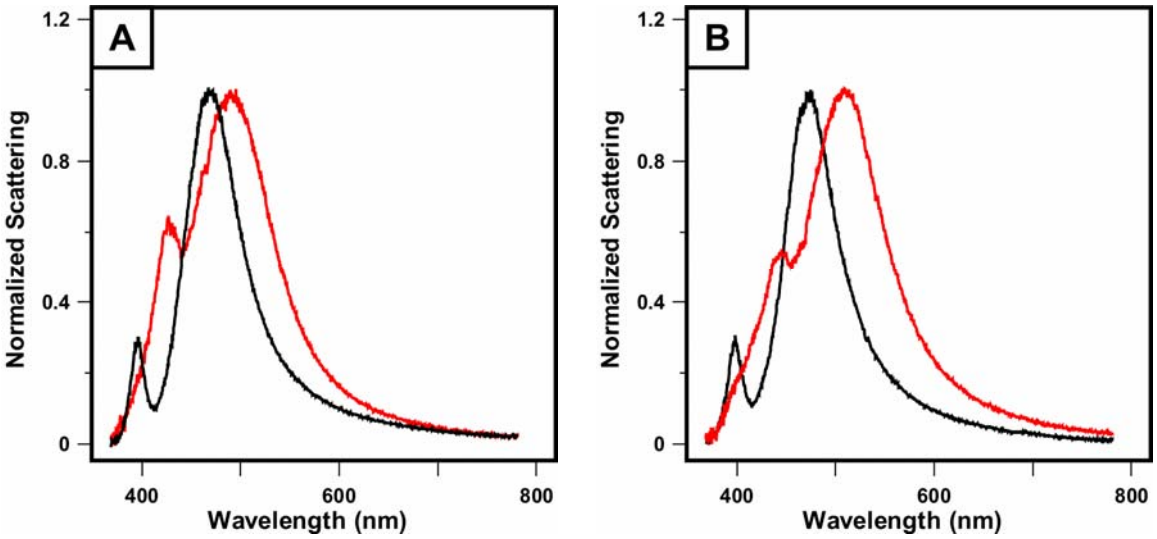

Figure 3.6 Dark-field scattering spectra of nanocubes acquired in heterogeneous (black curves) and homogeneous (red curves) dielectric environments.

resonance or a slight mismatch in the refractive indices of the glass substrate and index-matching oil.

To more thoroughly understand the geometric dependence of this phenomenon we conducted theoretical studies on how shape and size influence a single nanoparticle's LSPR scattering spectrum. To model the substrate effect for particles with different shapes we conducted FDTD calculations for spherical particles at progressively smaller distances above a glass substrate as done in Figure 3.2 for the nanocubes. In these studies we found only one plasmon resonance as the nanoparticle approaches and comes into contact with the substrate. If, however, the nanospheres are partially submerged into the substrate two peaks appear in the lineshape. This result is consistent with the location of hot spots for the different nanoparticle structures.[123] If the near-field intensity is very high both above and below the particle when it is in contact with the substrate, as is shown in Figure 3.2 for a cubic particle, then two peaks can result. For spheres, however, the highest intensities (for polarization parallel to the surface) are near the equatorial regions of the sphere. Hence the plasmon resonance is controlled by the medium above the substrate when the sphere touches the surface. Only when the nanosphere is submerged in the surface is it possible to generate two peaks.

The size, or thickness, of the nanocube also proved to be critical in creating the sharp resonance in Figure 3.1. For nanocubes smaller than the skin depth (~20 nm) the two resonances merge. In this situation the asymmetric dielectric environment is averaged in determining the overall response.

Now we consider the possibility of exploiting the extreme sharpness of peak 1 (FWHM = 0.146 eV) in chemical sensing applications. Although peak 1 proved to be less sensitive to

changes in its dielectric environment than previous studies have shown for other nanoparticle geometries,[58] the overall refractive index sensitivity also depends on the FWHM. Hence, we define a "Figure of Merit" (FOM) in order to directly compare the overall performance of single nanoparticles as chemical sensors:

$$\text{FOM} = \frac{m \text{ (eV RIU}^{-1}\text{)}}{FWHM \text{ (eV)}} \tag{3.1}$$

where m is the linear regression slope for the refractive index dependence. This definition allows nanoparticles to be judged against one another as sensing platforms independent of shape or size**.** Experiments on triangular nanoprisms synthesized via wet chemical techniques[48] have yielded FOMs averaging ~3. For the nanocube measurement in Figure 3.1B, we find a FOM of 1.6 for peak 2 and 5.4 for peak 1, the highest value we have obtained so far in isolated nanoparticle applications.

However, when we attempted to use these nanocubes in molecular sensing experiments we found that they yielded no response. Figure 3.7 shows two nanocubes incubated overnight in 10 mM hexadecanthiol. As can be seen the result was zero shift in both LSPR peaks. This is attributed to the thiol molecules not being able to displace the PVP capping agents used in synthesizing the nanocubes; just as in the case of the BSPP capped nanoprisms in the last chapter. Unfortunately, the cubes, unlike the nanoprisms, cannot be synthesized without the use of the capping agent. Hence, another solution was required in order to employ nanocubes as chemical sensors.

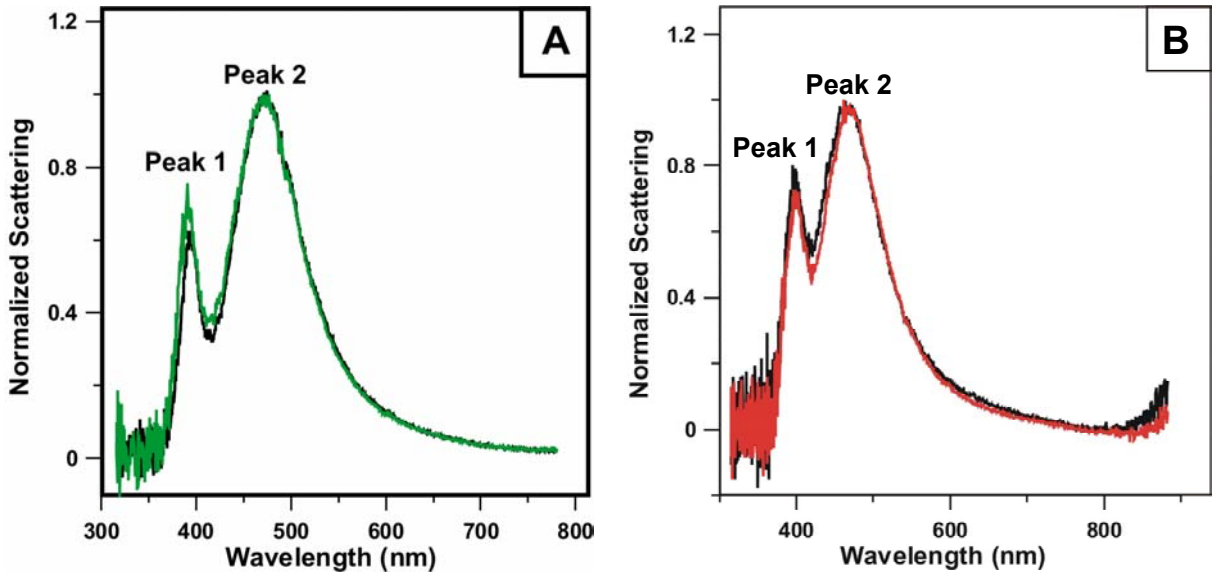

Figure 3.7 Chemical sensing results for two nanocubes incubated in 10 mM hexadecanethiol for 12 hours. Black curves were acquired with the nanocube in a nitrogen environment before exposure to thiol, and colored curves were acquired in a nitrogen environment after exposure to thiol.

The approach to solving this problem needed to be general since most of the nanoparticle geometries holding the greatest promise for chemical sensing applications are synthesized with capping agents. Even the syntheses that do not require the capping agents suffer greatly in terms of geometric homogeneity when the capping agent is omitted. Hence, the requirements were: (1) to modify a nanoparticle surface regardless of its surface functionality, (2) to modify a nanoparticle surface without filling its sensing volume, and (3) to modify a nanoparticle surface without degrading the properties of its LSPR modes. The approach that met all three requirements was atomic layer deposition (ALD).

ALD had been used previously to study the nature of the EM fields outside of silver truncated tetrahedral.[117] This study showed that silver nanoparticles retained their LSPRs when coated with an alumina surface, and that single atomic layers could be deposited over the nanoparticles. Bearing these results in mind, ALD could address one other issue in addition to the three mentioned above. Since we could systematically change its dielectric environment in atomic layer increments, we could further test our hypothesis concerning the physical mechanism behind the two resonance peaks.

Figure 3.8 shows the LSPR spectra and RI sensitivities for peaks 1 and 2 of a nanocube with five atomic layers of alumina deposited on its surface via ALD. Figure 3.9 shows the LSPR spectra and RI sensitivities for peaks 1 and 2 of a nanocube with 11 atomic layers of alumina. The relative ratios of the slopes for peaks 1 and 2 for each nanocube are 1.44 (with 5 layers of alumina) and 1.03 (with 11 layers of alumina). The nanocube with a ~2x thicker alumina shell shows a 28% decrease in the relative RI sensitivities of its two peaks. This result states that as the total sensing volume of a nanocube is made more homogeneous (i.e. filling with alumina

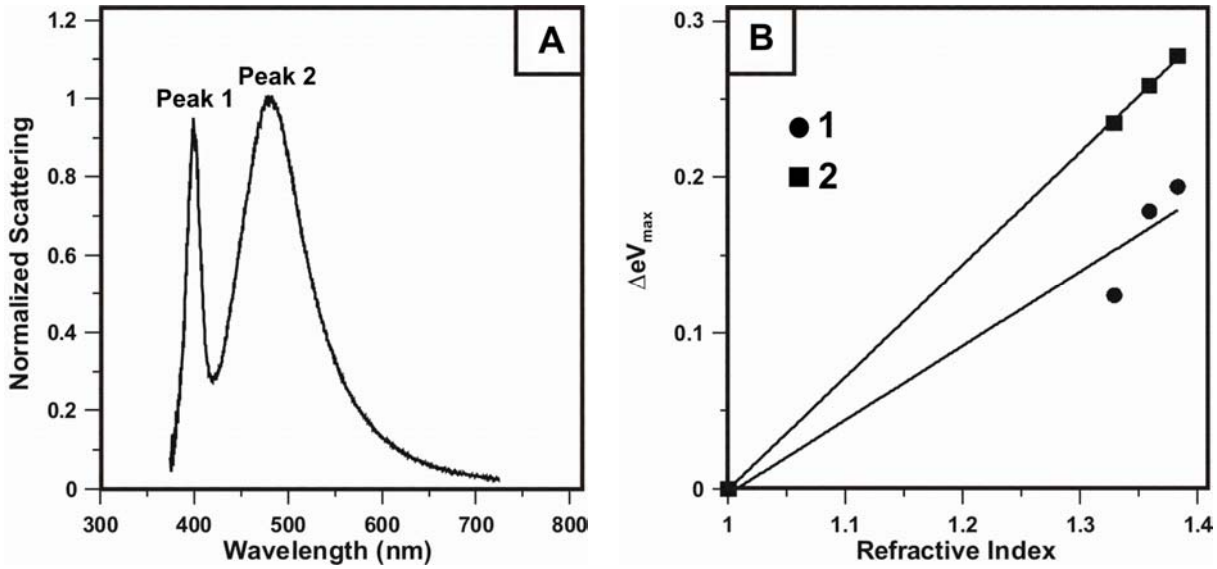

Figure 3.8 A) LSPR spectrum of a single silver nanocube with 5 cycles of alumina (0.5 nm) deposited by ALD. B) Refractive index sensitivities of peaks 1 and 2 respectively (peak 1 RI sensitivity = 0.722 eV*RIU^{-1}, FOM = 4.82; peak 2 RI sensitivity = 0.502 eV*RIU^{-1}, FOM = 1.08).

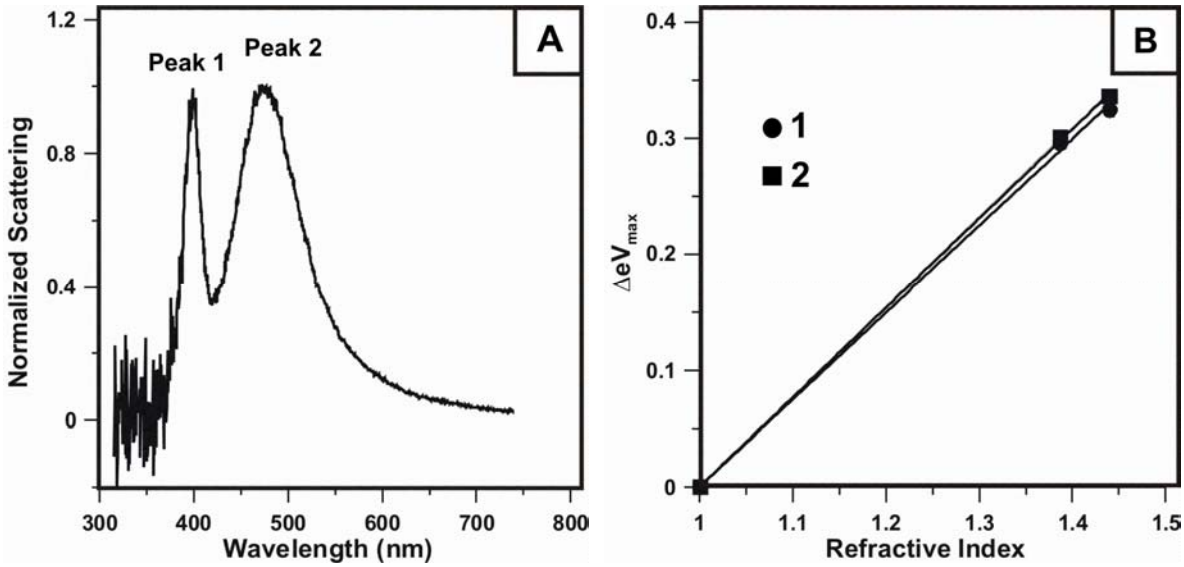

Figure 3.9 A) LSPR spectrum of a single silver nanocube with 11 cycles (1.1 nm) of alumina deposited by ALD. B) Refractive index sensitivities of peaks 1 and 2 respectively (peak 1 RI sensitivity = 0.769 eV*RIU^{-1}, FOM = 4.27; peak 2 RI sensitivity = 0.747 eV*RIU^{-1}, FOM = 1.61).

overlayers) the sensitivities of the peaks become equal. This result supports the FDTD explanation of the LSPR spectra of single silver nanocubes.

Figure 3.10 addresses the question of molecular sensing with ALD overlayers. This figure shows that peak 2 experienced a greater shift than peak 1 for the binding of benzoic acid to the nanocube's alumina surface (11 cycles). Here we finally seem to have a piece of data that argues for a conventional interpretation of silver nanocubes' LSPR spectrum where the intense low energy peak is a dipole and the weaker high energy peak is a quadrupole. Under more careful consideration, however, one can see that this is not correct. Recall that we desired a technique that would coat almost any surface with a protecting layer. The ALD process does exactly this, and the process is done after the nanoparticles are immobilized on the glass coverslip. This means that not only are the nanoparticles coated with alumina, but so is the glass substrate. Since the alumina is not filling the entire sensing volume of the nanocubes, molecules binding to the glass surface within the nanocubes' sensing volume (~25-40 nm) will add to the effect felt by the peak due to the substrate and not to the peak resonant on the top of the nanocube.

3.4 Conclusions

In summary, we report the existence of two plasmon resonances for silver nanocubes interacting with a glass substrate as a new substrate effect in single nanoparticle spectroscopy. This behavior has now been found using FDTD theory and we have observed it experimentally via resonant Raleigh, dark-field optical microscopy. Different dielectric environmental dependencies are observed for each resonance, with theory and experiment again in reasonable

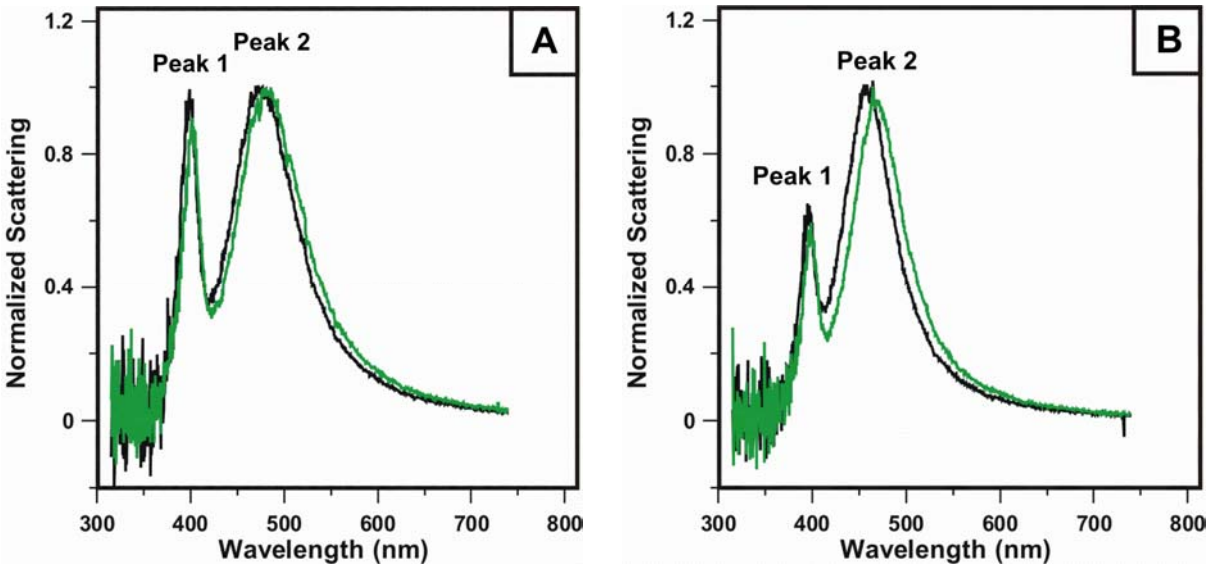

Figure 3.10 Results for binding of benzoic acid to single silver nanocubes coated with 11 cycles (1.1 nm) of alumina via ALD. A) Peak 1 shift = 0.0197 eV and peak 2 shift = 0.0760 eV. B) Peak 1 shift = 0.0134 eV and peak 2 shift = 0.0492 eV.

accord. We found that the two peaks are not obtained for spherical shapes, unless the particles are partially embedded in the surface, or for cubes, unless they are thicker than the skin depth. This shows that the plasmon resonance structure of a nanoparticle in contact with a dielectric substrate is shape and size dependent. Cube-shaped particles are ideal for the production of two resonances as large polarizations are induced on both top and bottom surfaces of the particles, with the bluer of the two resonances having exceptional sensing capabilities due to its extreme sharpness. Current work is underway to explore single nanocubes as chemical sensors. In addition, it may be possible to obtain further experimental observations of the reported substrate effect for a wider range of nanoparticle geometries thanks to recent advances in substrate modification[48] and wet chemical synthetic techniques.[124]

I.2 Outlook

The first part of this thesis has related detailed studies performed on two of the many flavors of nanoparticles available to today's experimentalist. Most of these geometries have unique spectral fingerprints that can identify them without direct structural measurement (exceptions are those that are symmetric in the in-plane dimension and lack sharp tips: i.e. cylindrical disks and spheres). This makes single nanoparticles ideal for multiplexed chemical analysis. In such a scheme each nanoparticle geometry would be synthesized and chemically modified to bind specific target analytes *ex-situ*. The nanoparticles could then be mixed and prepared for optical analysis. The shape of the nanoparticle, identified by its spectral fingerprint, would identify each target analyte being screened. The particle shapes showing shifts would identify which analytes were present. This can be taken one step further to maximize the

sensitivity to each target analyte. This can be accomplished, for example, by targeting large biomolecules with nanoprisms since their fields extend farther than any other nanoparticle due to their thin structure. Conversely, cubes may be best for target analytes with the smallest refractive index change due to its higher FOM.

There are two hurdles to overcome if this type of analysis is to be realized: (1) Speed of data acquisition. The current method for acquiring dark-field LSPR measurements, while adequate for fundamental studies, is unrealistic in a multiplexed paradigm. However, with the incorporation of new tools such as liquid crystal tunable filters it will be possible to perform wide-field single nanoparticle LSPR spectroscopy. In such a configuration it will be possible to measure tens, if not hundreds, of single nanoparticle spectra in a matter of seconds. (2) Nanoparticle synthetic control. While inorganic synthetic chemists continually add new nanoparticle geometries to the experimental landscape, these techniques are not perfect. To date all nanoparticle suspensions contain geometric heterogeneity. This is not limited to variations in the sizes of a particular shape, but in the shapes as well. Any occurrence of a specific nanoparticle suspension containing multiple geometries could lead to errors in sensing experiments. This could be minimized by combining large volumes of the various nanoparticle geometries to be used in a multiplexed experiment, thereby increasing the statistics in one's favor of using properly targeted nanoparticles. Also, approaches such as capillary electrophoresis have been employed for nanoparticle separations,[125] though these techniques require significant refinement before being applicable to the experiment described here.

Part II

Approaches to Correlating Structural and LSPR Measurements

II.1 Introduction

While part one of this thesis demonstrated the utilities and relative advantages of two nanoparticle geometries as refractive index sensors, it did not definitively account for the variations in sensitivities found within one nanoparticle geometry, or even definitively prove that the spectra shown were due to the specific geometries claimed. This is where structural measurements will reveal new insights into the details governing a nanoparticle's environmental sensitivity and further define nanoparticle sensor design parameters if structural measurements can be integrated and/or correlated with optical measurements. Part II of this thesis will address this challenge by incorporating two powerful approaches: atomic force microscopy (AFM) and transmission electron microscopy (TEM).

AFM belongs to the broader class of microscopy known as scanning probe microscopy. This class includes any microscopy in which a physical probe is used to image a sample by raster scanning the probe over a sample and monitoring the probe sample interaction. Two other types of microscopies in this class are scanning tunneling microscopy (STM) and near-field scanning optical microscopy (NSOM). In AFM the physical deflection of a probe by a sample is measured. STM monitors the current between a conducting tip and a conducting substrate. NSOM uses a sub-wavelength optical fiber to probe samples by detecting perturbations in the electromagnetic field produced by the fiber. The power of scanning probe microscopies lies in their ability to resolve features smaller than the diffraction limit. The diffraction limit is a fundamental limit of nature stating that light of a wavelength, λ, cannot resolve anything smaller than $\sim\lambda/2$. If one recalls the size of the nanoparticles studied in part I of this thesis relative to the wavelength of their LSPRs, one can see that light waves cannot resolve the structural features of

these individual nanoparticles. This is why every nanoparticle in Figure 1.2 appears as a circle of light. This is the so-called diffraction limited spot, and appears so due to the wavelike nature of light.

The resolution of scanning probe instruments, unlike light based instruments, is limited only by the size of their probes. STM tips epitomize this by, in principle, being only one atom in size. It is possible to have only one atom in an STM tip responsible for the feedback since the current measured is actually a tunneling current between the tip and sample: i.e. the tip and sample are never in physical contact. This is a quantum mechanical process and decays in strength exponentially as one moves farther up the tip away from the sample. While STM is the ultimate in resolution, with true atomic resolution readily achieved with today's instruments, it is limited to conducting surfaces. AFM, however, is not limited so and will be discussed in detail in chapter 4.

Another class of techniques for imaging beyond the diffraction limit of light is electron microscopy. In this type of approach samples are interrogated by a beam of electrons emitted from a cathode and focused by magnetic lenses. There are two basic types of electron microscopes: the scanning electron microscope (SEM) and transmission electron microscope (TEM). In SEM images are created by detecting secondary electrons emitted from the surface due to excitation by the primary electron beam. In TEM images are created by interrogating the original electron beam after it has passed *through* the sample. This is possible since electrons from the original electron beam are scattered by electrons inside the sample. Herein lies a new way in which to probe samples. Every other microscopy technique described in this section is limited to interrogating a sample's surface. TEM, however, allows one to probe the internal

structure of one's samples. Chapter 5 will discuss the importance these measurements have in understanding the properties of nanoparticle LSPR modes.

Part II: Chapter 4

Combining Microscopy's: *In-Situ* Atomic Force Microscopy with Real-Time Feedback via Resonant Rayleigh Dark-Field Microscopy

4.1 Introduction

The AFM, invented by Calvin Quate (Stanford) in 1986, is one of the most important tools in science today. Although the basic idea of the AFM is quite simply, the realization of the technique was a monumental achievement. From its humble beginnings of simple topological measurements of surfaces, it has expanded into such diverse fields as lithography[126] and single molecule force dynamics[127, 128] as a stand-alone instrument.

In AFM, a probe (generally a pyramidal silicon nitride tip mounted on a supporting cantilever) is pushed along a surface, and all the perturbations experienced by the tip are processed into a topographical map of the surface. This was such an achievement due to the extremely small forces involved in such processes (nanonewton-piconewton). The entire process is made possible by extremely accurate measurements of the cantilever's angle of deflection and a precise feedback control mechanism. Measuring the cantilever's angle of deflection is achieved by monitoring the position of a laser reflecting off the back of the cantilever by a photodiode. Whenever this photodiode registers a deflection of the cantilever the piezoelectric controlled feedback mechanism in the tip housing adjusts the height of the tip above the sample such that the cantilever remains at a constant deflection angle. There are two ways in which a tip scans the sample surface: (1) scanning the sample and (2) scanning the tip. Sample, or stage, scanning instruments are the standard design for AFMs since rendering a topological image in this geometry is straightforward. In this design the x-y in-plane measurements are completely decoupled from the out-of-plane z measurements. Piezoelements in the stage scan the sample and yield the x-y lateral dimensions for the image, and piezoelements in the tip housing account for height (z) dimension for the image. In a tip scanning instrument, however, this must all be

done by piezoelements in the tip housing. In these instruments, the tip housing is physically coupled with the scanning piezoelements to make one unit. Hence, one set of piezoelements must actuate scan motion in all three dimensions. This "scanner" acts as a pendulum as it scans the tip back and forth across a sample. While this approach makes image processing more challenging, it is the only way that the AFM can transition from a stand alone instrument to a versatile component of more complex systems.

The AFM has found widespread utility in being integrated into optical surface science investigations such as tip-enhanced Raman spectroscopy (TERS), where a metal coated AFM tip serves as the electromagnetic field-enhancing substrate.[129, 130] In this type of experiment, however, the AFM's primary function of surface characterization is not utilized. Hence, a far more widespread application of coupling AFM to optical surface science has been in fluorescence studies of biological processes. These studies are generally interested in processes occurring in thin membranes, such as a cell membrane. When conventional fluorescence microscopy is applied to such studies, fluorescence from other parts of the cell often interferes with the fluorescence information in the region of interest. To overcome this issue a number of imaging approaches have been employed including confocal microscopy[131] and surface plasmon resonance microscopy (SPRM).[132] SPRM localizes the illumination to within a few microns, and confocal microscopy to within 500 nm. However, the thickness of a lipid bilayer plasma membrane is only 6-10 nm. So experimentalists needed an even better approach to spatially localizing electromagnetic fields. This was achieved by the use of total internal reflection (TIR). In this approach a spatially confined (to within a couple hundred nanometers) electromagnetic

wave is created at an interface of two dielectric media via TIR, and will be discussed in detail in section 4.3.

The AFM has also found been widely applied to applications in characterizing inorganic nanoscale materials; specifically metallic nanoparticles. With the discovery of shape dependent properties of nanoparticles it has become increasingly imperative to properly characterize the structural characteristics leading to these properties. This has been straight forward for studies of array structures, but is more challenging for single nanoparticle applications. To date there has been no *in-situ* studies correlating multiple properties of single nanoparticles. These studies are critical if we are to understand the results of applied single nanoparticle experiments.[75, 133] This chapter discusses an approach to remedy this deficiency and presents preliminary results thereof.

4.2 Materials and Methods

4.2.1 Materials

Substrates for all experiments were either 18 or 25 mm diameter No. 1 glass coverslips from Fischer Scientific (Pittsburg, PA). Glassware preparations utilized H_2O_2, H_2SO_4, HCl, HNO_3, and NH_4OH from Fischer Scientific, and ultrapure H_2O (18.2 MΩ cm^{-1}) from a Millipore academic system (Marlborough, MA). Sodium borohydride (99%), trisodium citrate dihydrate, silver nitrate (99.9999%), and poly-L-lysine (98%) were purchased from Aldrich (Milwaukee, WI). Bis(p-sulfanatophenyl) phenylphosphine dihydrate dipotassium salt (BSPP) was purchased from Strem Chemicals (Newburyport, MA).

4.2.2 Substrate Preparation

No. 1 glass coverslip substrates were prepared by a standard procedure where the coverslips were initially treated with a "piranha etch" (3:1 H_2SO_4:H_2O_2) for 30 minutes to clean the glass surface of impurities. The substrates were then rinsed with copious amounts of ultrapure H_2O until the pH of the substrates' bath stabilized at a value of 7. This was followed by sonicating the substrates for 60 minutes in a 5:1:1 H_2O:H_2O_2:NH_4OH bath in order to render the surface hydrophilic via OH^- termination. The substrates were again rinsed with copious amounts of milliQ purified H_2O, and stored in a pH neutral H_2O environment until use.

4.2.3 Sample Preparation

When ready to use, a substrate was removed from the water storage and a 5-25 μL aliquot of nanoparticle solution was drop-coated onto the surface of a still wet glass coverslip. The substrate was then rotated by hand until the nanoparticle solution is well dispersed into the initial water layer. Substrates were then allowed to dry in either air or N_2 environments.

Colloidal suspensions of silver nanoparticles were synthesized by reducing silver nitrate with sodium citrate by an established scheme pioneered by Lee and Miesel.[134] In this approach 90 mg of silver nitrate and 500 mL of ultrapure water are combined and brought to a boil in a 1 liter cleaned flask (3 HCl:1 HNO_3). Then 10 mL of a 1% sodium citrate solution was added while stirring vigorously. This solution was boiled for 30 minutes. During this time the solution undergoes a color change sequence: first to light yellow followed by a change to an opaque brown. After the 30 minutes, the new suspension was allowed to cool and transferred to a brown glass bottle for storage. Most of the nanoparticles in such a suspension are spherical in shape

with a diameter ~ 40 nm. However, many other geometries are also present such as: triangular prisms, rods, cubes, hexagonal plates, and many others.

Suspensions of triangular nanoprisms were synthesized by an established technique pioneered by Jin *et al*.[59] This is a two step synthesis where a seed solution of silver colloids (~8 nm) serve as the starting material for triangular nanoprism formation. First, nanopure water (95 mL), aqueous trisodium citrate (1 mL of 30 mM, freshly prepared), and aqueous silver nitrate (2mL of 5 mM, freshly prepared) were mixed in a 250 mL 3 necked flask that had been cleaned with aqua regia for at least 3 hours. This solution was immersed in an ice bath and stirred for 30 minutes. During this time inert gas (Ar or N_2) was bubbled through the solution. After 30 minutes the inert gas flow was terminated, and each neck of the flask was corked with a rubber stopper. Aqueous sodium borohydride (50 mM) was then made using ice-cold ultrapure water. 1 mL of this solution was quickly injected into the ice-cold solution by a syringe through the center rubber stopper. The clear solution turned pale yellow immediately (note: if a blue color that fades to light yellow appears initially, the seed solution is unusable). The reaction was allowed to proceed for an additional 15 minutes. 1 mL of BSPP and 0.5 mL of sodium borohydride solutions (50 mM, freshly made with ice-cold water) were then added dropwise over a five minute period. The resulting suspension of small silver colloids were immediately divided into 10 mL vials and irradiated with a fluorescent lab lamp overnight. After the irradiation period the suspension changed from yellow to deep green or blue, indicating the formation of triangular nanoprisms.

4.2.4 Structural Characterization

AFM images were acquired using a Molecular Imaging PicoPlus AFM (Agilent Technologies, Santa Clara, CA) operating in either tapping or contact mode. Pyramidal doped single crystal silicon cantilevers (Applied Nanostructures, Santa Clara, CA; tapping mode: radius of curvature < 10 nm, resonant frequency = 200-400 kHz, force constant = 25-75 N/m; contact mode: radius of curvature < 10 nm, force constant = 0.5-5N/m) were used to obtain all AFM images.

Scanning electron microscope (SEM) images were acquired using a Hitachi 4500 field emission electron microscope (Hitachi, Japan) operating at an accelerating voltage of 5 kV.

4.2.5 Optical Characterization

All optical measurements were acquired with a Nikon *Eclipse* TE-2000-U (Nikon, Japan). Three types of dark-field microscopies were used in the following experiments: transmission dark-field, reflected dark-field, and total internal reflection (TIR) dark-field. Transmission dark-field was applied in the same manner as discussed in part I of this thesis. TIR and reflected dark-fields will be discussed in depth in section 4.3. Reflected dark-field measurements were acquired using a Nikon LU Plan ELWD 50x dark-field objective with a N.A. of 0.55 (Nikon, Japan). TIR dark-field measurements were acquired using either the objective used for transmission dark-field measurements or a Nikon Plan Apo 60x TIRF objective with a N.A. of 1.45.

4.3 Results and Discussion

4.3.1 Reflected Dark-Field

Part I of this thesis demonstrated the unique nature of every single nanoparticles' optical spectra, and the need to interrogate the geometries of these structures *in-situ*. I remind the reader of the standard geometry used for dark-field imaging of single nanoparticles as seen in Figure 2.1. If a scanning probe instrument is to be integrated into such an experiment it is obvious that the illumination geometry must be redesigned. Figure 4.1 shows a schematic of the first approach we implemented to address this issue. This approach is referred to as reflected dark-field. In this approach the dark-field condenser and objective are combined into one unit (dark-field objective), leaving the top of the apparatus clear for AFM integration. The condenser is a torus built around the objective. Hence, a custom reflector was built that would reflect only a hollow light cone into the condenser without sending any light into the objective optics. Dark-field is achieved in exactly the same way as in transmission dark-field. The condenser brings the light to the sample at an oblique angle such that reflections from the substrate surface are not collected by the objective lens.

Figure 4.2 shows a reflected dark-field LSPR image of colloidal nanoparticles on a glass surface. One can see that the imaging works beautifully. However, when the AFM tip is brought into contact with substrate, and we once again look at a dark-field image of the nanoparticles we see a glaring problem; the AFM tip's cantilever scatters the illumination light so strongly that the nanoparticles' scattering is lost (Figure 4.3). This result shows that the reflected dark-field approach does not address the need for which it was designed. In order to gain correlated information about single nanoparticles one would have to resort to image pattern

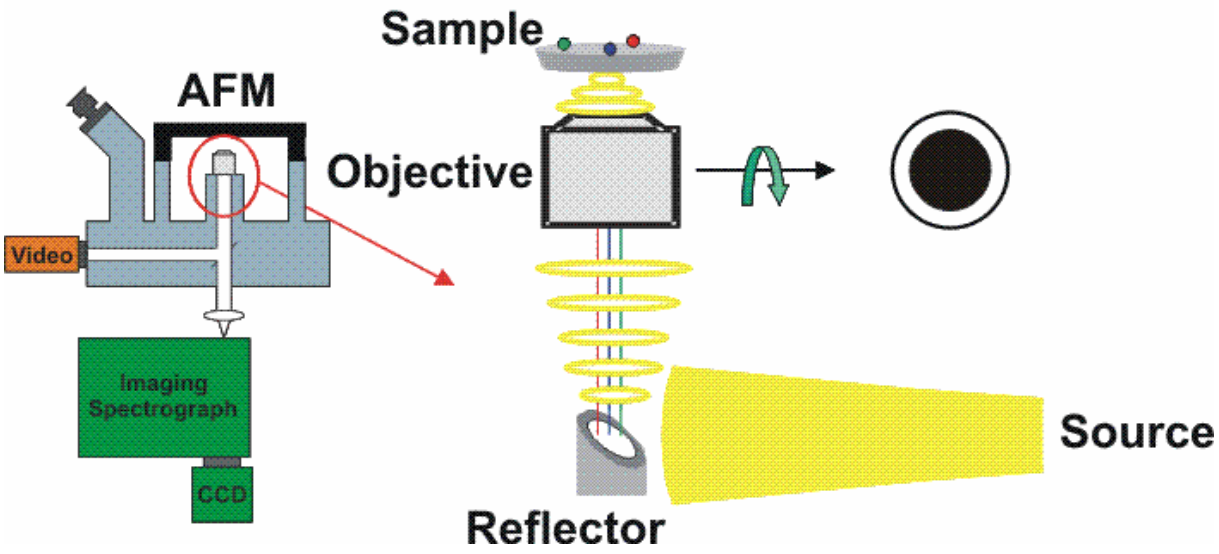

Figure 4.1 Schematic of the experimental apparatus used for integrating an atomic force microscope into a reflected dark-field microscopy geometry.

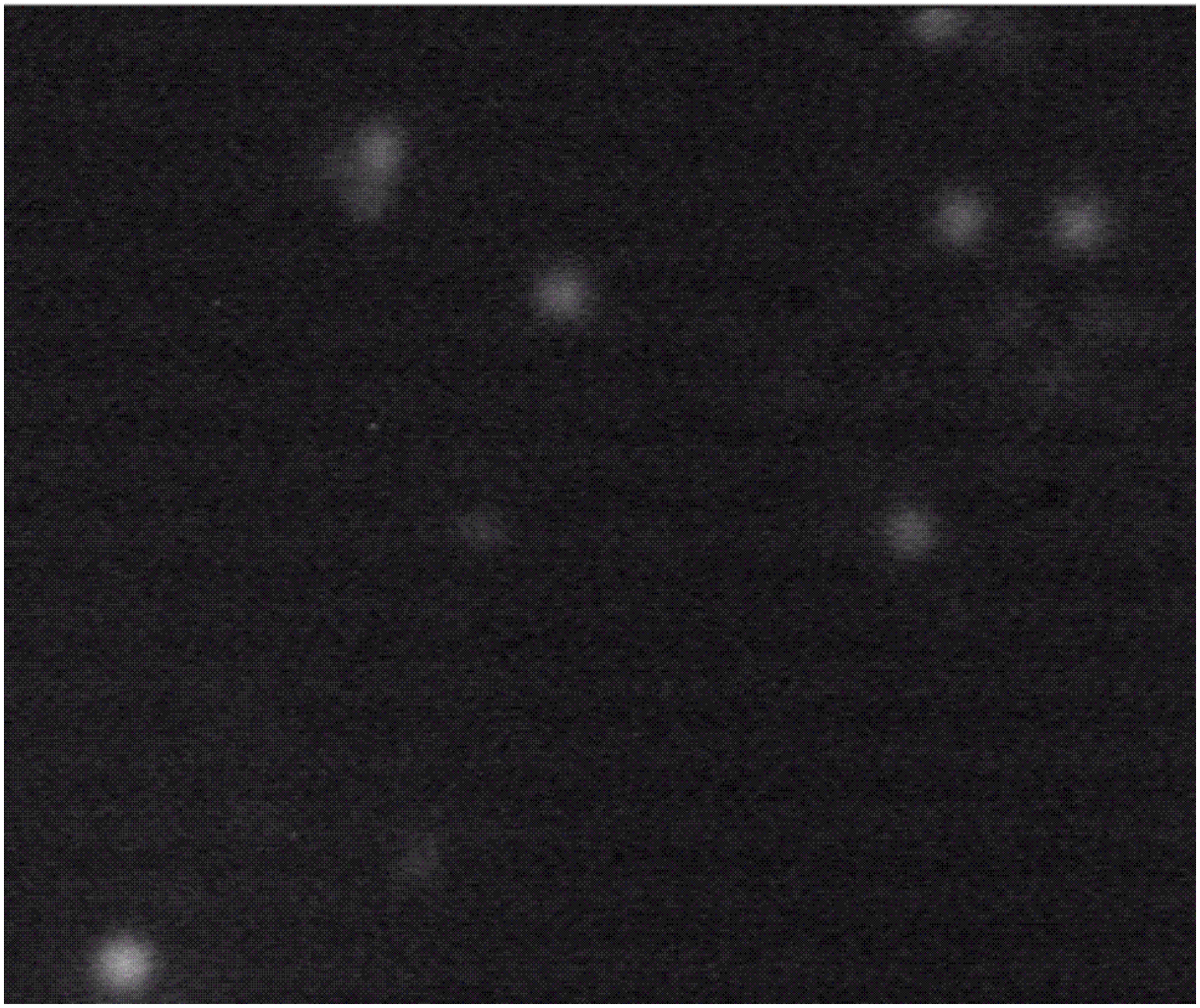

Figure 4.2 Reflected dark-field LSPR image of silver colloidal nanoparticles on a no. 1 glass coverslip

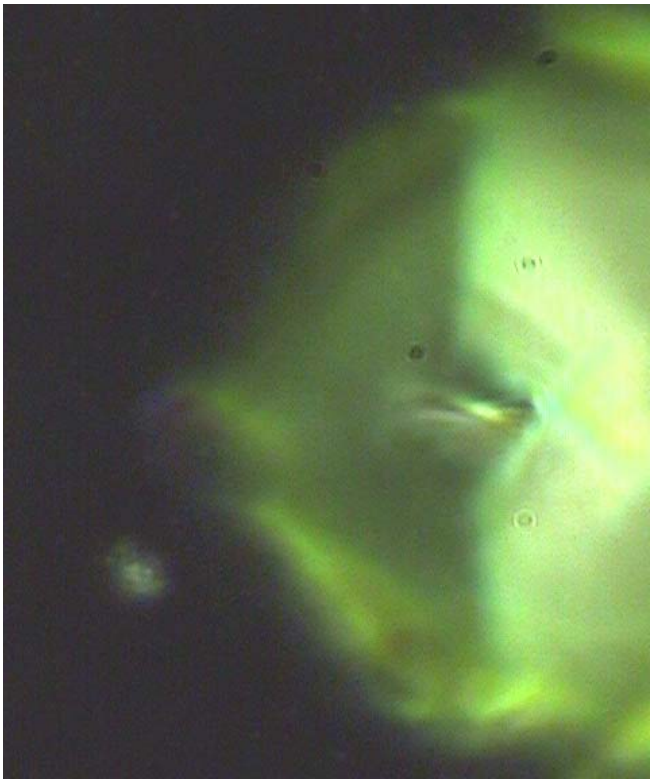

Figure 4.3 Image of an AFM tip engaged on a glass substrate acquired using reflected dark-field microscopy at 50x magnification.

matching techniques. This approach is useful and has been applied in past experiments.[135] However, it did not yield the level of control we sought for this application. This approach does yield one advantage over transmission dark-field: If one wishes to perform dark-field scattering measurements of periodic structures, one must always take care not to mistake diffraction peaks from the array for plasmon peaks. Since the incident light is not passing through the sample towards the collection optics in reflected dark-field this complication is removed.

4.3.2 Total Internal Reflection Dark-Field

A third approach for performing dark-field imaging is total internal reflection (TIR). TIR is an optical phenomenon that occurs at the interface of two different dielectrics. When a beam of light traveling through a material with a high refractive index, n_2, encounters a medium with a lower refractive index, n_1, light is both transmitted and reflected as shown in Figure 4.4. The amount of light undergoing each process depends on the angle of incidence and can be evaluated using the Fresnel coefficients. The angle of the refracted light can be calculated from Snell's law:

$$n_2 \sin(\theta_t) = n_1 \sin(\theta_t) \tag{4.1}$$

As one can see from Snell's law, at a certain incidence angle (θ_i) the "transmitted" beam in fact does not escape the higher index material (n_2). This is known as the critical angle (θ_c), above which all incident light is said to suffer total internal reflection. While no light escapes into the far field from n_2, an electromagnetic wave, which decays exponentially into n_1, does exist at the dielectric interface propagating parallel to it (note that this is a completely classical result since it can be derived from classical electrodynamics, and there is no net energy transmitted to the lower index medium, allowing energy conservation to remain intact). The evanescent wave's

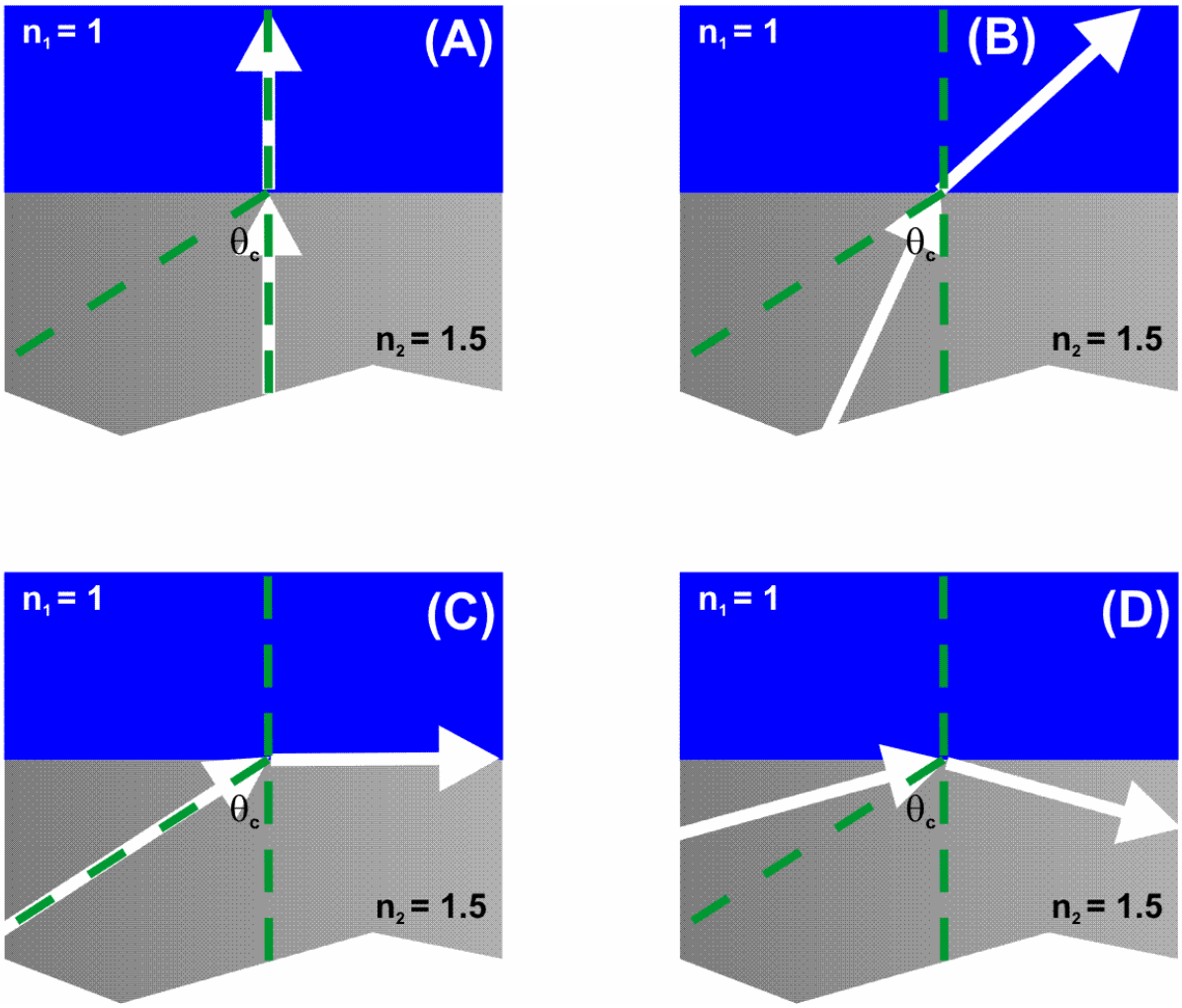

Figure 4.4 Ray optics representation of the behavior of light at the interface of two dielectric materials (air and glass).

penetration into n_1 is wavelength dependent. More specifically, the smaller the wave's energy the further it penetrates into n_1.

There are three tools (shown schematically in Figure 4.5) that can be used to achieve TIR: (A) a glass prism, (B) a coupled waveguide, and (C) a high NA microscope objective. Prism TIR has been employed to study the LSPR of single nanoparticles.[121] This approach, however, leaves no room for the incorporation of an AFM. The coupled waveguide approach does leave room in the system for an AFM. Commercial AFM designs, however, make integrating this scheme into the overall system design extremely difficult. The high NA objective approach is an elegant approach for this application since there are no other elements to include in the system but the commercial microscope and AFM systems. In order to achieve TIR with a microscope objective an oil immersion objective must be used. If an air objective is used the light beam traverses two dielectric interfaces and a sufficiently high NA objective is not available to achieve TIR. The light beam is focused off-axis at the objective's back focal plane as shown in Figure 4.5C. Since the beam is not centered on the objective's optics, the objective lens will turn the beam rather than focus it. It turns out that in order to achieve TIR with an objective lens the NA of the objective must be $\geq$ the refractive index of the lower index material (n_1). TIR is most easily accomplished with a coherent single wavelength light source because the angle at which a light wave is refracted is wavelength dependent. For collecting LSPR spectra, however, a white light source is preferable so as to collect the entire LSPR spectra at one time instead of scanning a laser across many wavelengths. In order to achieve through-the-objective TIR with a white light source it is imperative to have an extremely well collimated light beam. For this purpose we used a fiber optically coupled DH-2000 UV-Vis NIR light

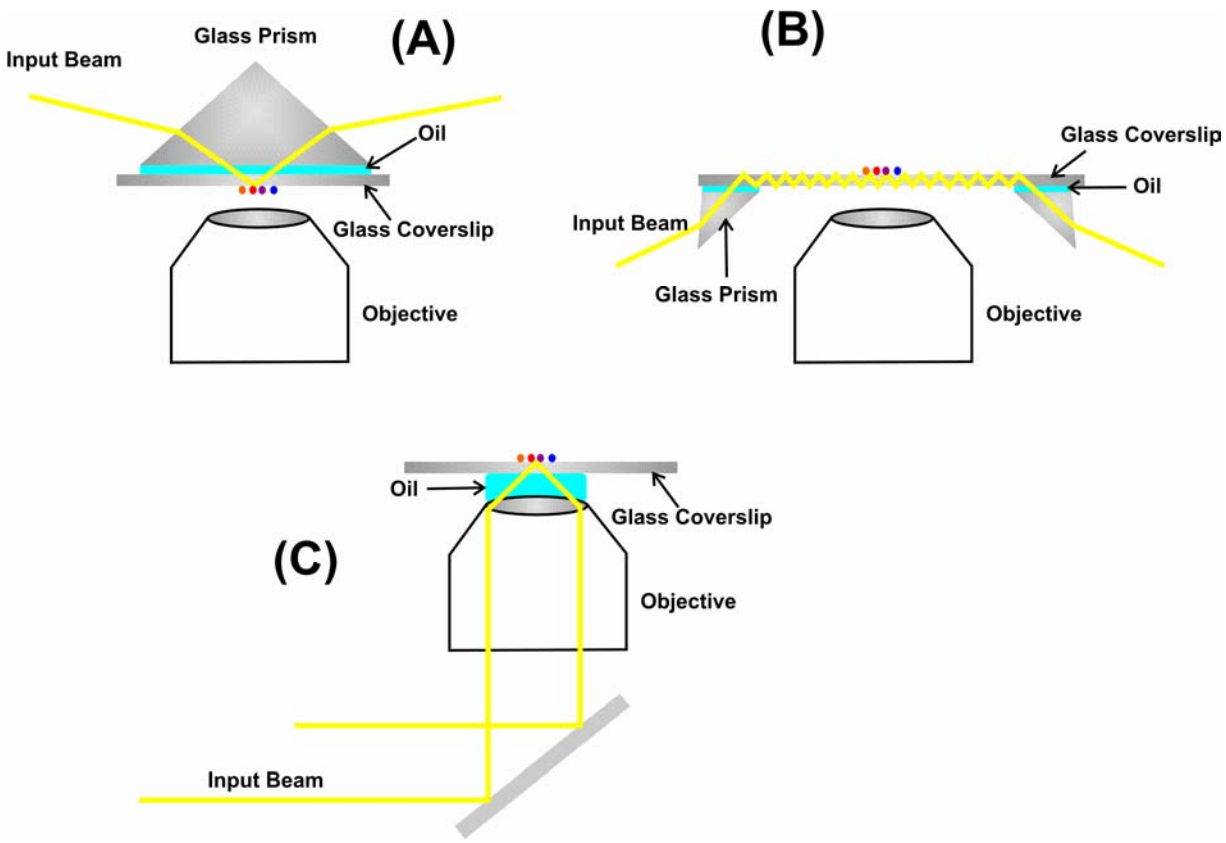

Figure 4.5 Three approaches to TIR dark-field microscopy: A) Glass prism, B) coupled waveguide, and C) through the objective.

source (Ocean Optics, Dunedin, FL). Figure 4.6 shows a schematic of the integrated TIR-AFM system.

Before we could test the performance of the integrated atomic force and dark-field microscopies it was imperative to test whether or not the physics of the LSPR was the same in TIR as it was in transmission. To accomplish this we acquired spectra of the same single nanoparticles in both imaging modalities. Figure 4.7 compares the two LSPR for two particles. Only two particles are shown because these data suffice to explain the overall trends. It was found that nanoparticle's with dipole LSPR peaks above 600 nm yielded almost perfect agreement (Figure 4.7B), while those with dipole LSPR peaks below 600 nm yielded slightly different spectra (Figure 4.7A). There are four factors that could explain these results. First, it is not a straightforward process to determine what the actual spectrum of the excitation light is at the sample surface. This is critical since this spectrum is used to normalize the raw LSPR spectrum. Any error in the normalization spectrum leads to an incorrect nanoparticle LSPR spectrum. A number of different approaches to acquiring the normalization spectrum were attempted. Each one yielded a spectrum very similar to each other and the lamp spectrum. Hence, we feel confident that the spectral lineshape is not the issue. Second, Figure 4.8 shows the spectrum of the TIR light source vs. the transmission dark-field light source. It is clear that the TIR source generates markedly less light below 500 nm. This could lead to errors when normalizing the LSPR spectrum with low signal to noise data. Third, one must consider the geometry of the different nanoparticles interrogated. In Figure 4.7B we are measuring the LSPR of a triangular nanoprism. From chapter 2 of this thesis we know that these nanoparticles are extremely thin (~10 nm). It is more difficult to assign a specific structure to the nanoparticle

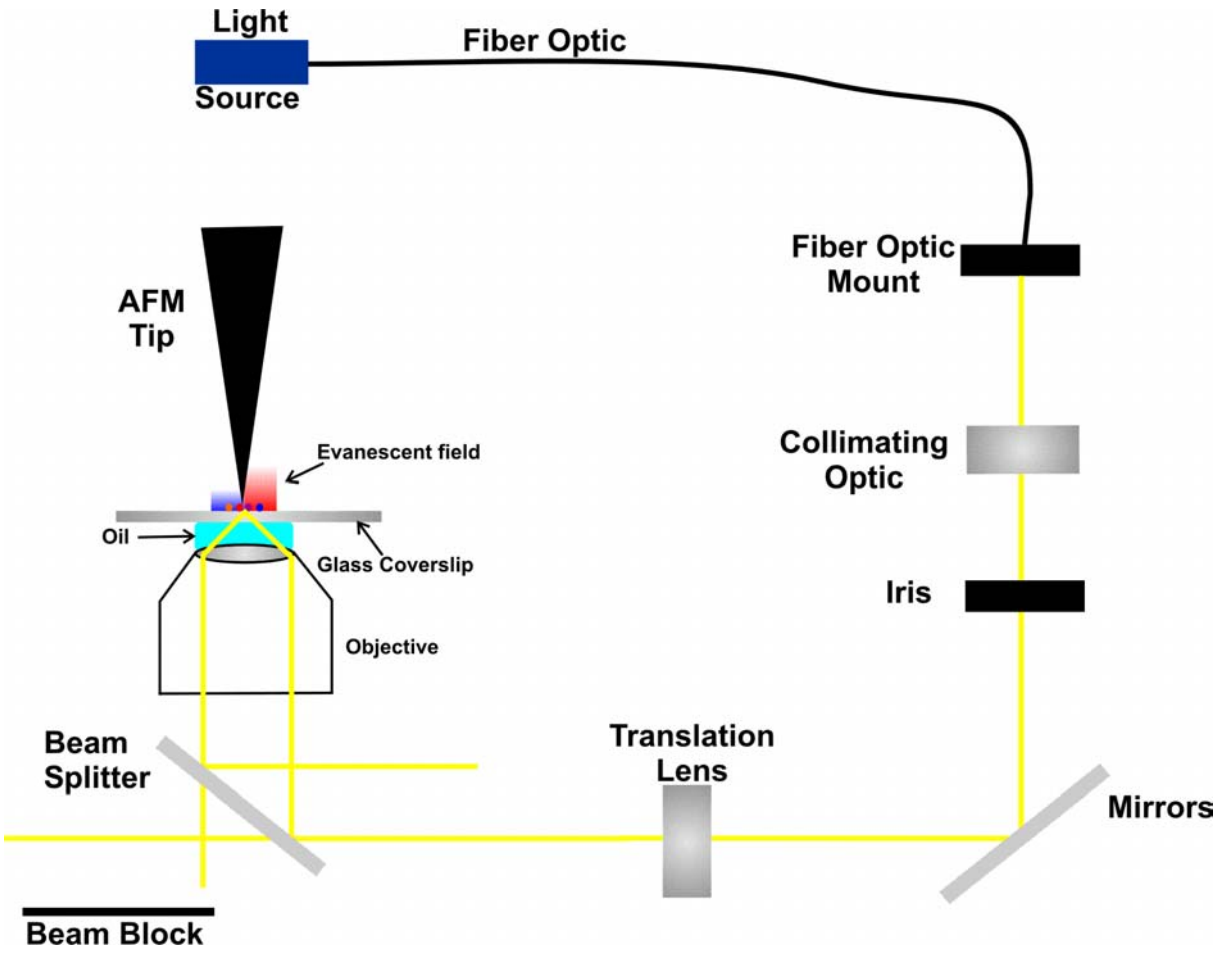

Figure 4.6 Schematic of the integrated TIR-AFM apparatus.

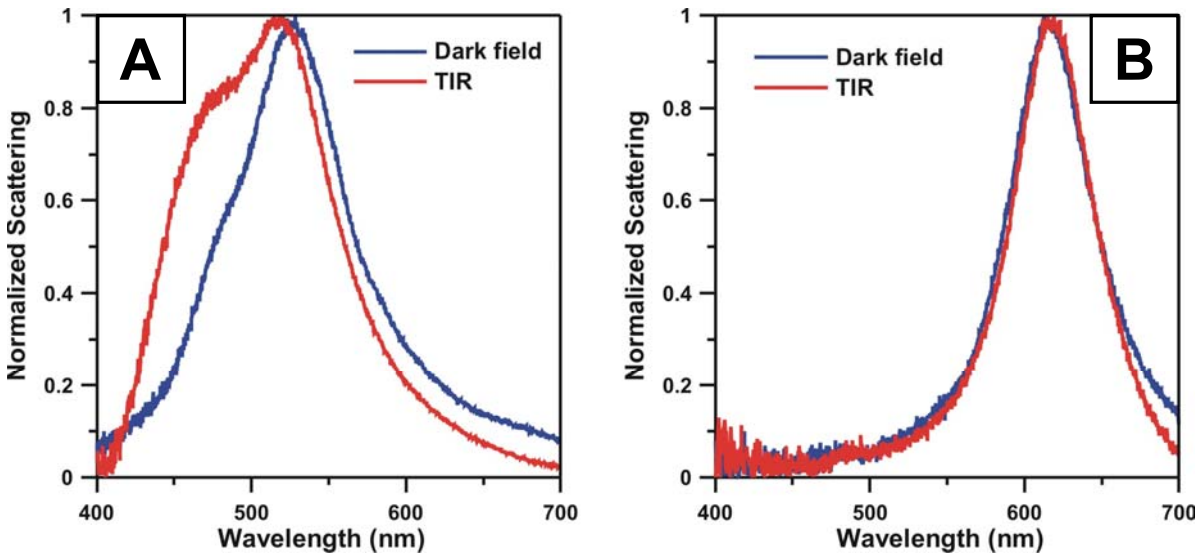

Figure 4.7 A and B each compare the spectra obtained under TIR and transmission dark-field conditions for a single nanoparticle.

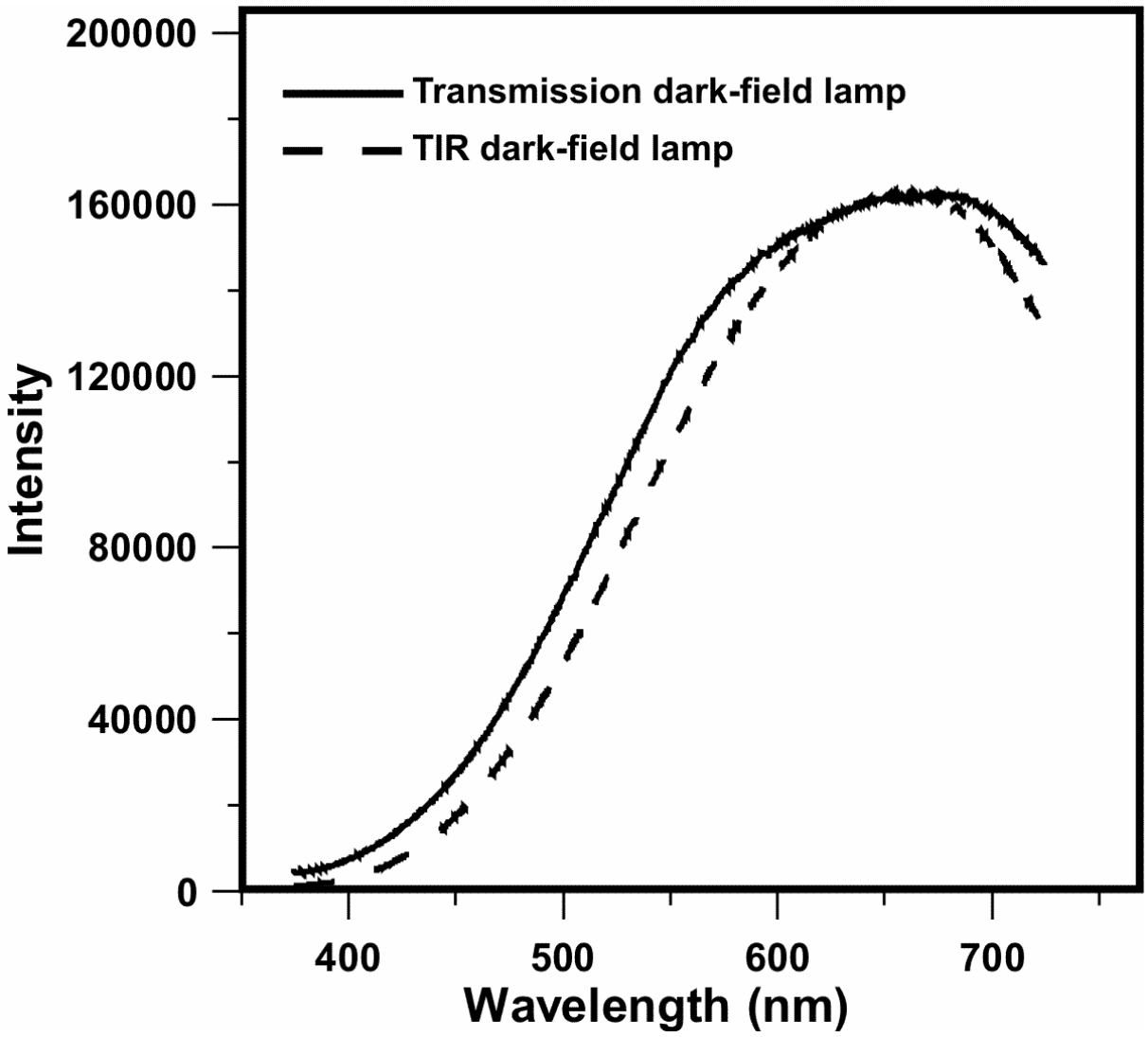

Figure 4.8 Spectral comparison of the light sources used in transmission and TIR dark-field illumination (acquisition times were 0.1 sec for transmission and 1 sec for TIR).

LSPR shown in Figure 4.7A, but it is almost certainly not a flat high aspect ratio particle. It is most likely a spheroid or ellipsoid with an out-of-plane height many times that of the nanoprism's out of plane height. This implies that the ellipsoidal nanoparticle is sampling a much different electromagnetic field than the nanoprism. Again, remember that the penetration depth of the TIR evanescent wave is wavelength dependent. Hence, the taller the nanoparticle the more the spectrum of the light sampled by that nanoparticle is different from the light spectrum under normal illumination conditions. Last, the scattering angles of nanoparticle LSPR modes are dependent on the angle of the illumination light, with this dependence being more severe for quadrupolar modes than for dipolar modes. For transmission dark-field the angle between the incident light and the forward scattering direction is ~125^{o}, and for TIR dark-field the angle is 41.8^{o}. Hence, the difference in the observed spectra in Figure 4.7A may be due to illumination geometry. The latter two arguments concerning the discrepancy in the LSPR measurements will be minimized for thin particles. Therefore, we have limited our studies to triangular nanoprisms.

Figure 4.9 compares reflected and TIR dark-field images acquired with an AFM tip engaged on the sample. Reflected dark-field allows no information about the nanoparticles to be obtained optically in real time with the tip engaged. With TIR, however, it is difficult to even tell where the tip is! This is due to the localization of the evanescent wave to the surface of the sample. Since an AFM tip is ~10 μm tall only ~5% of the tip structure is illuminated, rendering the appearance of the AFM tip as a diffraction-limited spot in the dark-field image. While conducting initial experiments to test the imaging performance of the AFM when in TIR optical

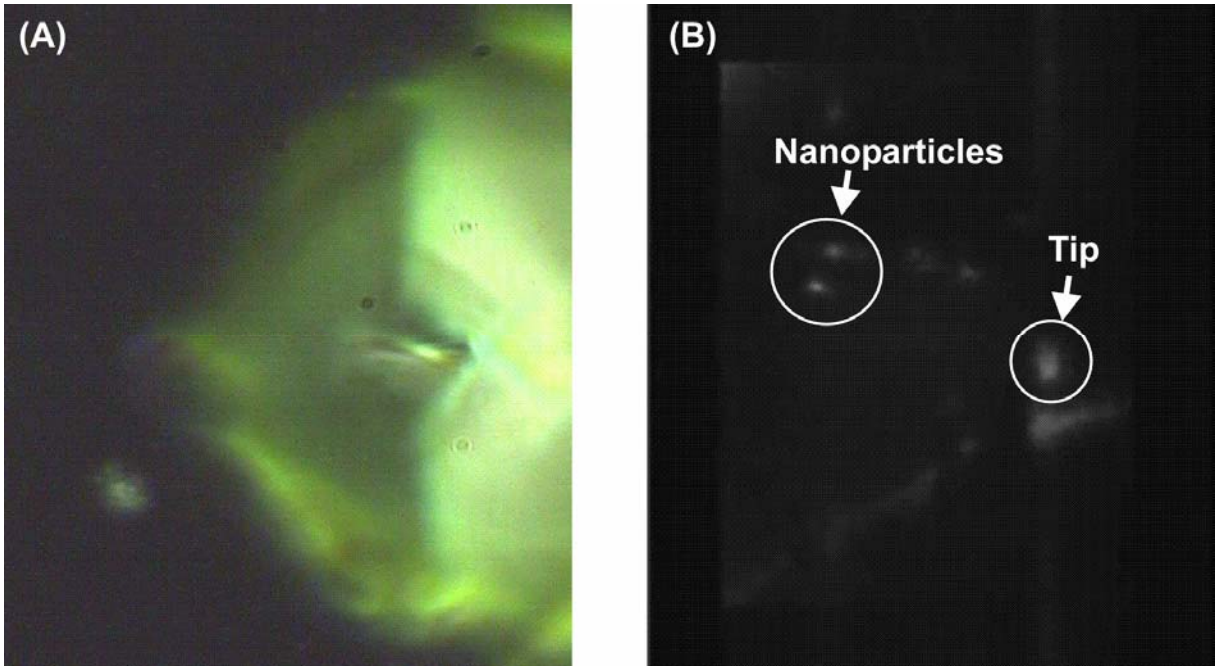

Figure 4.9 Imaging a nanoparticle sample with an AFM tip engaged under A) reflected dark-field conditions and B) TIR conditions.

feedback, we noticed a number of interesting phenomena that have never been directly observed before.

The first phenomenon occurred when we attempted to image a multiwall carbon nanotube. Figure 4.10 shows the image that the AFM yielded from this experiment. It looks as though the experiment utterly failed. The only information available in the AFM image is that the nanotube had been pushed, indicated by the long streaks across the image. Figure 4.11, however, shows a series of dark-field images acquired during the AFM imaging. In each image the nanotube and the tip are circled. As the series shows, the TIR dark-field yields real-time feedback about how the tip and sample are interacting. The nanotube is sometimes passed over by the tip, sometimes pushed by the tip, and is eventually picked-up by the tip. We realized that this could have major implications for nanoparticle manipulation and tip-enhanced Raman experiments if we could reproducibly engineer the desired tip-sample interaction.

Figure 4.12 shows preliminary results towards the goal of nanoparticle manipulation. The series of images shows the AFM tip pushing a nanoparticle in a controlled manner to a new position (the change in the scattering intensities and spot shapes are due to the fact that the illumination field is not uniform across large areas of the field of view, to be discussed later). This is a major advance. It allows for open-loop nanoparticle manipulation with diffraction-limited resolution. This is functionality not possible in any other configuration.

Figure 4.13 shows an SEM image of a single nanoparticle attached to an AFM tip. The ability to attach a single well-defined nanoscale structure to a scanning probe tip is, by itself, a major advance for TERS applications. The ability to select the LSPR of the structure to be attached is a tip-enhanced Raman spectroscopist's dream. Only recently have investigators

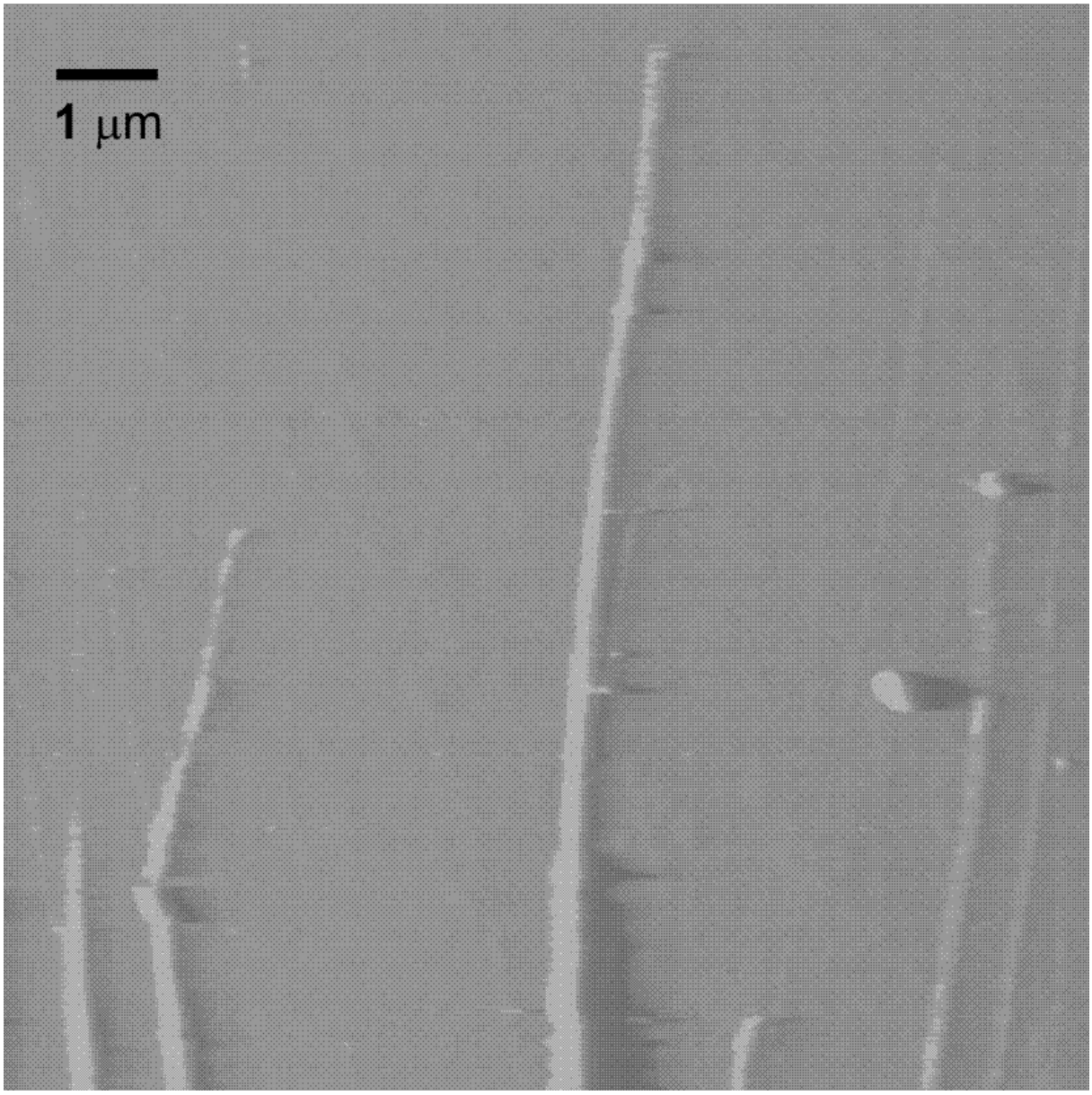

Figure 4.10 Tapping mode AFM image. Here, the streaks indicate that the particles on the substrate were pushed due to their interaction with the AFM tip.

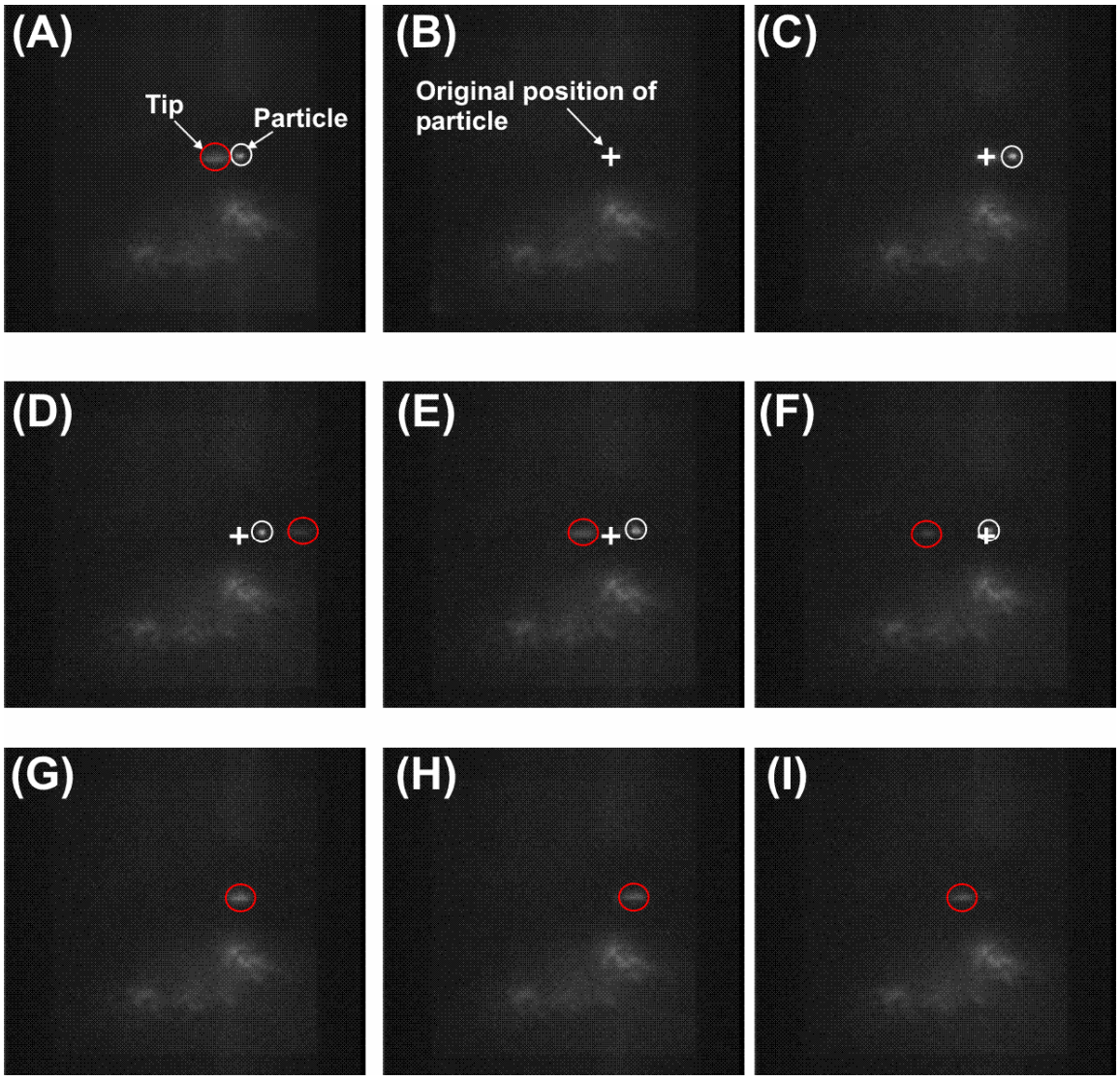

Figure 4.11 Series of TIR dark-field images taken from a movie showing the interaction between an AFM tip and a nanostructure (carbon nanotube) in real time. In frames A-C the particle is picked-up (B) and deposited in a new position (C). In frames D-F the particle is pushed around by the AFM tip. Frames G-I show scattering only from the AFM tip, indicating the particle was picked up by the tip and not redeposited..

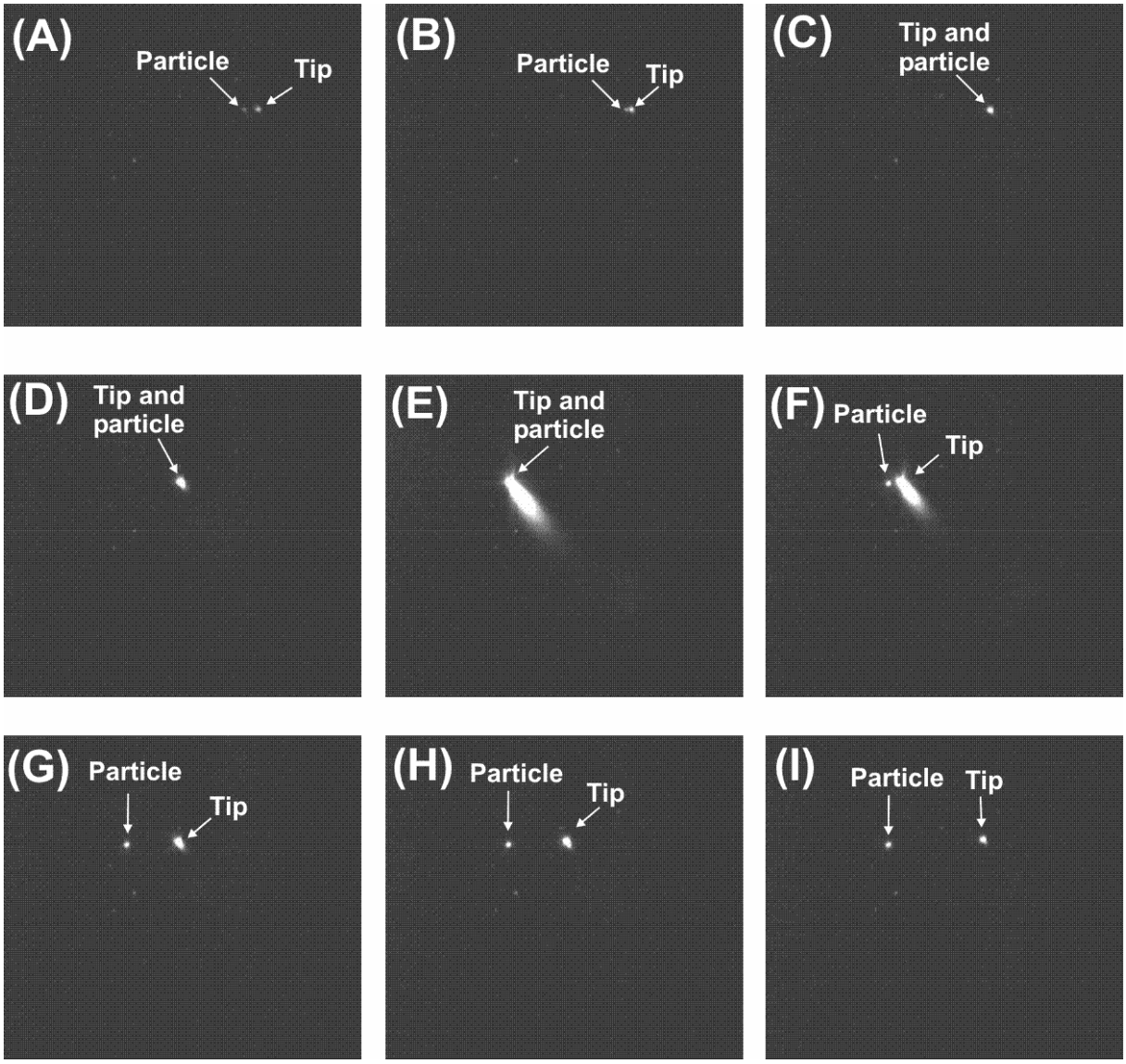

Figure 4.12 Series of TIR dark-field images taken from a movie showing the interaction between an AFM tip and a silver nanoparticle in real time. In this experiment, the particle is smoothly pushed a predefined distance and subsequently left in a new position.

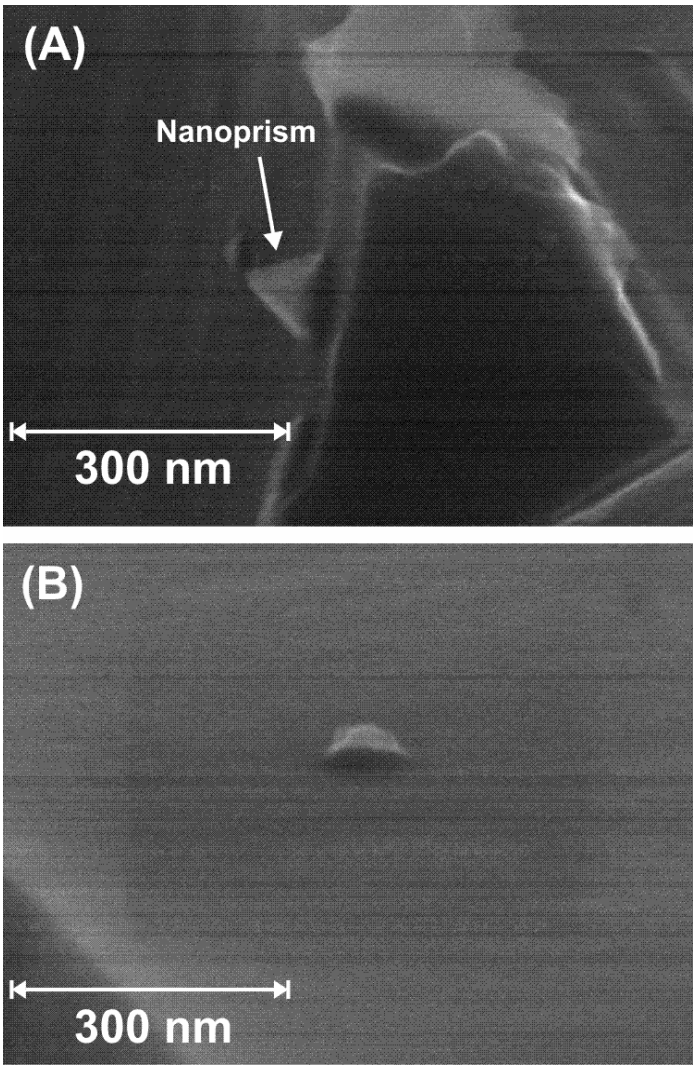

Figure 4.13 SEM images of a single triangular nanoprism attached to an AFM tip. The amorphous structure in (A) on which the particle is supported is the AFM tip. B) The same prism as in (A) with the viewing angle rotated. This process was observed in real-time via TIR dark-field by noting the disappearance of the prism's scattering after the AFM tip passed over it.

characterized the plasmonic properties of a tip used in a TERS experiment,[136] and never has anyone been able to select the LSPR of their tip. The TIR-AFM allows for just that since one can acquire nanoparticle spectra until the desired LSPR is found. Then go directly to that particle with the AFM tip using the optical feedback and pick it up! More work is required to optimize the conditions to perform manipulation and attachment as desired. However, these experiments have demonstrated the proof-of-principle.

Returning to the original goal of this experiment, which was to correlate structural and optical properties *in-situ*, Figure 4.14 shows a correlated LSPR-AFM experiment. Here the TIR dark-field image of the triangular nanoprism to be studied (Figure 4.14A), the spectrum of that nanoprism (Figure 4.14B), and the nanoprism's AFM image (Figure 4.14C) is shown. Everything appears to have worked quite well except that the AFM image looks blurry. This is a consequence of image processing. We were required to filter the AFM image due to noise in the AFM data. We encountered two types of noise: a low frequency component and a high frequency component. Figure 4.15A shows this noise over an image of a NSL array. It was filtering the low frequency noise that led to the blurring of the AFM image seen in Figure 4.14C. The high frequency noise could be filtered with negligible degradation to the image quality. We deduced that the low frequency noise was due to mechanical instability in the z axis of our instrument since this noise was not present in lateral force microscopy images (Figure 4.15B). The presence of the noise was a consequence of coupling a large mass to the bottom of the AFM via the oil immersion objective. The cantilevered turret caused mechanical vibrations to be coupled to the sample via the thin oil layer between objective and substrate. Figure 4.16 shows the design of our solution. Since the source of the vibrations was the turret, we vibrationally

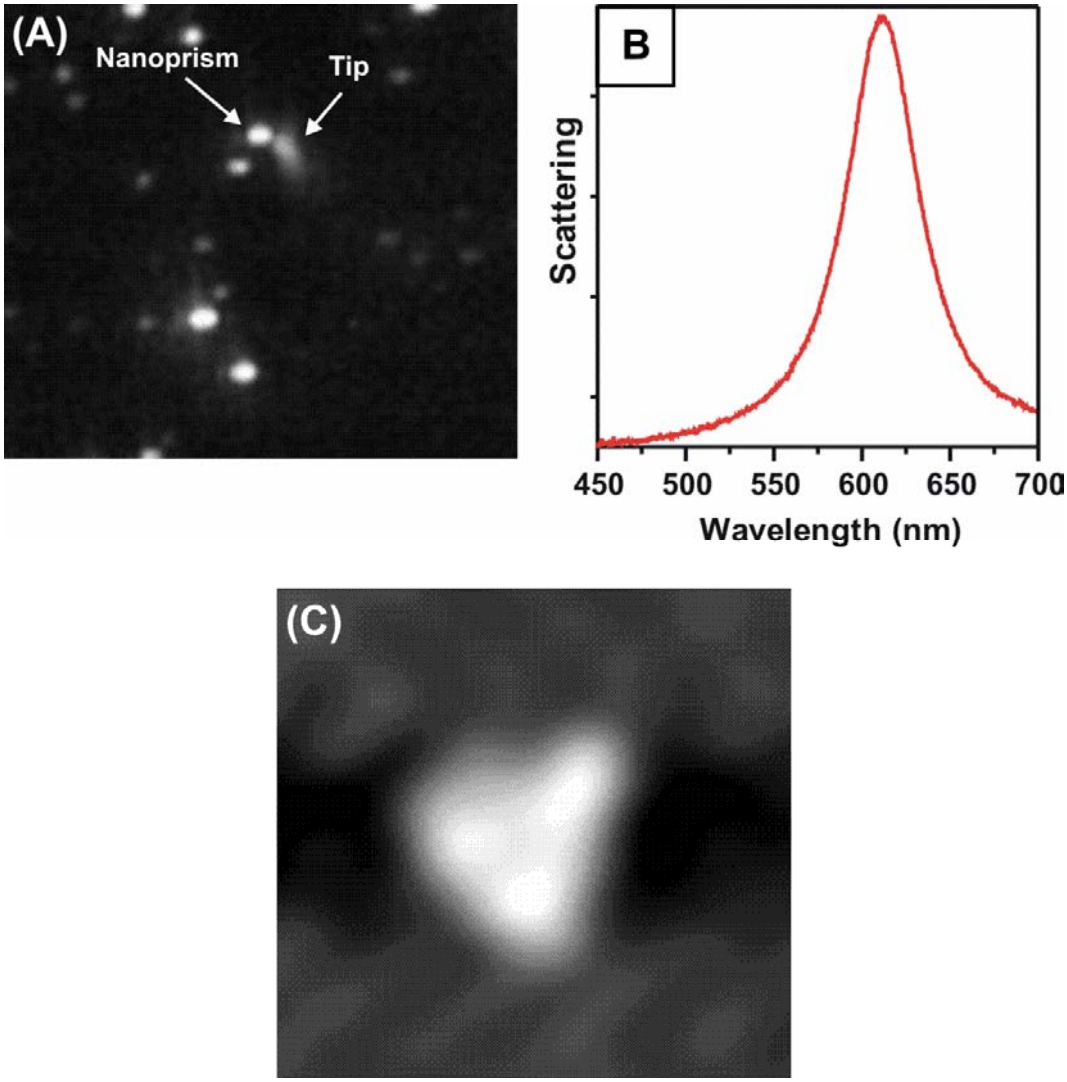

Figure 4.14 Correlated optical and structural measurement of a triangular nanoprism. A) TIR wide-field image showing tip and nanoprism. B) LSPR spectrum from nanoprism identified in (A). C) High resolution AFM image of nanoprism after being processed for noise removal.

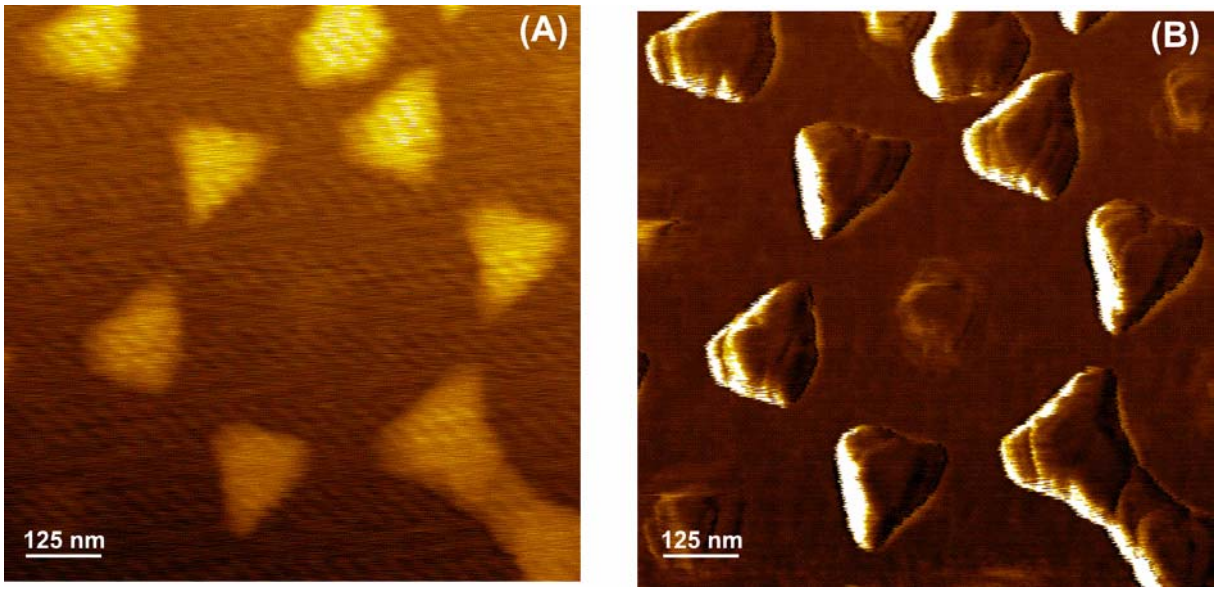

Figure 4.15 Contact mode AFM images acquired with the oil immersion objective in contact with the substrate. A) Topological image of a NSL particle array (D=500 nm) displaying periodic noise. B) Lateral force image of the NSL array showing no periodic noise.

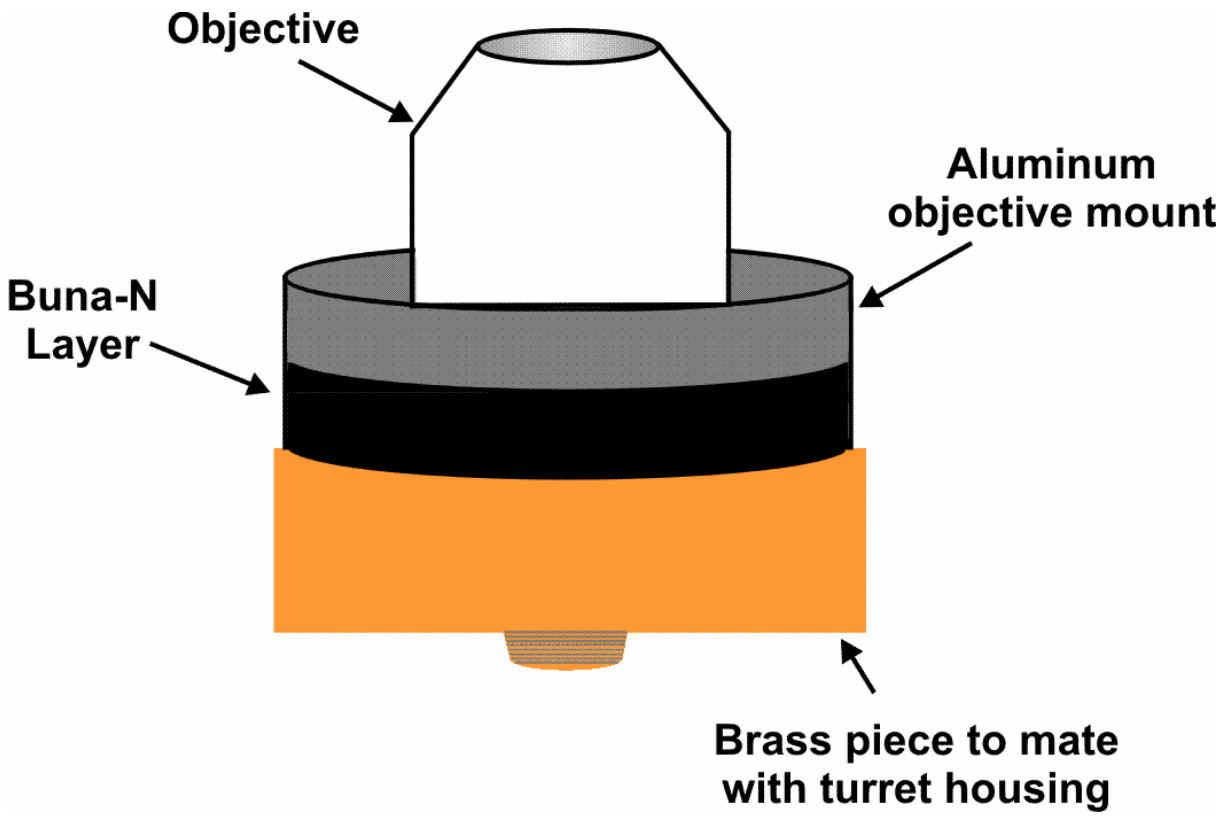

Figure 4.16 Objective "float" for isolating the objective-sample oil interface from mechanical vibrations from the microscope turret.

isolated the objective from the turret via a layer of Buna-N (McMaster Carr). Figure 4.17 demonstrates the improvement in the AFM imaging by showing two topology AFM images: one before vibration isolation (Figure 4.17A) and one after vibration isolation (Figure 4.17B).

4.4 Conclusions

A new approach to correlate single nanoparticle structural measurements with their LSPR spectra has been presented via a TIR illumination geometry mated with an AFM via an inverted optical microscope. It has been shown that *in-situ* real-time optical feedback can not only be acquired during an AFM scan, but that this yields new information that has, to date, been inaccessible. This includes the nature of the tip-sample interaction in situations where the tip sample interaction is stronger than the sample-substrate interaction. While the integration of an AFM into this configuration can lead to new noise pathways that can convolute AFM images, these can be isolated and neutralized by careful engineering and design. While this approach suffers a limitation in correlating the exact geometry of a single nanoparticle to its LSPR spectrum due to the finite size of the probe, it facilitates advances for other studies. First, this instrument opens the door for the creation of novel nanoparticle geometries of interest to the nanoparticle optics community via single nanoparticle manipulation. This system also offers an advance to the field of nanoparticle manipulation by enabling diffraction limited resolution for single nanoparticle manipulation in an open-loop scanning configuration. Prior to this work, directed manipulation of single nanoparticles was impossible via open-loop AFM. Finally, this approach supplies the TERS community with a technique by which to functionalize scanning probe tips with well defined nanostructures of virtually any LSPR energy desired. This is, to our

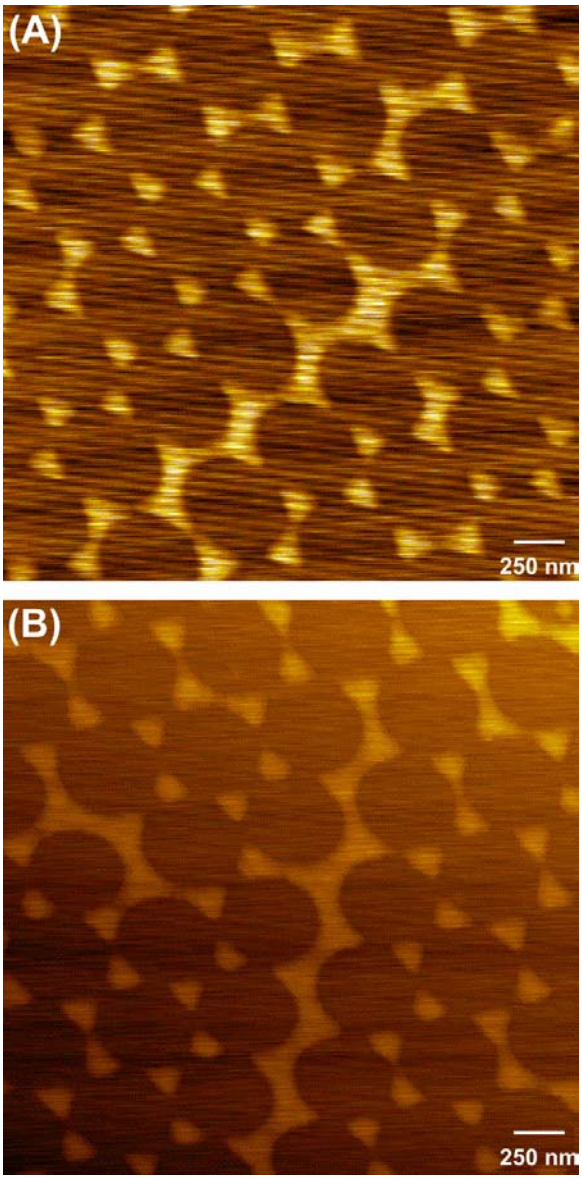

Figure 4.17 Tapping mode AFM images acquired with TIR oil immersion objective engaged with the substrate A) before floating the objective and B) after floating the objective. Scanning conditions were identical for each image.

knowledge, the only technique available to select both the LSPR and the geometry of a nanostructure for use in a TERS application.

Part II: Chapter 5

Using High-Resolution Transmission Electron Microscopy to correlate Nanoparticle Optical and Structural Properties

5.1 Introduction

Chapter 4 discussed real time *in-situ* structural and optical microscopy measurements by combining TIR-AFM. While this approach is a giant leap forward for single nanoparticle studies there is still one limitation to the approach. The structural resolution by AFM will never exceed the diameter of the probe tip (~5-10 nm). Hence, this technique enables us to definitively identify the shape of nanoparticles (cubes, prisms, rods, etc.) responsible for particular spectral fingerprints and refractive sensitivities, but does not allow us to investigate the sub-5nm structural details that affect plasmonic properties. For example, it has been shown that a 1 nm variation in the radius of curvature of a nanoprism's tips has a measurable effect on the LSPR spectrum, and appears to have a large effect on its refractive index sensitivity.[133] Also, many interesting plasmonic effects yet to be investigated lie in the regime where two or more nanoparticles are separated by less than 5 nm. It has been suggested that studies of such systems could yield the key to understanding single molecule SERS.[137, 138] AFM, being limited to measuring features of 10 nm or more, cannot aid in such studies.

Much of the work in the Van Duyne group has been concerned with the utility of nanoparticles as chemical sensors.[56-58, 75, 133] This work has been concerned explicitly with maximizing the shift experienced by the LSPR when its environment is changed. While this is the primary concern in sensing experiments, it is not the only factor that influences sensitivity. To this end we have defined a figure of merit (FOM) to aid in comparing the relative utility of nanoparticles of various shapes (Eq. 2.1).[75]. An important component of the FOM is the LSPR linewidth. This, along with discoveries of narrow plasmons in other nanoparticle systems,[75, 82] motivated us to consider the question of how narrow an LSPR could be, and what factors

determine the observed linewidth. While investigators have studied the lifetime and dephasing dynamics of nanoparticle LSPRs under various conditions,[122, 139-142] none have conducted detailed single particle studies of the influence of the various intrinsic and extrinsic structural factors affecting the LSPR linewidth. Moreover, only one of these studies was conducted on single nanoparticles, and only used one technique (NSOM) to investigate the nanoparticles' properties.[122] Under such experimental conditions it is impossible to accurately assign the relative importance of all possible factors on the LSPR linewidth.

The intrinsic effects are generally associated with a nanoparticle's dielectric properties, and dominate the LSPR linewidth for nanoparticles smaller than the electron mean free path of their material (gold, silver, copper, etc.). The extrinsic effects are generally considered to dominate the LSPR linewidth for nanoparticles larger than the electron mean free path, and are contingent on the details of a nanoparticle's structure. Hence, in order to discuss the plasmon linewidth in a manner that encompassed all possible factors we needed a technique that allowed us to probe both the internal and external structure of our nanoparticles with exquisite resolution. Transmission electron microscopy (TEM) is the ideal technique for these studies.

TEM allows for sub-nanometer resolution of structural features due to the extremely small wavelength of electrons (12.3 pm at 10 keV). The fact that electrons do have a wavelength, however, allows for the internal crystallographic structure of our nanoparticles to be interrogated via diffraction. There are many different crystallographic nuances that can affect the plasmon linewidth such as twinned planes, stacking faults, dislocations, grain boundaries, etc. Before results on the intrinsic and extrinsic influences on plasmon linewidth are presented, however, how these factors are understood within the theoretical framework will be discussed.

Many theories of nanoparticle optics, such as Mie theory, do not explicitly account for structural influences on the LSPR. These theories use macroscopic material dielectric properties. Hence, the linewidth in these theories is defined by the optical plasmon modes that are excited. The larger linewidths observed for larger particles are accounted for by the excitation of higher order modes and retardation effects.[33, 116] The dephasing of the electronic polarizations caused by the simultaneous existence of many plasmon modes (dipole, quadrupole, etc.) leads to broader plasmon linewidths in such a paradigm. Real nanoparticle systems, however, have structural features, as noted above, that are not accounted for within the macroscopic description of the material dielectric function. For these structures information about the plasmon bandwidth can be modeled by correcting the macroscopic dielectric function.

The real part of a metal's dielectric (ε_r) function is generally modeled as a sum of an interband term and a free electron gas term:

$$\varepsilon_r(\omega) = \varepsilon_{rIB}(\omega) + \varepsilon_{rD}(\omega) \tag{5.1}$$

The free electron term is modeled with the Drude-Sommerfeld model:[139, 140, 143]

$$\varepsilon_{rD}(\omega) = 1 - \frac{\omega_p{}^2}{\omega^2 + i\gamma\omega} \tag{5.2}$$

Here ω_p is the well-known bulk plasmon frequency of a free electron oscillation expressed in terms of the free electron density N as discussed in Chapter 1, and γ is the phenomenological damping constant of the bulk material. For small particles (1-5 nm) γ has been corrected for the intrinsic size effect discussed above where the nanoparticle is smaller than its electron mean free path:

$$\gamma(R) = \gamma_0 + \frac{A * v_F}{R} \tag{5.3}$$

where γ_0 is the bulk damping constant (determined by electron-electron, electron-phonon, and electron-defect scattering), v_F is the Fermi velocity, R is the nanoparticle radius, and A includes details of the scattering process. Both electromagnetic and quantum mechanical theories have deduced this 1/R dependence to explain the intrinsic effect on the linewidth of small particle LSPRs, and found varying degrees of quantitative agreement.[144-147]

In this chapter studies of four nanoparticle systems will be presented: nanorods, triangular nanoprisms, nanocubes, and colloidal clusters. In these experiments the LSPRs of single nanoparticles were correlated with high resolution TEM (HRTEM) images. These are not the first studies correlating TEM images with nanoparticle optical measurements. Sherer *et al* correlated the second harmonic (SHG) signal generated from nanoparticle aggregates with TEM images of the aggregate structures.[148] Using this approach they were able to locate the SHG "hot spots" within multi-particle aggregates. Mock *et al* studied the effect of nanoparticle geometry on the LSPR spectra by correlating TEM and LSPR measurements of single nanoparticles.[135] These studies verified a number of the theoretically predicted trends, discussed previously in this thesis, for the dipole mode of triangular nanoprisms. However, these studies only addressed the effect on the LSPR for external geometry changes for one particle structure (prisms). They did not study how changes in the internal structure of the nanoprisms may have affected the LSPR (this particularly important here since the investigators used temperature changes to alter the prism's geometry), and they only discussed the relative spectral position of the in-plane dipole LSPR mode.

The studies presented here will expand on these studies by addressing how the LSPR linewidth is affected by internal and external geometric factors for multiple nanoparticle

geometries. There were three objectives for these studies: (1) prove the geometry of the nanoparticles responsible for spectra such as those shown in Chapters 1 and 2, (2) understand the contribution of nanoparticle geometric features on the LSPR linewidth, and (3) understand the role of internal structural defects on the LSPR linewidth.

5.2 Materials and Methods

5.2.1 Materials

Substrates for all experiments were commercially available copper TEM grids with a 50 nm formvar polymer and 2-3 nm amorphous carbon layer (Ted Pella, Redding, CA)). These grids were placed on 18 mm No. 1 glass coverslips from Fischer Scientific (Pittsburg, PA). Glassware preparations utilized H_2O_2, H_2SO_4, HCl, HNO_3, and NH_4OH from Fischer Scientific, and ultrapure H_2O (18.2 MΩ cm^{-1}) from a Millipore academic system (Marlborough, MA). Sodium borohydride (99%), trisodium citrate dihydrate, silver nitrate (99.9999%), and poly-L-lysine (98%) were purchased from Aldrich (Milwaukee, WI). Bis(p-sulfanatophenyl) phenylphosphine dihydrate dipotassium salt (BSPP) was purchased from Strem Chemicals (Newburyport, MA).

5.2.2 Sample Preparation

When ready to use, a 2-10 μL aliquot of nanoparticle solution was drop-coated onto the surface of a TEM grid. The substrate was then left to dry in air until the nanoparticle suspension droplet was no longer visible by eye. This was necessary because if the TEM substrates were placed on the glass slides before the water droplet evaporated, the hydrophilic glass surface

would pull the suspension over the TEM grid's edges onto the glass. Samples were then further dried in an N_2 environment for ~1 hr.

Colloidal suspensions of silver nanoparticles were synthesized by reducing silver nitrate with sodium citrate by an established scheme pioneered by Lee and Miesel.[134] In this approach 90 mg of silver nitrate and 500 mL of ultrapure water are combined and brought to a boil in a 1 liter cleaned flask (3 HCl:1 HNO_3). Then 10 mL of a 1% sodium citrate solution was added while stirring vigorously. This solution was boiled for 30 minutes. During this time the solution undergoes a color change sequence: first to light yellow followed by a change to an opaque brown. After the 30 minutes, the new suspension was allowed to cool and transferred to a brown glass bottle for storage. Most of the nanoparticles in such a suspension are spherical in shape with a diameter ~ 40 nm. However, many other geometries are also present such as: triangular prisms, rods, cubes, hexagonal plates, and many others.

Suspensions of triangular nanoprisms were synthesized by an established technique pioneered by Jin et al.[59] This is a two step synthesis where a seed solution of silver colloids (~8 nm) serve as the starting material for triangular nanoprism formation. First, nanopure water (95 mL), aqueous trisodium citrate (1 mL of 30 mM, freshly prepared), and aqueous silver nitrate (2mL of 5 mM, freshly prepared) were mixed in a 250 mL 3 necked flask that had been cleaned with aqua regia for at least 3 hours. This solution was immersed in an ice bath and stirred for 30 minutes. During this time inert gas (Ar or N_2) was bubbled through the solution. After 30 minutes the inert gas flow was terminated, and each neck of the flask was corked with a rubber stopper. Aqueous sodium borohydride (50 mM) was then made using ice-cold ultrapure water. 1 mL of this solution was quickly injected into the ice-cold solution by a syringe through the

center rubber stopper. The clear solution turned pale yellow immediately (note: if a blue color that fades to light yellow appears initially, the seed solution is unusable). The reaction was allowed to proceed for an additional 15 minutes. 1 mL of BSPP and 0.5 mL of sodium borohydride solutions (50 mM, freshly made with ice-cold water) were then added dropwise over a five minute period. The resulting suspension of small silver colloids were immediately divided into 10 mL vials and irradiated with a fluorescent lab lamp overnight. After the irradiation period the suspension changed from yellow to deep green or blue, indicating the formation of triangular nanoprisms.

5.2.3 Structural Characterization

A JEOL JEM-2100F Fast TEM (Tokyo, Japan) operating at an accelerating voltage of 200 kV was used to acquire all transmission electron microscope data: standard images, electron energy loss spectroscopy (EELS), and dark-field TEM.

5.2.4 Optical Characterization

All single nanoparticle scattering spectra were obtained with either a Nikon *Eclipse* TE300 or Nikon *Eclipse* TE2000-U inverted optical microscope (Nikon, Japan) coupled to a SpectroPro 300i imaging spectrometer and a liquid nitrogen cooled Spec-10:400B CCD detector. These microscopes use tungsten filaments for illumination. This illumination was focused on the sample surface by a Nikon 0.8-0.95 numerical aperture (NA) dark-field condenser. Single nanoparticles scattered this light into the collection optics. For this approach it was critical that the NA of the objective (collection optic) was smaller than the NA of the condenser so that none of the illumination light would be collected. A Nikon variable aperture (NA=0.5-1.3) 100X oil

immersion objective was chosen for this purpose. Figure 2.1 shows a schematic of this apparatus, and section 2.2.5 explains the procedure for all data acquisition.

In order to correlate the LSPR and TEM images we used a TEM grid with an asymmetric center mark as shown by Figure 5.1. Due to this mark we were able to define a coordinate for each section of the grid. The grid was divided into four quadrants: (+,+), (+,-), (-,+), (-,-). Counting sections from the center grid mark gave numeric values to the coordinate, while the sign of the numbers gave the quadrant. Then low magnification TEM images were correlated with high magnification LSPR images (TEM has ~10,000 times high magnification capabilities than optical microscopy making low resolution TEM comparable to high resolution optical microscopy) as shown by Figure 5.2.

5.3 Results and Discussion

5.3.1 Nanorods

One of the two most interesting questions within the scope of these studies was what structural features result in the narrowest LSPRs. While this is still an open subject within the scope of all possible parameters affecting plasmon linewidth, preliminary studies on overall nanoparticle geometry indicate the answer to be rod-like structures. Figure 5.3 shows the LSPR spectra and TEM images of nanoparticles that yielded the narrowest LSPRs that could be found from sampling hundreds of particles. Considering that the crystal structure of the silver nanorods is the same as that of any of our other particles, I will approach this discussion from a classical argument since the eigenstates of the system are determined by the crystal structure.

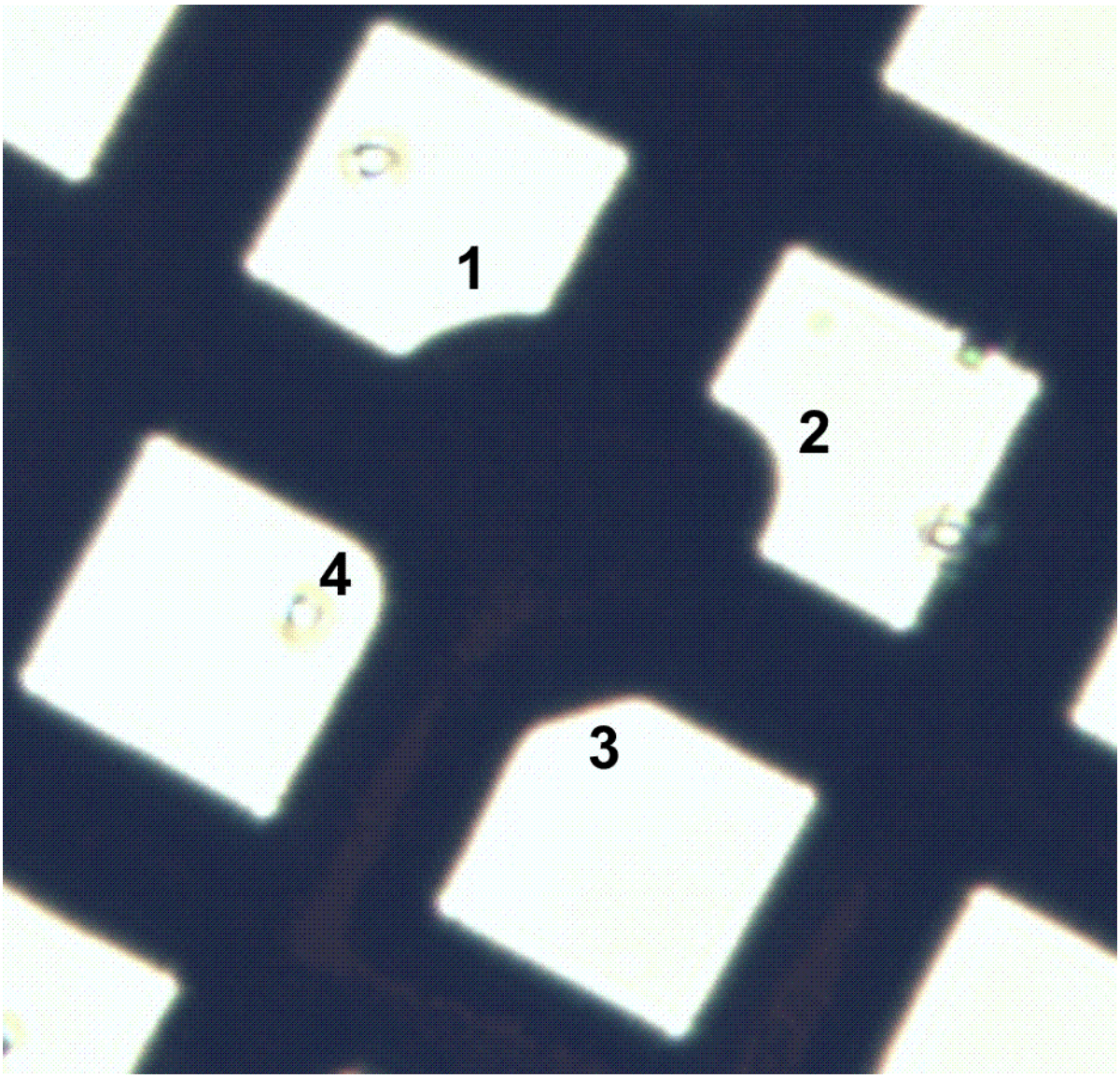

Figure 5.1 Bright-field optical microscopy image showing the asymmetric center mark of the TEM grids.

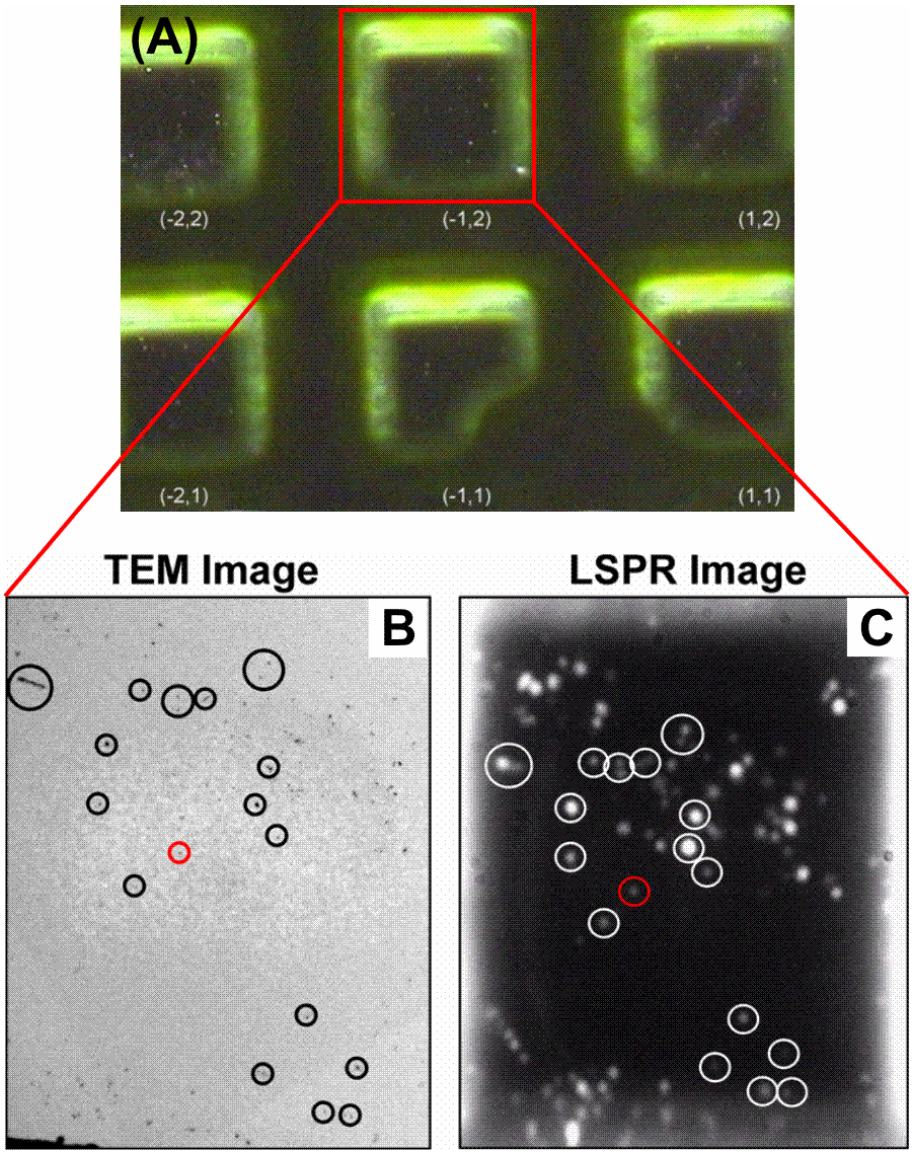

Figure 5.2 Correlation of TEM and LSPR images. A) Low resolution (40x) dark-field image of grid (-1,2). B) Low resolution TEM image of grid (-1,2). C) High resolution (100x) LSPR image of grid (-1,2).

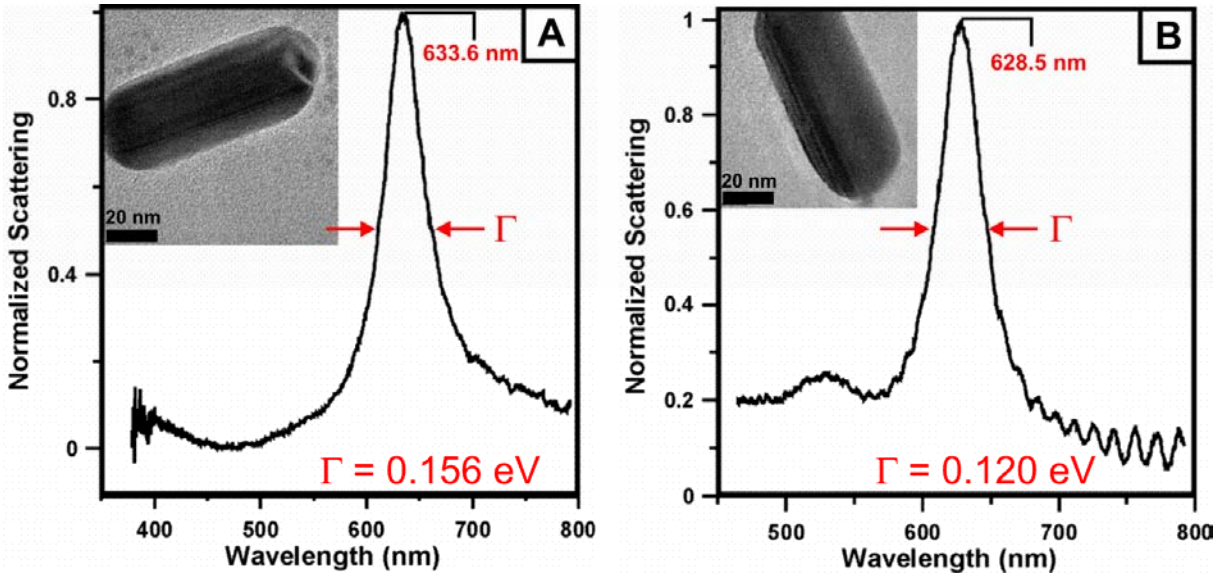

Figure 5.3 Correlated LSPR spectra and high resolution TEM images of single silver nanorods. These structures displayed the narrowest LSPR linewidths found from surveying hundreds of nanoparticles of various geometries.

As discussed in Chapter 1, the LSPR can be analyzed as a longitudinal density wave bounded by the nanoparticle surface. If one excites such an oscillation in the in-plane dimension for a sphere it is clear that the period of oscillation is not uniform across the entire sphere. This is due to the changing boundary conditions that exist as a consequence of the sphere's curvature as one moves through a sphere along the out-of-plane axis. This causes the polarization of the nanoparticle to be imperfect leading to a decoherence in the electrons' energies. This broadens the linewidths of such geometries' LSPRs beyond the effects of dynamic depolarization. A cylinder whose major axis lies in-plane is the perfect geometry in which to induce a collective longitudinal wave since all the electrons have exactly the same boundary conditions when excited along the major axis. This is shown schematically in Figure 5.4. Hence, nanorods remove one linewidth broadening mechanism from their major axis LSPRs, and could explain why we find the narrowest LSPRs in such structures. If this is true, however, it would be expected that the transverse dipole resonance would have a broader linewidth than that of the longitudinal plasmon. Figure 5.5 demonstrates that this is indeed true for gold nanorods (3:1 aspect ratio with a length of ~70 nm). Gold nanorods are used to demonstrate this since there is a much larger degree of control for synthesizing gold nanorods, and, therefore, much easier to fabricate particles with both LSPR dipole modes within the optical spectrum. It should be noted that these results are taken from an earlier study, and correlated TEM images are not available for these particular structures. The spectrum in Figure 5.5 A shows a ratio of 2.11 between the two LSPRs, while Figure 5.5 B shows a ratio of 1.37. The ratio for spectrum A may be artificially high from a purely geometric argument due to the transverse dipole resonance lying very close to the gold interband transition, which could further damp the resonance. Both

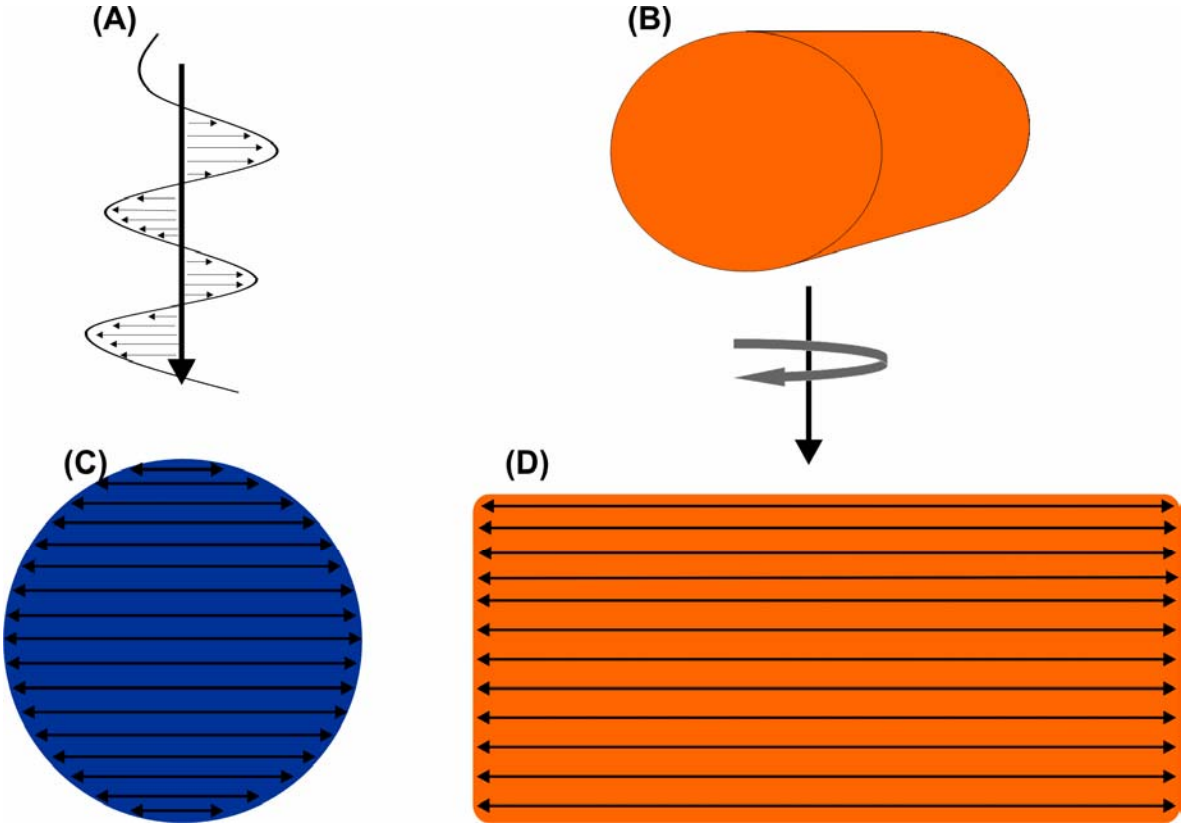

Figure 5.4 Idealized comparison of the electronic polarization of spheres and cylinders. A) Excitation geometry. B) Idealized geometry of a nanorod. C) In-plane cross-section of a nanosphere showing the inhomogenous electronic polarization. D) In-plane cross-section of a nanorod showing the homogenous electronic polarization.

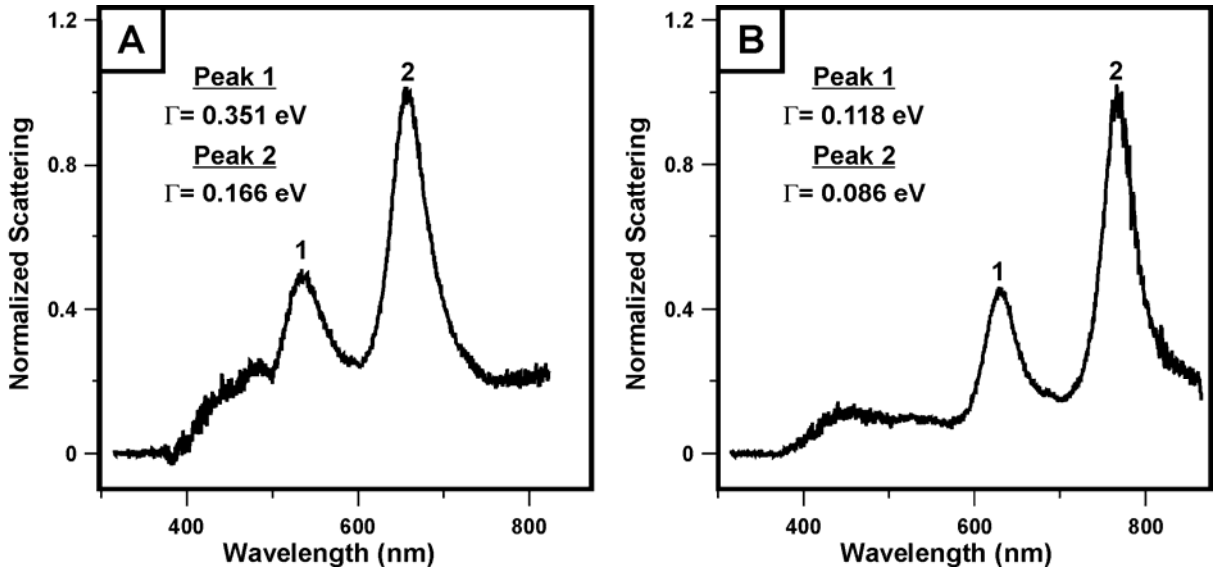

Figure 5.5 LSPR spectra of single gold nanorods demonstrating that the longitudinal dipole plasmon resonance shows a narrower linewidth than the tranverse dipole resonance.

resonances in spectrum B, however, are above 600 nm, and the linewidth should be dependent on the factors discussed above. In fact, the linewidth of 86 meV is, to our knowledge, the narrowest nanoparticle LSPR linewidth measured to date. From such an argument, however, it would seem that atomically flat structures with perpendicular sides would also lead to narrow LSPRs. Fortuitously, we have access to such structures by means of the triangular prisms and nanocubes studied in Part I.

5.3.2 Triangular Prisms

While triangular nanoprisms do fit the afore stated requirement of being flat, they are of lower symmetry than cylinders, and therefore should also experience imperfect polarization of their electrons. However, these nanostructures are extremely thin (~10 nm) meaning dynamic depolarization should be minimized in such structures. Also, it has been shown from DDA calculations that the main dipole LSPR peak for nanoprisms come from the tip regions. This can be understood in terms of the argument put forth by Pines and Bohm.[149] They argue that there is a critical dependence of the collective oscillation of an electron gas on the electron density. They say that higher density promotes collective behavior, while lower density leads to random particle dynamics. This is due to the nature of the coulomb interactions between the electrons. Coulomb interactions are long range interactions. So, the closer the electrons are together the more electrons each single electron's motions impact. This causes a cascading effect that leads to a coherent ensemble dynamic. In less dense environments, however, each electron does not interact with enough electrons to propagate the effect of the ensemble. Thus, random thermal motions of the electrons lead to decoherence of the system's polarization. In the nanoprism system the electrons are forced to the boundary of the nanoprisms (i.e. the tips) by

electromagnetic radiation. This causes an increase in electron density, and therefore an increase in collective dynamics, which leads to a pure dipole. This also explains why the quadrupole is effective only in the center of nanoprisms. Here, the electron density is lower than at the tips allowing for more random thermal motion of the electrons. This causes the polarization information to be localized, which allows for higher order modes to be excited.

These arguments support a result of a narrow plasmon for nanoprisms. Linewidth broadening from polarization decoherence that is normally associated with particles of low symmetry or high curvature is countered by the localization of the dipoles on the tips, and broadening due to dynamic depolarization is countered by nanoprisms' thinness. However, the LSPRs of nanoprisms are broader than those of nanorods. We attribute this to the well-known lightning rod effect seen in conductors with sharp tips. Under this hypothesis the LSPRs of nanoprisms with sharper tips should show broader linewidths. Figure 5.6 shows preliminary data supporting this hypothesis. It should be noted that it is not necessary for the tips of the triangles to be the most "well-formed" to show the broadest LSPRs. Instead, there only needs to be sharp features. The nanoprism in Figure 5.6A has a better formed tip structure than the nanoprisms in Figures 5.6B-D, but actually has a lower radius of curvature for its sharpest feature. Hence, the nanoprism in Figure 5.6A has the smallest LSPR linewidth.

5.3.3 Nanocubes

Within the context of the argument used in the last two sections, one would hypothesize that nanocubes would have a wide LSPR. While they will have perfect coherence in their electronic polarizations they have one more tip than triangular nanoprisms, and they will suffer from dynamic depolarization due to their thickness (3 to 10 times that of nanoprisms). However,

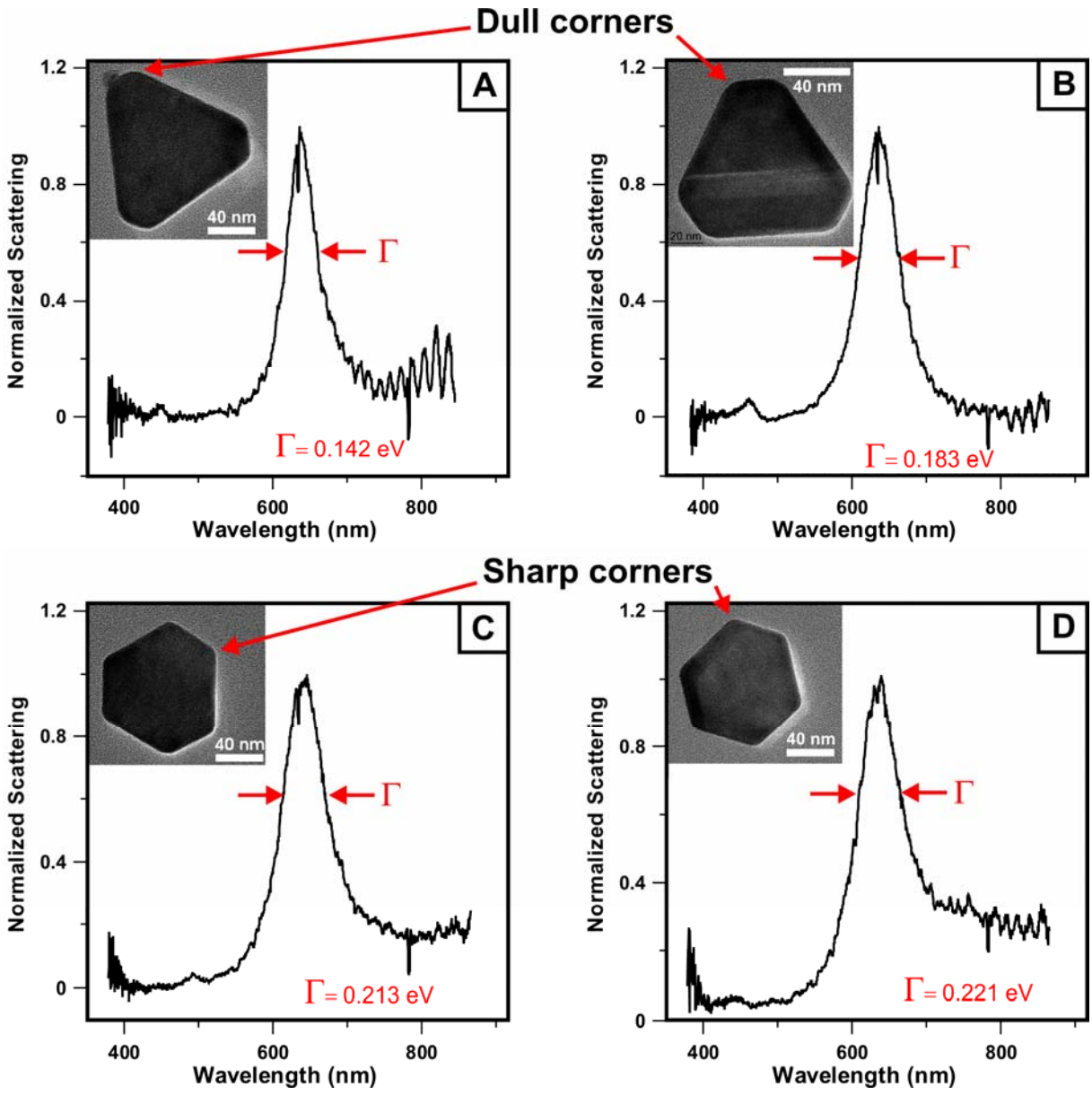

Figure 5.6 Series of correlated LSPR spectra and high resolution TEM images showing that the width of a nanoprism's dipole LSPR is affected by the corners' radius of curvature.

as shown in Chapter 3 nanocubes show two LSPR peaks, and these are assigned as dipolar resonances associated with the polar regions of the cube where the electromagnetic fields are most intense. The two peaks are a result of the two dielectric environments present: the substrate, which is responsible for the lower energy peak, and the gas or solvent environment, which is responsible for the higher energy peak. This study, however, did not prove that the observed LSPR spectra were a result of nanocube LSPRs, and did not address the difference in the relative linewidths of the two resonances. Figure 5.7A shows a correlated LSPR spectrum and HRTEM image of a nanocube, definitively proving that nanocubes are the source of this LSPR fingerprint. Figure 5.7B-F shows how the LSPR spectrum of a nanocube can be compromised by factors varying from the substrate to structural deformation. The ratio between the linewidths of the nanocubes' two peaks has been observed to range from 1.9 to 3.1, with the nanocube shown in Figure 5.7A having a ratio of 2.03. Interestingly, Kreibig and coworkers observed an increase in the plasmon resonance of small silver clusters (2 nm diameter) by approximately a factor of 3 for experiments comparing the LSPR of free silver clusters in a cluster beam produced from supersonic expansion and clusters supported on a glass substrate.[150] It was found that only chemical interface damping (CID) could account for the drastic change in the plasmon linewidth. In the CID model, energy is transferred from the nanoparticles to the surrounding (or supporting) medium through temporary charge transfer reactions. These studies were conducted on much smaller particles than described here. However, the effect should be of approximately equal magnitude for larger nanoparticles if they have high surface area to effective volume ratios. I use the term effective volume because a cube low surface area to volume ratio relative to other geometries. However, I would remind the reader that the field

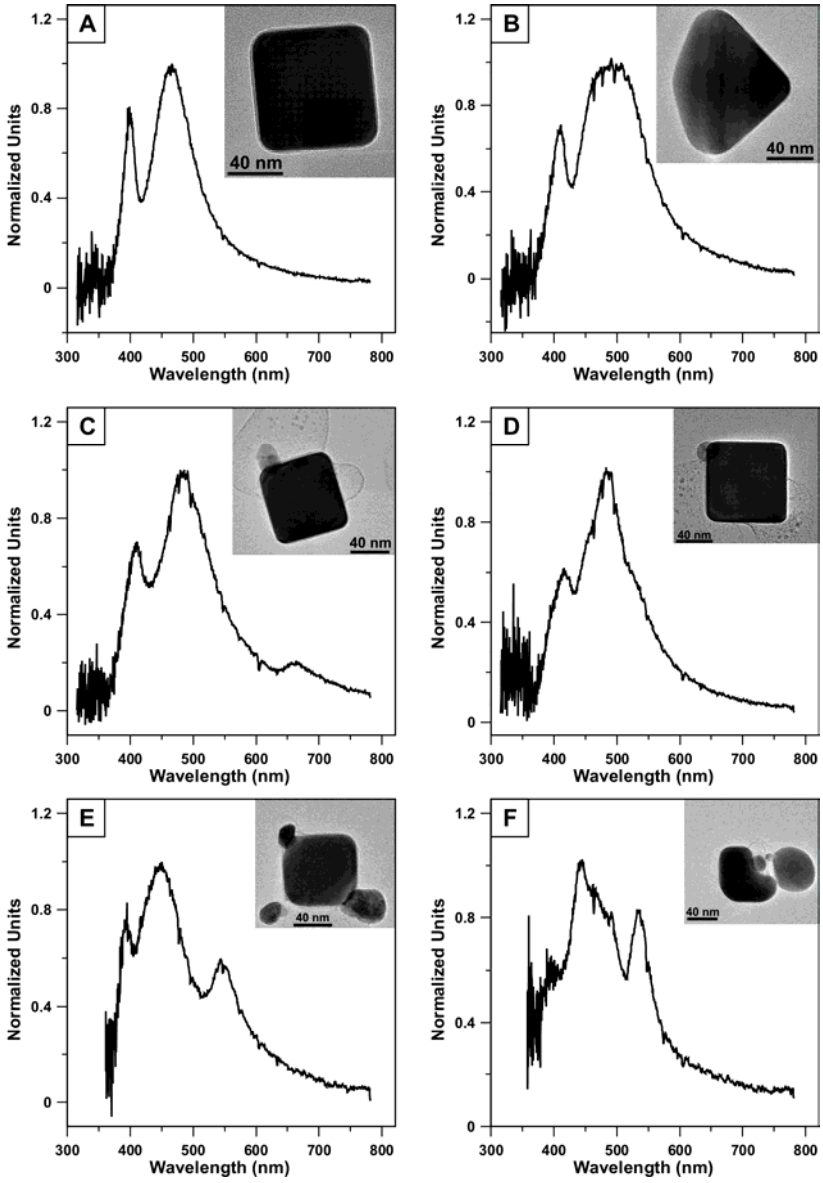

Figure 5.7 Series of correlated LSPR and high resolution TEM images of nanocubes. A) Ideal nanocube. B) Nanocube lying on its edge or a right bipyramid. C, D) Nanocubes on an imperfect section of substrate. E) Nanocube with small colloids in close proximity. F) Structurally compromised nanocube

pattern of a nanocube is unique. The enhanced electromagnetic fields are localized at the poles of a nanocube, allowing interactions with the surface to play a large role in the decay of electronic excitations. Therefore, it is not unreasonable that CID could account for the difference in the linewidths of a nanocube's two LSPR peaks. Unfortunately, it is difficult to compare these measurements with those of free nanocubes, since it is almost impossible to obtain a scattering spectrum of a single nanoparticle without the use of a substrate, and comparisons with ensembles of nanoparticles is useless due to inhomogenous linewidth broadening.

5.3.4 Nanoparticle Clusters

Figure 5.7 alludes to one other interesting dynamic of nanoparticle LSPR spectra: how do the interactions between nanoparticles affect the LSPR of each, the aggregate as a whole, and which nanoparticles dominate the LSPR? Figure 5.8 shows a number of different nanoparticle aggregate structures. Figure 5.8A-D show spectra from aggregates of 2-4 nanoparticles. The spectra are quite complicated with many peaks of varying intensities. Figure5.8E and F, however, show the LSPR spectra from nanoparticle dimers where each of the nanoparticles in the dimer are the same geometry. These spectra look very much like single nanoparticle spectra, and without the aid of correlated TEM imaging would be interpreted as such in a single nanoparticle experiment. This is an important discovery in the context of the single nanoparticle sensing studies presented in Chapter 2. In these studies, we found the sensitivities of single nanoprisms' LSPRs to surface modification with alkanethiols to be, at times, inconsistent with our expectations based on ensemble experiments and theoretical calculations. Figure 5.8E and F reveal a possible mechanism to explain these unexpected results. Figure 5.8E illustrates this especially well. In Chapter 2 a result was found for a nanoprism where the quadrupole mode

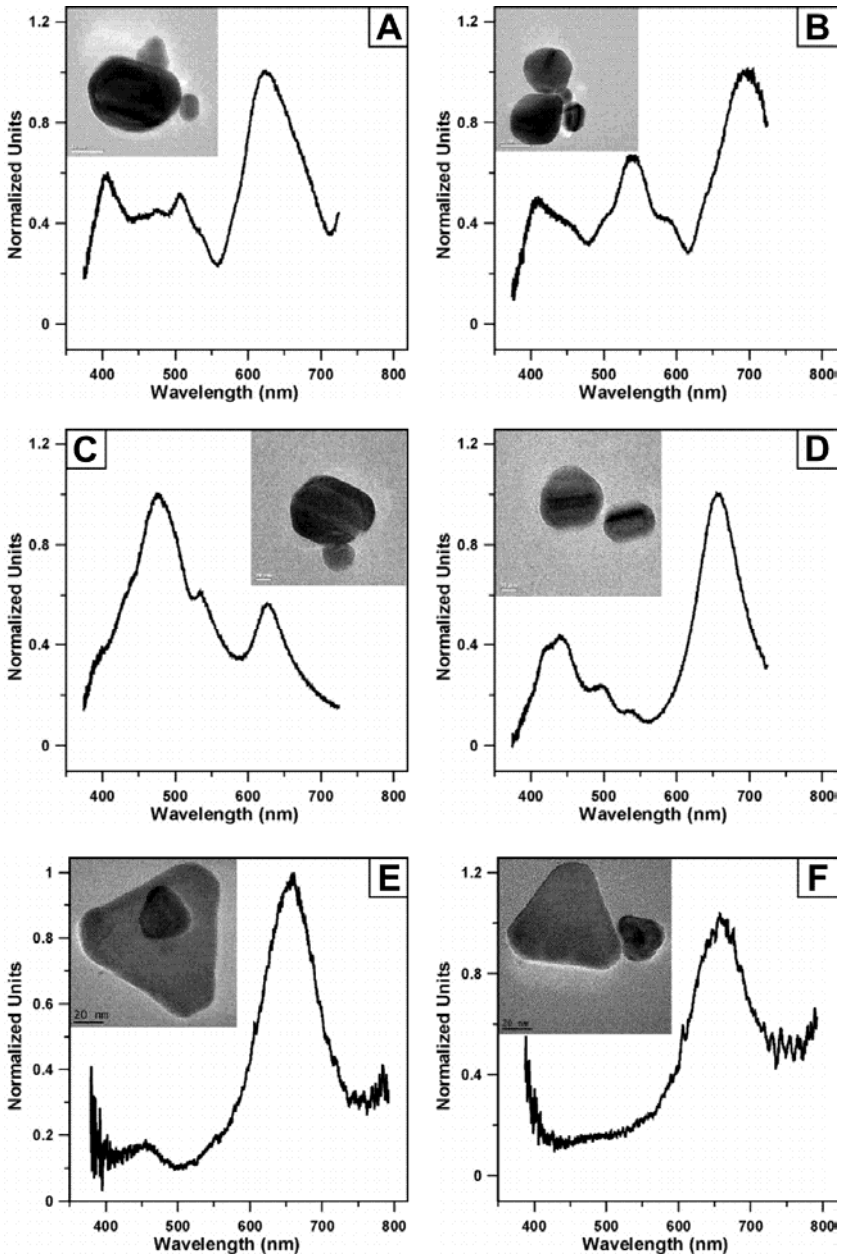

Figure 5.8 Correlated LSPR spectra and high resolution TEM images of silver nanoparticle aggregates.

shifted an unexpectedly large amount relative to the dipole mode. If a smaller nanoparticle was blocking one of the larger nanoprism's tips from chemical binding, a smaller than expected total shift may be observed.

5.4 Conclusions

The correlation of LSPR spectra with high resolution TEM images of the nanoparticle structures yielding those spectra will yield important insights into a number of phenomena in the field of nanoparticle optics. Here, we have definitively proven the spectral fingerprint of three nanoparticle geometries, and shown how the external geometry of a nanoparticle can affect the LSPR linewidth. Three conclusions can be drawn from this work: 1) Cylindrical geometries show the narrowest resonances of any geometry for excitations along their longitudinal axis. The narrow linewidths shown for these resonances have been hypothesized to be a consequence of coherent polarization, and have yielded the narrowest single nanoparticle LSPR linewidths to date. 2) The higher the radius of curvature of a nanoparticle's features the broader the LSPR linewidth. This was demonstrated using triangular nanoprisms. 3) The linewidth ratio between the two LSPR peaks for nanocubes suggests that CID processes may be an important factor in the energy dissipation dynamics of single nanoparticle systems in agreement with the work of Kreibig and coworkers.

Current studies are aimed at understanding the role of intrinsic nanoparticle structure in determining the LSPR linewidth. We are also performing high level electrodynamics calculations on structures that are defined by HRTEM, EELS, and dark-field TEM measurements in order to assess the performance of these methods in modeling the plasmonic properties of

single nanoparticles as they have been, to date, only used to model nanoparticle ensembles. Due to the complex nature of the spectra associated with nanoparticle aggregates, we are working to correlate HRTEM, LSPR spectra, and single molecule SERS spectra in order to gain further insights into the nature of the environments that yield the huge electromagnetic fields necessary for such sensitivity. Unfortunately, these nanoparticle aggregates were formed by randomly being deposited near or on top of each other while their suspensions were evaporating from the substrate surface. This makes systematic studies of these geometries unrealistic with our current approach.

II.2 Outlook

Part II of this thesis has described two approaches to correlating single nanoparticle optical and structural properties: *in-situ* TIR-AFM and correlating LSPR spectroscopy with HRTEM imaging. Each approach, while proving great utility, has demonstrated weaknesses. The finite size of the AFM probe in TIR-AFM limits the resolution of the system to ~10 nm, but allows the direct assembly of specific multi-nanoparticle geometries. On the other hand correlated LSPR-HRTEM imaging has an atomic scale probe (electron beam), but yields no control of the structures to be studied. Hence, the ultimate achievement in studying the optical properties of single and optically coupled nanoparticle systems will be realized by the combination of these two approaches. We believe this to be a realizable goal, and are currently investigating avenues towards this end.

References

1. Taniguchi, N., On the Basic Concept of 'Nano-Technology'. *Proceedings of the International Conference of Prod. Engineering Tokyo, Part II (Tokyo: Japan Society of Precision Engineering)* **1974**.

2. Faraday, M., The Bakerian Lecture: Experimental Relations of Gold (and Other Metals) to Light. *Philosophical Transactions of the Royal Society of London* **1857,** 147, 145-181.

3. Sajitha, E. P.; Prasad, V.; Subramanyam, S. V.; Mishra, A. K.; Sarkar, S.; Bansal, C., Size-dependent magnetic properties of iron carbide nanoparticles embedded in a carbon matrix. *Journal of Physics: Condensed Matter* **2007,** 19, (4), 046214/1-046214/13.

4. Park, T.-J.; Papaefthymiou, G. C.; Viescas, A. J.; Moodenbaugh, A. R.; Wong, S. S., Size-Dependent Magnetic Properties of Single-Crystalline Multiferroic BiFeO3 Nanoparticles. *Nano Letters* **2007,** 7, (3), 766-772.

5. He, L.; Zheng, W.; Zhou, W.; Du, H.; Chen, C.; Guo, L., Size-dependent magnetic properties of nickel nanochains. *Journal of Physics: Condensed Matter* **2007,** 19, (3), 036216/1-036216/10.

6. Sharma, S. K.; Kumar, R.; Kumar, V. V. S.; Dolia, S. N.; Gupta, A.; Reddy, V. R.; Knobel, M.; Singh, M., Size dependent magnetic behaviour of nanocrystalline spinel ferrite Mg0.95Mn0.05Fe2O4. *Indian Journal of Pure and Applied Physics* **2007,** 45, (1), 16-20.

7. Chen, J. P.; Sorensen, C. M.; Klabunde, K. J.; Hadjipanayis, G. C.; Devlin, E.; Kostikas, A., Size-dependent magnetic properties of MnFe2O4 fine particles synthesized by coprecipitation. *Physical Review B: Condensed Matter* **1996,** 54, (13), 9288-9296.

8. Tang, Z. X.; Sorensen, C. M.; Klabunde, K. J.; Hadjipanayis, G. C., Size-dependent magnetic properties of manganese ferrite fine particles. *Journal of Applied Physics* **1991,** 69, (8, Pt. 2A), 5279-81.

9. Heiz, U.; Schneider, W.-D., Nanoassembled model catalysts. *Journal of Physics D: Applied Physics* **2000,** 33, (11), R85-R102.

10. Hamilton, J. F.; Baetzold, R. C., Catalysis by small metal clusters. *Science (Washington, DC, United States)* **1979,** 205, (4412), 1213-20.

11. Jana, N. R.; Pal, T., Growing small metal particle as redox catalyst. *Current Science* **1998,** 75, (2), 145-149.

12. Santra, A. K.; Goodman, D. W., Size-dependent electronic, structural, and catalytic properties of metal clusters supported on ultrathin oxide films. *Catalysis and Electrocatalysis at Nanoparticle Surfaces* **2003**, 281-309.

13. Schumacher, E.; Blatter, F.; Frey, M.; Heiz, U.; Roethlisberger, U.; Schaer, M.; Vayloyan, A.; Yeretzian, C., Metal clusters: Between atom and bulk. *Chimia* **1988,** 42, (11), 357-76.

14. Xu, Z.; Xiao, F. S.; Purnell, S. K.; Alexeev, O.; Kawi, S.; Deutsch, S. E.; Gates, B. C., Size-dependent catalytic activity of supported metal clusters. *Nature (London)* **1994,** 372, (6504), 346-8.

15. Wilcoxon, J. P.; Abrams, B. L., Synthesis, structure and properties of metal nanoclusters. *Chemical Society Reviews* **2006,** 35, (11), 1162-1194.

16. Audoit, G.; Kulkarni, J. S.; Morris, M. A.; Holmes, J. D., Size dependent thermal properties of embedded crystalline germanium nanowires. *Journal of Materials Chemistry* **2007,** 17, (16), 1608-1613.

17. Liang, L. H.; Li, B., Size-dependent thermal conductivity of nanoscale semiconducting systems. *Physical Review B: Condensed Matter and Materials Physics* **2006,** 73, (15), 153303/1-153303/4.

18. Yang, H.-S.; Eastman, J. A.; Thompson, L. J.; Bai, G. R., Grain-size-dependent thermal transport properties in nanocrystalline yttria-stabilized zirconia. *Materials Research Society Symposium Proceedings* **2002,** 703, (Nanophase and Nanocomposite Materials IV), 179-184.

19. Hone, J.; Batlogg, B.; Benes, Z.; Llaguno, M. C.; Nemes, N. M.; Johnson, A. T.; Fischer, J. E., Thermal properties of single-walled carbon nanotubes. *Materials Research Society Symposium Proceedings* **2001,** 633, (Nanotubes and Related Materials), A17 1 1-A17 1 12.

20. Gaponik, N.; Shavel, A.; Talapin, D. V.; Poznyak, S. K.; Osipovich, N. P.; Gao, M., Size-dependent electrochemical behavior of thiol-capped nanocrystals. *Physics, Chemistry and Application of Nanostructures: Reviews and Short Notes to Nanomeeting 2005, [International Conference], Minsk, Belarus, May 24-27, 2005* **2005**, 341-344.

21. Chaki, N. K.; Sharma, J.; Mandle, A. B.; Mulla, I. S.; Pasricha, R.; Vijayamohanan, K., Size dependent redox behavior of monolayer protected silver nanoparticles (2-7 nm) in aqueous medium. *Physical Chemistry Chemical Physics* **2004,** 6, (6), 1304-1309.

22. Cheng, W.; Dong, S.; Wang, E., Gold Nanoparticles as Fine Tuners of Electrochemical Properties of the Electrode/Solution Interface. *Langmuir* **2002,** 18, (25), 9947-9952.

23. Pattabiraman, R., Electrochemical investigations on carbon supported palladium catalysts. *Applied Catalysis, A: General* **1997,** 153, (1-2), 9-20.

24. Lu, J.; Nagase, S.; Zhang, S.; Peng, L., Strongly size-dependent electronic properties in C60-encapsulated zigzag nanotubes and lower size limit of carbon nanopeapods. *Physical Review B: Condensed Matter and Materials Physics* **2003,** 68, (12), 121402/1-121402/4.

25. Liu, H., Theoretical and experimental study on the electronic structure of clusters. *Wuhan Gongye Daxue Xuebao* **1993,** 15, (4), 138-45.

26. Kumar, A.; Mital, S., Synthesis and photophysics of purine-capped Q-CdS nanocrystallites. *Photochem Photobiol Sci FIELD Full Journal Title:Photochemical & photobiological sciences : Official journal of the European Photochemistry Association and the European Society for Photobiology* **2002,** 1, (10), 737-41.

27. Odom, T. W.; Huang, J.-L.; Kim, P.; Lieber, C. M., Structure and Electronic Properties of Carbon Nanotubes. *Journal of Physical Chemistry B* **2000,** 104, (13), 2794-2809.

28. Dresselhaus, M. S.; Dresselhaus, G.; Pimenta, M., The remarkable properties of carbon nanotubes as nanoclusters. *European Physical Journal D: Atomic, Molecular and Optical Physics* **1999,** 9, (1-4), 69-75.

29. Issi, J. P.; Langer, L.; Heremans, J.; Olk, C. H., Electronic properties of carbon nanotubes: experimental results. *Carbon* **1995,** 33, (7), 941-8.

30. Kolwas, K., Size-dependent index of refraction and absorption of a spherical metal cluster. *Zeitschrift fuer Physik D: Atoms, Molecules and Clusters* **1996,** 38, (3), 233-240.

31. Kanemitsu, Y.; Suzuki, K.; Nakayoshi, Y.; Masumoto, Y., Quantum size effects and enhancement of the oscillator strength of excitons in chains of silicon atoms. *Physical Review B: Condensed Matter and Materials Physics* **1992,** 46, (7), 3916-19.

32. Jensen, T. R.; Malinsky, M. D.; Haynes, C. L.; van Duyne, R. P., Nanosphere Lithography: Tunable Localized Surface Plasmon Resonance Spectra of Silver Nanoparticles. *Journal of Physical Chemistry B* **2000,** 104, (45), 10549-10556.

33. Kelly, K. L.; Coronado, E.; Zhao, L. L.; Schatz, G. C., The Optical Properties of Metal Nanoparticles: The Influence of Size, Shape, and Dielectric Environment. *Journal of Physical Chemistry B* **2003,** 107, (3), 668-677.

34. Reather, H., *Surface Polaritons on Smooth and Rough Surfaces and on Gratings*. Springer-Verlag: Berlin, 1988.

35. Kreibig, U., Vollmer, M., *Optical Properties of Metal Clusters*. Springer-Verlag: Heidelberg, 1995; Vol. 25.

36. Jeanmaire, D. L.; Van Duyne, R. P., Surface Raman spectroelectrochemistry. Part I. Heterocyclic, aromatic, and aliphatic amines adsorbed on the anodized silver electrode. *Journal of Electroanalytical Chemistry and Interfacial Electrochemistry* **1977,** 84, (1), 1-20.

37. Schatz, G. C.; Young, M. A.; Van Duyne, R. P., Electromagnetic mechanism of SERS. *Topics in Applied Physics* **2006,** 103, (Surface-Enhanced Raman Scattering), 19-46.

38. Feynman, R. P. L., R. B.; Sands, M., *The Feynman Lectures on Physics*. Addison-Wesley: Reading, 1964; Vol. II.

39. Haynes, C. L.; Van Duyne, R. P., Nanosphere Lithography: A Versatile Nanofabrication Tool for Studies of Size-Dependent Nanoparticle Optics. *Journal of Physical Chemistry B* **2001,** 105, (24), 5599-5611.

40. Willets Katherine, A.; Van Duyne Richard, P., Localized surface plasmon resonance spectroscopy and sensing. *Annu Rev Phys Chem FIELD Full Journal Title:Annual review of physical chemistry* **2007,** 58, 267-97.

41. Martin, O. J. F., Surface plasmon illumination scheme for contact lithography beyond the diffraction limit. *Microelectronic Engineering* **2003,** 67-68, 24-30.

42. Haynes, C. L.; McFarland, A. D.; Zhao, L.; Van Duyne, R. P.; Schatz, G. C.; Gunnarsson, L.; Prikulis, J.; Kasemo, B.; Kaell, M., Nanoparticle Optics: The Importance of Radiative Dipole Coupling in Two-Dimensional Nanoparticle Arrays. *Journal of Physical Chemistry B* **2003,** 107, (30), 7337-7342.

43. Tong, H. D.; Jansen, H. V.; Gadgil, V. J.; Bostan, C. G.; Berenschot, E.; van Rijn, C. J. M.; Elwenspoek, M., Silicon nitride nanosieve membrane. *Nano Letters* **2004,** 4, (2), 283-287.

44. Dick, L. A.; McFarland, A. D.; Haynes, C. L.; Van Duyne, R. P., Metal Film over Nanosphere (MFON) Electrodes for Surface-Enhanced Raman Spectroscopy (SERS): Improvements in Surface Nanostructure Stability and Suppression of Irreversible Loss. *Journal of Physical Chemistry B* **2002,** 106, (4), 853-860.

45. Hulteen, J. C. V. D., R. P., Nanosphere Lithography: A Materials General Fabricaton Process for Periodic Particle Array Surfaces. *Journal of Vacuum Science and Technology A* **1995,** 13, 1553-1558.

46. Malinsky, M. D.; Kelly, K. L.; Schatz, G. C.; Van Duyne, R. P., Nanosphere Lithography: Effect of Substrate on the Localized Surface Plasmon Resonance Spectrum of Silver Nanoparticles. *Journal of Physical Chemistry B* **2001,** 105, (12), 2343-2350.

47. Haes, A. J.; Chang, L.; Klein, W. L.; Van Duyne, R. P., Detection of a Biomarker for Alzheimer's Disease from Synthetic and Clinical Samples Using a Nanoscale Optical Biosensor. *Journal of the American Chemical Society* **2005,** 127, (7), 2264-2271.

48. Whitney, A. V.; Myers, B. D.; Van Duyne, R. P., Sub-100 nm Triangular Nanopores Fabricated with the Reactive Ion Etching Variant of Nanosphere Lithography and Angle-Resolved Nanosphere Lithography. *Nano Letters* **2004,** 4, (8), 1507-1511.

49. Shafer-Peltier, K. E.; Haynes, C. L.; Glucksberg, M. R.; VanDuyne, R. P., Toward a glucose biosensor based on surface-enhanced raman scattering. *Journal of the American Chemical Society* **2003,** 125, (2), 588-593.

50. Zhang, X.; Hicks, E. M.; Zhao, J.; Schatz, G. C.; Van Duyne, R. P., Electrochemical Tuning of Silver Nanoparticles Fabricated by Nanosphere Lithography. *Nano Letters* **2005,** 5, (7), 1503-1507.

51. Lyandres, O.; Shah, N. C.; Yonzon, C. R.; Walsh, J. T., Jr.; Glucksberg, M. R.; Van Duyne, R. P., Real-Time Glucose Sensing by Surface-Enhanced Raman Spectroscopy in Bovine Plasma Facilitated by a Mixed Decanethiol/Mercaptohexanol Partition Layer. *Analytical Chemistry* **2005,** 77, (19), 6134-6139.

52. Zhang, X.; Young, M. A.; Lyandres, O.; Van Duyne, R. P., Rapid detection of an anthrax biomarker by surface-enhanced Raman spectroscopy. *Journal of the American Chemical Society* **2005,** 127, (12), 4484-4489.

53. Hulteen, J. C.; Treichel, D. A.; Smith, M. T.; Duval, M. L.; Jensen, T. R.; Van Duyne, R. P., Nanosphere Lithography: Size-Tunable Silver Nanoparticle and Surface Cluster Arrays. *Journal of Physical Chemistry B* **1999,** 103, (19), 3854-3863.

54. Haynes, C. L.; Van Duyne, R. P., Plasmon-Sampled Surface-Enhanced Raman Excitation Spectroscopy. *Journal of Physical Chemistry B* **2003,** 107, (30), 7426-7433.

55. McFarland, A. D.; Young, M. A.; Dieringer, J. A.; Van Duyne, R. P., Wavelength-Scanned Surface-Enhanced Raman Excitation Spectroscopy. *Journal of Physical Chemistry B* **2005,** 109, (22), 11279-11285.

56. Malinsky, M. D.; Kelly, K. L.; Schatz, G. C.; Van Duyne, R. P., Chain length dependence and sensing capabilities of the localized surface plasmon resonance of silver nanoparticles chemically modified with alkanethiol self-assembled monolayers. *Journal of the American Chemical Society* **2001,** 123, (7), 1471-1482.

57. Haes, A. J.; Van Duyne, R. P., A nanoscale optical biosensor: Sensitivity and selectivity of an approach based on the localized surface plasmon resonance spectroscopy of triangular silver nanoparticles. *Journal of the American Chemical Society* **2002,** 124, (35), 10596-10604.

58. McFarland, A. D.; Van Duyne, R. P., Single Silver Nanoparticles as Real-Time Optical Sensors with Zeptomole Sensitivity. *Nano Letters* **2003,** 3, (8), 1057-1062.

59. Jin, R.; Cao, Y.; Mirkin, C. A.; Kelly, K. L.; Schatz, G. C.; Zheng, J. G., Photoinduced conversion of silver nanospheres to nanoprisms. *Science* **2001,** 294, (5548), 1901-1903.

60. Murphy, C. J.; Sau, T. K.; Gole, A.; Orendorff, C. J., Surfactant-directed synthesis and optical properties of one-dimensional plasmonic metallic nanostructures. *MRS Bulletin* **2005,** 30, (5), 349-355.

61. Wiley, B.; Sun, Y.; Mayers, B.; Xia, Y., Shape-controlled synthesis of metal nanostructures: The case of silver. *Chemistry--A European Journal* **2005,** 11, (2), 454-463.

62. Wiley, B. J.; Xiong, Y.; Li, Z.-Y.; Yin, Y.; Xia, Y., Right Bipyramids of Silver: A New Shape Derived from Single Twinned Seeds. *Nano Letters* **2006,** 6, (4), 765-768.

63. Nehl, C. L.; Liao, H.; Hafner, J. H., Optical Properties of Star-Shaped Gold Nanoparticles. *Nano Letters* **2006,** 6, (4), 683-688.

64. Nehl, C. L.; Liao, H.; Hafner, J. H., Plasmon resonant molecular sensing with single gold nanostars. *Proceedings of SPIE-The International Society for Optical Engineering* **2006,** 6323, (Plasmonics: Metallic Nanostructures and Their Optical Properties IV), 63230G/1-63230G/8.

65. Smolyaninov, I. I.; Hung, Y.-J.; Davis, C. C., Surface plasmon dielectric waveguides. *Applied Physics Letters* **2005,** 87, (24), 241106/1-241106/3.

66. Maier, S. A.; Kik, P. G.; Atwater, H. A.; Meltzer, S.; Harel, E.; Koel, B. E.; Requicha, A. A. G., Local detection of electromagnetic energy transport below the diffraction limit in metal nanoparticle plasmon waveguides. *Nature Materials* **2003,** 2, (4), 229-232.

67. Krenn, J. R., Nanoparticle waveguides. Watching energy transfer. *Nature Materials* **2003,** 2, (4), 210-211.

68. Ozbay, E., Plasmonics: Merging photonics and electronics at nanoscale dimensions. *Science* **2006,** 311, (5758), 189-193.

69. Vasseur, J. O.; Akjouj, A.; Dobrzynski, L.; Djafari-Rouhani, B.; El Boudouti, E. H., Photon, electron, magnon, phonon and plasmon mono-mode circuits. *Surface Science Reports* **2004,** 54, (1-4), 1-156.

70. Reinhard, B. M.; Siu, M.; Agarwal, H.; Alivisatos, A. P.; Liphardt, J., Calibration of Dynamic Molecular Rulers Based on Plasmon Coupling between Gold Nanoparticles. *Nano Letters* **2005,** 5, (11), 2246-2252.

71. Elghanian, R.; Storhoff, J. J.; Mucic, R. C.; Letsinger, R. L.; Mirkin, C. A., Selective colorimetric detection of polynucleotides based on the distance-dependent optical properties of gold nanoparticles. *Science* **1997,** 277, (5329), 1078-1080.

72. Mock, J. J.; Smith, D. R.; Schultz, S., Local Refractive Index Dependence of Plasmon Resonance Spectra from Individual Nanoparticles. *Nano Letters* **2003,** 3, (4), 485-491.

73. Link, S.; Wang, Z. L.; El-Sayed, M. A., Alloy Formation of Gold-Silver Nanoparticles and the Dependence of the Plasmon Absorption on Their Composition. *J. Phys. Chem. B* **1999,** 103, (18), 3529-3533.

74. Jin, R.; Cao, Y. C.; Hao, E.; Metraux, G. S.; Schatz, G. C.; Mirkin, C. A., Controlling Anisotropic Nanoparticle Growth Through Plasmon Excitation. *Nature* **2003,** 425, (6957), 487-490.

75. Sherry, L. J.; Chang, S.-H.; Schatz, G. C.; Van Duyne, R. P.; Wiley, B. J.; Xia, Y., Localized Surface Plasmon Resonance Spectroscopy of Single Silver Nanocubes. *Nano Letters* **2005,** 5, (10), 2034-2038.

76. Xu, G.; Chen, Y.; Tazawa, M.; Jin, P., Surface Plasmon Resonance of Silver Nanoparticles on Vanadium Dioxide. *Journal of Physical Chemistry B* **2006,** 110, (5), 2051-2056.

77. Pinchuk, A.; Hilger, A.; von Plessen, G.; Kreibig, U., Substrate effect on the optical response of silver nanoparticles. *Nanotechnology* **2004,** 15, (12), 1890-1896.

78. Huang, W.; Qian, W.; El-Sayed, M. A., The Optically Detected Coherent Lattice Oscillations in Silver and Gold Monolayer Periodic Nanoprism Arrays: The Effect of Interparticle Coupling. *Journal of Physical Chemistry B* **2005,** 109, (40), 18881-18888.

79. Zhao, L.; Kelly, K. L.; Schatz, G. C., The Extinction Spectra of Silver Nanoparticle Arrays: Influence of Array Structure on Plasmon Resonance Wavelength and Width. *Journal of Physical Chemistry B* **2003,** 107, (30), 7343-7350.

80. Gunnarsson, L.; Rindzevicius, T.; Prikulis, J.; Kasemo, B.; Kaell, M.; Zou, S.; Schatz, G. C., Confined Plasmons in Nanofabricated Single Silver Particle Pairs: Experimental Observations of Strong Interparticle Interactions. *Journal of Physical Chemistry B* **2005,** 109, (3), 1079-1087.

81. Mie, G., Contributions to the Optics of Turbid Media, Especially Colloidal Metal Solutions. *Annalen der Physik (Weinheim, Germany)* **1908,** 25, 377-445.

82. Hicks, E. M.; Zou, S.; Schatz, G. C.; Spears, K. G.; Van Duyne, R. P.; Gunnarsson, L.; Rindzevicius, T.; Kasemo, B.; Kaell, M., Controlling Plasmon Line Shapes through Diffractive Coupling in Linear Arrays of Cylindrical Nanoparticles Fabricated by Electron Beam Lithography. *Nano Letters* **2005,** 5, (6), 1065-1070.

83. Henzie, J.; Kwak, E.-S.; Odom, T. W., Mesoscale Metallic Pyramids with Nanoscale Tips. *Nano Letters* **2005,** 5, (7), 1199-1202.

84. Murphy, C. J.; Sau, T. K.; Gole, A. M.; Orendorff, C. J.; Gao, J.; Gou, L.; Hunyadi, S. E.; Li, T., Anisotropic metal nanoparticles: synthesis, assembly, and optical applications. *Journal of Physical Chemistry B* **2005,** 109, (29), 13857-13870.

85. Wiley, B. J.; Im, S. H.; Li, Z.-Y.; McLellan, J.; Siekkinen, A.; Xia, Y., Maneuvering the Surface Plasmon Resonance of Silver Nanostructures through Shape-Controlled Synthesis. *Journal of Physical Chemistry B* **2006,** 110, (32), 15666-15675.

86. Sau, T. K.; Murphy, C. J., Seeded high yield synthesis of short Au nanorods in aqueous solution. *Langmuir* **2004,** 20, (15), 6414-6420.

87. Payne, E. K.; Shuford, K. L.; Park, S.; Schatz, G. C.; Mirkin, C. A., Multipole Plasmon Resonances in Gold Nanorods. *Journal of Physical. Chemistry B* **2006,** 110, (5), 2150-2154.

88. Moreno, E.; Erni, D.; Hafner, C.; Vahldieck, R., Multiple multipole method with automatic multipole setting applied to the simulation of surface plasmons in metallic nanostructures. *Journal of the Optical Society of America. A* **2002,** 19, (1), 101-11.

89. Yang, W.-H.; Schatz, G. C.; Van Duyne, R. P., Discrete dipole approximation for calculating extinction and Raman intensities for small particles with arbitrary shapes. *Journal of Chemical Physics* **1995,** 103, (3), 869-75.

90. Mackowski, D. W., Calculation of Total Cross Sections of Multiple-Sphere Clusters. *Journal of the Optical Society of America. A* **1994,** 11, (11), 2851-2861.

91. Grayson, A. C. R.; Choi, I. S.; Tyler, B. M.; Wang, P. P.; Brem, H.; Cima, M. J.; Langer, R., Multi-pulse drug delivery from a resorbable polymeric microchip device. *Nature Materials* **2003,** 2, (11), 767-772.

92. Kwak, E.-S.; Henzie, J.; Chang, S.-H.; Gray, S. K.; Schatz, G. C.; Odom, T. W., Surface Plasmon Standing Waves in Large-Area Subwavelength Hole Arrays. *Nano Letters* **2005,** 5, (10), 1963-1967.

93. Taflove, A., Hagness, S. C., *Computational Electrodynamics: The Finite-Difference Time-Domain Method*. Artech House: Boston, 2000.

94. Draine, B. F., J., Discrete-Dipole Approximation for Scattering Calculations. *Journal of the Optical Society of America. A* **1994,** 11, 1491-1499.

95. Draine, B. F., J., *User Guide to the Discrete Dipole Approximation Code DDSCAT.6.0.* *http://arxiv.org/abs-ph/0300969* **2003**.

96. Tsukerman, I.; Cajko, F.; Sokolov, A. P., Traditional and new simulation techniques for nanoscale optics and photonics. *Proceedings of SPIE-The International Society for Optical Engineering* **2005,** 5927, (Plasmonics: Metallic Nanostructures and Their Optical Properties III), 59270L/1-59270L/10.

97. Yonzon, C. R.; Stuart, D. A.; Zhang, X.; McFarland, A. D.; Haynes, C. L.; Van Duyne, R. P., Towards advanced chemical and biological nanosensors - An overview. *Talanta* **2005,** 67, (3), 438-448.

98. Shaikh, K. A.; Ryu, K. S.; Goluch, E. D.; Nam, J.-M.; Liu, J.; Thaxton, C. S.; Chiesl, T. N.; Barron, A. E.; Lu, Y.; Mirkin, C. A.; Liu, C., A modular microfluidic architecture for integrated biochemical analysis. *Proceedings of the National Academy of Sciences of the United States of America* **2005,** 102, (28), 9745-9750.

99. Haynes, C. L.; Yonzon, C. R.; Zhang, X.; Van Duyne, R. P., Surface-enhanced Raman sensors: Early history and the development of sensors for quantitative biowarfare agent and glucose detection. *Journal of Raman Spectroscopy* **2005,** 36, (6/7), 471-484.

100. Cao, Y. C.; Jin, R.; Mirkin, C. A., Nanoparticles with Raman spectroscopic fingerprints for DNA and RNA detection. *Science* **2002,** 297, (5586), 1536-1540.

101. Nath, N.; Chilkoti, A., A colorimetric gold nanoparticle sensor to interrogate biomolecular interactions in real time on a surface. *Analytical Chemistry* **2002,** 74, (3), 504-509.

102. Okamoto, T.; Yamaguchi, I.; Kobayashi, T., Local plasmon sensor with gold colloid monolayers deposited upon glass substrates. *Optics Letters* **2000,** 25, (6), 372-374.

103. Hilger, A.; Cuppers, N.; Tenfelde, M.; Kreibig, U., Surface and interface effects in the optical properties of silver nanoparticles. *European Physical Journal D: Atomic, Molecular and Optical Physics* **2000,** 10, (1), 115-118.

104. Henglein, A.; Meisel, D., Spectrophotometric Observations of the Adsorption of Organosulfur Compounds on Colloidal Silver Nanoparticles. *Journal of Physical Chemistry B* **1998,** 102, (43), 8364-8366.

105. Taton, T. A.; Lu, G.; Mirkin, C. A., Two-Color Labeling of Oligonucleotide Arrays via Size-Selective Scattering of Nanoparticle Probes. *Journal of the American Chemical Society* **2001,** 123, (21), 5164-5165.

106. Schultz, S.; Smith, D. R.; Mock, J. J.; Schultz, D. A., Single-target molecule detection with nonbleaching multicolor optical immunolabels. *Proceedings of the National Academy of Sciences of the United States of America* **2000,** 97, (3), 996-1001.

107. Sonnichsen, C.; Franzl, T.; Wilk, T.; von Plessen, G.; Feldmann, J.; Wilson, O.; Mulvaney, P., Drastic Reduction of Plasmon Damping in Gold Nanorods. *Physical Review Letters* **2002,** 88, (7), 077402/1-077402/4.

108. Connolly, S.; Cobbe, S.; Fitzmaurice, D., Effects of ligand-receptor geometry and stoichiometry on protein-induced aggregation of biotin-modified colloidal gold. *Journal of Physical Chemistry B* **2001,** 105, (11), 2222-2226.

109. Mirkin, C. A.; Letsinger, R. L.; Mucic, R. C.; Storhoff, J. J., A DNA-based method for rationally assembling nanoparticles into macroscopic materials. *Nature (London)* **1996,** 382, (6592), 607-609.

110. Storhoff, J. J.; Elghanian, R.; Mucic, R. C.; Mirkin, C. A.; Letsinger, R. L., One-Pot Colorimetric Differentiation of Polynucleotides with Single Base Imperfections Using Gold Nanoparticle Probes. *Journal of the American Chemical Society* **1998,** 120, (9), 1959-1964.

111. Miller, M. M.; Lazarides, A. A., Sensitivity of Metal Nanoparticle Surface Plasmon Resonance to the Dielectric Environment. *Journal of Physical Chemistry B* **2005,** 109, (46), 21556-21565.

112. Maillard, M.; Huang, P.; Brus, L., Silver Nanodisk Growth by Surface Plasmon Enhanced Photoreduction of Adsorbed [Ag+]. *Nano Letters* **2003,** 3, (11), 1611-1615.

113. Haes, A. J.; Zou, S.; Schatz, G. C.; Van Duyne, R. P., A Nanoscale Optical Biosensor: The Long Range Distance Dependence of the Localized Surface Plasmon Resonance of Noble Metal Nanoparticles. *Journal of Physical Chemistry B* **2004,** 108, (1), 109-116.

114. Yonzon Chanda, R.; Jeoung, E.; Zou, S.; Schatz George, C.; Mrksich, M.; Van Duyne Richard, P., A comparative Analysis of Localized and Propagating Surface Plasmon Resonance Sensors: The Binding of Concanavalin A to a Monosaccharide Functionalized Self-Sssembled Monolayer. *Journal of the American Chemical Society* **2004,** 126, (39), 12669-76.

115. Haes, A. J.; Zou, S.; Schatz, G. C.; Van Duyne, R. P., Nanoscale Optical Biosensor: Short Range Distance Dependence of the Localized Surface Plasmon Resonance of Noble Metal Nanoparticles. *Journal of Physical Chemistry B* **2004,** 108, (22), 6961-6968.

116. Link, S. E.-S., M.A., Spectral Properties and Relaxation Dynamics of Surface Plasmon Electronic Oscillations in gold And Silver Nanodots and Nanorods. *Journal of Physical Chemistry B* **1999,** 103, (40), 8410-8426.

117. Whitney, A. V.; Elam, J. W.; Zou, S.; Zinovev, A. V.; Stair, P. C.; Schatz, G. C.; Van Duyne, R. P., Localized Surface Plasmon Resonance Nanosensor: A High-Resolution Distance-Dependence Study Using Atomic Layer Deposition. *Journal of Physical Chemistry B* **2005,** 109, (43), 20522-20528.

118. Haes, A. J.; Van Duyne, R. P., Probing the long range distance dependence of noble metal nanoparticles. *Materials Research Society Symposium Proceedings* **2004,** 789, (Quantum Dots, Nanoparticles and Nanowires), 409-414.

119. Chang, S.-H., Gray, S. K., Schatz, G. C., Surface Plasmon Generation and Light Transmission by Isolated Nanoholes and Arrays of Nanoholes in Thin Metal Films. *Optics Express* **2005,** 13, 3150-3165.

120. Gray, S. K.; Kupka, T., Propagation of light in metallic nanowire arrays: finite-difference time-domain studies of silver cylinders. *Physical Review B: Condensed Matter and Materials Physics* **2003,** 68, (4), 045415/1-045415/11.

121. Sonnichsen, C.; Geier, S.; Hecker, N. E.; von Plessen, G.; Feldmann, J.; Ditlbacher, H.; Lamprecht, B.; Krenn, J. R.; Aussenegg, F. R.; Chan, V. Z. H.; Spatz, J. P.; Moller, M., Spectroscopy of single metallic nanoparticles using total internal reflection microscopy. *Applied Physics Letters* **2000,** 77, (19), 2949-2951.

122. Klar, T.; Perner, M.; Grosse, S.; von Plessen, G.; Spirkl, W.; Feldmann, J., Surface-Plasmon Resonances in Single Metallic Nanoparticles. *Physical Review Letters* **1998,** 80, (19), 4249-4252.

123. Hao, E.; Schatz, G. C., Electromagnetic fields around silver nanoparticles and dimers. *Journal of Chemical Physics* **2004,** 120, (1), 357-366.

124. Metraux, G. S.; Mirkin, C. A., Rapid thermal synthesis of silver nanoprisms with chemically tailorable thickness. *Advanced Materials (Weinheim, Germany)* **2005,** 17, (4), 412-415.

125. Liu, F.-K.; Ko, F.-H.; Huang, P.-W.; Wu, C.-H.; Chu, T.-C., Studying the size/shape separation and optical properties of silver nanoparticles by capillary electrophoresis. *Journal of Chromatography A* **2005,** 1062, (1), 139-45.

126. Piner, R. D.; Zhu, J.; Xu, F.; Hong, S.; Mirkin, C. A., "Dip-pen" nanolithography. *Science (Washington, D. C.)* **1999,** 283, (5402), 661-663.

127. Zou, S.; Schoenherr, H.; Vancso, G. J., Force Spectroscopy of Quadruple H-Bonded Dimers by AFM: Dynamic Bond Rupture and Molecular Time-Temperature Superposition. *Journal of the American Chemical Society* **2005,** 127, (32), 11230-11231.

128. Okajima, T.; Arakawa, H.; Taufiq Alam, M.; Sekiguchi, H.; Ikai, A., Dynamics of a partially stretched protein molecule studied using an atomic force microscope. *Biophysical Chemistry* **2004,** 107, (1), 51-61.

129. Stockle, R. M.; Suh, Y. D.; Deckert, V.; Zenobi, R., Nanoscale chemical analysis by tip-enhanced Raman spectroscopy. *Chemical Physics Letters* **2000,** 318, (1,2,3), 131-136.

130. Anderson, M. S., Locally enhanced Raman spectroscopy with an atomic force microscope. *Applied Physics Letters* **2000,** 76, (21), 3130-3132.

131. Brakenhoff, G. J.; van Spronsen, E. A.; van der Voort, H. T.; Nanninga, N., Three-dimensional confocal fluorescence microscopy. *Journal Title:Methods in cell biology* **1989,** 30, 379-98.

132. Berger, C. E. H.; Kooyman, R. P. H.; Greve, J., Resolution in surface plasmon microscopy. *Review of Scientific Instruments* **1994,** 65, (9), 2829-36.

133. Sherry, L. J.; Jin, R.; Mirkin, C. A.; Schatz, G. C.; Van Duyne, R. P., Localized Surface Plasmon Resonance Spectroscopy of Single Silver Triangular Nanoprisms. *Nano Letters* **2006,** 6, (9), 2060-2065.

134. Lee, P. C.; Meisel, D., Adsorption and surface-enhanced Raman of dyes on silver and gold sols. *Journal of Physical Chemistry* **1982,** 86, (17), 3391-3395.

135. Mock, J. J.; Barbic, M.; Smith, D. R.; Schultz, D. A.; Schultz, S., Shape effects in plasmon resonance of individual colloidal silver nanoparticles. *Journal of Chemical Physics* **2002,** 116, (15), 6755-6759.

136. Mehtani, D.; Lee, N.; Hartschuh, R. D.; Kisliuk, A.; Foster, M. D.; Sokolov, A. P.; Cajko, F.; Tsukerman, I., Optical Properties and Enhancement Factors of the Tips for Apertureless Near-field Optics. *Journal of Optics A* **2006,** 8, S183-S190.

137. Zhao, L.; Jensen, L.; Schatz, G. C., Pyridine-Ag20 Cluster: A Model System for Studying Surface-Enhanced Raman Scattering. *Journal of the American Chemical Society* **2006,** 128, (9), 2911-2919.

138. Hao, E.; Schatz, G. C., Electromagnetic Fields Around Silver Nanoparticles and Dimers. *Journal of Chemical Physics* **2004,** 120, 357-366.

139. Alvarez, M. M.; Khoury, J. T.; Schaaff, T. G.; Shafigullin, M. N.; Vezmar, I.; Whetten, R. L., Optical Absorption Spectra of Nanocrystal Gold Molecules. *Journal of Physical Chemistry B* **1997,** 101, (19), 3706-3712.

140. Link, S.; El-Sayed, M. A., Size and Temperature Dependence of the Plasmon Absorption of Colloidal Gold Nanoparticles. *Journal of Physical Chemistry B* **1999,** 103, (21), 4212-4217.

141. Kreibig, U., The transition cluster-solid state in small gold particles. *Solid State Communications* **1978,** 28, (9), 767-9.

142. Doremus, R. H., Optical properties of small silver particles. *Journal of Chemical Physics* **1965,** 42, (1), 414-417.

143. Ziman, J. M., *Theory of Solids*. University Prss: Cambridge, 1979; p 278.

144. Kawabata, A.; Kubo, R., Electronic properties of fine metallic particles. II. Plasma resonance absorption. *Journal of the Physical Society of Japan* **1966,** 21, (9), 1765-72.

145. Persson, N. J., Polarizability of Small Spherical Metal Particles: Influence of the Matrix Environmnet. *Surface Science* **1993,** 281, 153-162.

146. Kraus, W. A.; Schatz, G. C., Plasmon resonance broadening in small metal particles. *Journal of Chemical Physics* **1983,** 79, (12), 6130-9.

147. Kraus, W. A.; Schatz, G. C., Plasmon resonance broadening in spheroidal metal particles. *Chemical Physics Letters* **1983,** 99, (4), 353-7.

148. Scherer, N. F.; Pelton, M.; Jin, R.; Jureller, J. E.; Liu, M.; Kim, H. Y.; Park, S.; Guyot-Sionnest, P., Optical nonlinearities of metal nanoparticles: single-particle measurements and correlation to structure. *Proceedings of SPIE-The International Society for Optical Engineering* **2006,** 6323, (Plasmonics: Metallic Nanostructures and Their Optical Properties IV), 632309/1-632309/6.

149. Pines, D.; Bohm, D., A collective description of electron interactions. II. Collective vs. individual particle aspects of the interactions. *Physical Review* **1952,** 85, 338-353.

150. Hovel, H.; Fritz, S.; Hilger, A.; Kreibig, U.; Vollmer, M., Width of Cluster Plasmon Resonances: Bulk Dieletric Functions and Chemical Interface Damping. *Physical Review B: Condensed Matter* **1993,** 48, (24), 18178-18188.

Leif J. Sherry

Northwestern University
2145 Sheridan Road
Evanston, Illinois 60208-3113
E-mail: l-sherry@northwestern.edu
Phone: (773) 983-2424

Education

June, 2007 **PhD**, Chemistry, Northwestern University, Evanston, IL

2002 **BS**, Chemistry, Centenary College of Louisiana, Shreveport, LA (minors: Mathematics, Physics)

Experience

2003-present **Northwestern University, Department of Chemistry**, Evanston, IL
Research Assistant
- Studied plasmonic properties of single metal nanostructures.

2002-2003 **Northwestern University, Department of Chemistry,** Evanston, IL
Teaching Assistant
- Developed and delivered lectures for General Chemistry and Advanced Photochemistry labs.
- Assessed laboratory performance and graded written reports.

2001-2002 **Centenary College, Department of Chemistry**, Shreveport, LA
Teaching Assistant
- Supervised General Chemistry labs and prepared reagents for analysis.

2001 **NASA-Glenn Research Center**, Cleveland, OH.
Summer Faculty Fellow
- Conducted research on laser-assisted growth mechanisms of carbon nanotubes, and flame annealing of soot.
- Work contributed to a publication in *Nano Letters*, **2003**; 3, 223-229.

Computer Skills

Proficient with Word, Excel, PowerPoint, MatLab, MathCAD, and UNIX
Experience with LabVIEW and Fortran

Field

Physical/Materials/Theoretical Chemistry

Research Areas

- Morphology dependence of single nanoparticle optical properties
- Optimizing single nanoparticle chemical/biological sensors
- Theoretical analysis of optical modes of single and coupled nanoparticle structures

Awards and Recognitions

2006 **Outstanding Researcher Award** from Northwestern University's Nanoscale Science and Engineering Center.

2005 **Fellow** of Northwestern University's Preparing Future Faculty Program.

2002 **University Graduation Honors (Cum Laude)** from Centenary College of Louisiana.

2002 **Departmental Graduation Honors** from Centenary College of Louisiana, Chemistry Department. Thesis: "*Laser Assisted Methods of Carbon Nanotube Synthesis"*.

2001 **First Prize** at the Centenary College Undergraduate Research Symposium: Topic – "*Laser Assisted Methods of Carbon Nanotube Synthesis*" (fifty participants).

2001 **Summer Faculty Fellowship** from the Center for Microgravity Research: Fluids and Combustion, NASA-Glenn Research Center, Cleveland, OH.

1999 **Fellow** of Belmont University's Honor's Program.

Peer Reviewed Publications

- "Synthesis, Structure, and Physical Properties of Some $CsLnCoQ_3$ Compounds: Low-Dimensional Magnetism in $CsYbZnSe_3$," Chan, G. H.; **Sherry, L. J.**; Van Duyne, R. P.; Ibers, J. A. *Inorg. Chem. Accepted*.

- "Nanoscale Localized Surface Plasmon Resonance Biosensors," Willets, K. A.; Hall, W. P.; **Sherry, L. J.**; Zhang, X.; Zhao, J.; Van Duyne, R. P. appearing in Nanobiotechnology II. Eds. C.A. Mirkin and C.M. Niemeyer. Weinheim: Wiley-VCH, 2006.

- "Localized Surface Plasmon Resonance Spectroscopy of Single Silver Nanoprisms," **Sherry, L. J.**; Jin, R.; Mirkin, C. A.; Schatz, G. C.; Van Duyne, R. P. *Nano Lett.,* 6, 2060-2065 (2006).

- "Localized Surface Plasmon Resonance Spectroscopy of Single Silver Nanocubes," **Sherry, L. J.**; Chang, S.-H.; Schatz, G. C.; Van Duyne, R. P.; Wiley, B. J.; Xia, Y. *Nano Lett.*, 5, 2034-2038 (2005).

- "Synthesis, Structure, Some Band Gaps, and Electronic Structures of $CsLnZnTe_3$ (Ln = La, Pr, Nd, Sm, Gd, Tb, Dy, Ho, Er, Tm, Y)," Yao, J., Deng, B., **Sherry, L. J.**, McFarland, A. D., Ellis, D. E., Van Duyne, R. P., Ibers, J. A. *Inorg. Chem.*, 43, 7735-7740 (2004).

Invention Disclosures

- NU 26111 (July 31, 2006): "Localized Surface Plasmon Resonance Spectroscopy of Single Silver Triangular Nanoprisms", Inventors: L. Sherry, R. Jin, C. A. Mirkin, G. C. Schatz, and R. P. Van Duyne

Invention Disclosures (Continued)

- NU 25080 (August 26, 2005): "Localized Surface Plasmon Resonance Spectroscopy of Single Silver Nanocubes", Inventors: L. Sherry, S.-H. Chang, G. C. Schatz, R. P. Van Duyne

Presentations

2006	Northwestern University Nanoscale Science and Engineering Center Annual Review Poster Session
2005	Guest Lecturer for Northeastern Illinois University's Chemistry Department
2004	American Chemical Society National Conference Poster Session
2002	American Chemical Society National Conference Poster Session
2002	Centenary College Undergraduate Research Symposium
2001	NASA-Glenn's Microgravity Research Center Quarterly Meeting

Synergistic Activities

2006	Author of the research proposal "Spatial, Temporal, and Structural Correlation in Single Nanoparticle Localized Surface Plasmon Resonance Spectroscopy", NU Nanoscale Science and Engineering Center, $31,000.
2005	Co-organized Northwestern University Chemistry Department's 3rd annual "All Scout Nano Event", which brings in area scouts and exposes them, through activities and hands on demos, to nanotechnology and its possibilities.
2004-present	Participant in Northwestern University Chemistry Department's "Science in the Classroom" initiative, which designs and implements interactive science modules for area elementary students.
2003-present	Member of Northwestern University's Nanoalliance; a student driven organization composed of graduate students from the Kellogg, McCormick, and Weinberg Schools who all share interests in nanotechnology.

- Research highlighted in the inaugural edition of "citatioN", see: http://nunanoalliance.org/citatioN/citatioNFall2005.pdf

Professional Affiliations

- Phi Lambda Upsilon, Graduate Chemistry Honor Society
- American Chemical Society